APPENDIX

UNIVERSITY OF HAWAII

INSTITUTE FOR ASTRONOMY

2680 Woodlawn Drive

Honolulu, Hawaii 96822

NASA GRANT NGL 12-001-57

SEMIANNUAL PROGRESS REPORTS #32 and #33

Dale P. Cruikshank, Principal Investigator

For the Period

January-December 1986

TABLE OF CONTENTS

I. PERSONNEL

This report covers the period January–December 1986. Scientific personnel engaged in planetary research who were supported fully or in part by this grant during the report period area as follows:

D. P. Cruikshank	D. Morrison	C. B. Pilcher
W. M. Sinton	M. W. Buie	D. J. Tholen

In addition, graduate students A. D. Storrs, H. B. Hammel, J. R. Piscitelli, and I. Heyer received salary and/or travel support on research assistantships. K. Uchida and Dr. N. Lark also received salary and travel support while working on special research projects during the year.

II. THE RESEARCH PROGRAMS

A. HIGHLIGHTS

1. Determination of the physical and orbital parameters of Pluto and Charon, including their diameters and the mean density of the system.

2. Acquisition of the best images of Neptune ever taken, showing cloud patterns and limb brightening in the light of methane, 8900 Å.

3. Determination of the rotation period of Neptune from high-resolution imagery, giving a result consistent with other determinations by photometry and imagery.

4. Acquisition of high-resolution images of Uranus with photometric calibration for studies of the planet's atmosphere.

5. Continued study of the thermal properties of the Galilean satellite Io from infrared observations during eclipses and occultations, and by polarimetry.

6. Discovery of major changes in the spectrum of Triton from observations with the cooled-grating array spectrometer in the near-infrared.

7. Study of the infrared spectrum of Io and a determination of the isotopic content of the sulfur dioxide snow on the satellite's surface.

8. Detection of a nonwater-ice volatile on Europa and its apparent time variability.

9. Observations of stellar occultations by the rings of Uranus with model fitting.

10. Observations of the rotational lightcurves of numerous peculiar asteroids, including Trojans, Hildas, and other peculiar objects.

11. Continued study of infrared spectra of asteroids in an effort to trace the origins of the S types and the A types.

12. Discovery of the C-H organic signature in the infrared spectrum of the wet C-type asteroid 130 Elektra.

13. Photometry of 11 planet-crossing asteroids.

14. Acquisition of an enormous body of photometric, spectroscopic, photographic, and electronic (CCD) imagery of Comet Halley, the analysis of which is in progress.

15. Laboratory study of a suite of dark materials, mostly organic in nature, in connection with our study of the dark material on solar system bodies (comets, planetary satellites, asteroids).

16. Breakthrough in the modeling of thermal inertias and thermal conductivities of solar system bodies.

17. Study of very high-resolution spectra of several K and M giant stars in the search for velocity shifts indicative of planet-size bodies in orbit around these stars.

18. Use of 32% of 2.2-m telescope time for solar system studies of interest to NASA during the calendar year 1986.

B. MAJOR PLANETS

B1. Outer Planet Imaging-Neptune and Uranus

Over 500 images of Neptune and nearly 150 images of Uranus were obtained by H. Hammel in three observing runs in 1986 using three different methane-band filters and three continuum filters (Figs. 1-3). Most of the images are good quality; some of the images of Neptune are of exceptional quality and may represent the finest images of this planet to date.

Discrete cloud features were observed on Neptune in many images. One particularly bright feature was observed crossing the planetary disk on at least two nights (Fig. 2) and was used to determine an atmospheric rotation period (Hammel and Buie, 1987). The measurements from a single night are not sufficient to calculate a rotation period accurately because of possible confusion from fainter spots, ambiguity in the pole position of Neptune, and other problems. Fortunately, the problems are minimal when a feature transits (crosses the central meridian of the planet as seen from Earth). By combining the observations from a night, the transit time can be calculated very accurately (Fig. 4). From the difference in transit times separated by many days, an atmospheric rotation period of 17.86 (± 0.02) hours was obtained for latitude -38° (± 2°). This period is consistent with earlier observations of cloud motion on Neptune. Hammel is working on determining the rotation period of some of the fainter features at different latitudes in hopes of deriving the vertical shear. The imaging method supersedes previous photometric work because the precise latitudes of atmospheric activity can be isolated.

The distribution of bright clouds on Neptune appears to have changed significantly since 1983. All images obtained prior to 1984 showed bright features of comparable magnitude in both the northern and southern mid-latitude regions, giving the planet the appearance of having a dark equatorial belt. But in 1986, no bright features were detected in the northern hemisphere

(Fig. 1). The imaging covers the full rotation cycle of Neptune over many weeks. Activity in the southern hemisphere is confined to latitudes -30° through -60°, consistent with that seen earlier. But activity in the northern hemisphere must have been subdued, at least during the months of May and June. The time scale of change of features in the southern hemisphere seems to be on the order of weeks to months. At least one fainter feature was seen to brighten over a period of three weeks to the same level as the bright feature discussed above.

Center-to-limb brightness variations are visible on both planets. Methane-band images show limb-brightening; continuum images show either limb-darkening or a uniform light distribution. The excellent quality of the images of Neptune allows different center-to-limb profiles to be extracted for various regions on the planet. A mean profile was obtained for the dark region by summing a series of radial profiles at different position angles across the northern hemisphere. By measuring the brightness of the brightest feature at a variety of positions on the disk, a center-to-limb profile was created for a bright region. Hammel is working with colleague K. Baines at JPL to generate atmospheric vertical structure models that fit these two differing regions.

On Uranus, the peak of the brightness distribution in the continuum wavelengths is offset from the center of the planetary disk, consistent with Voyager observations indicating a polar haze. The methane-band images show very obvious limb-brightening (Figs. 3 and 5). The very good signal-to-noise in these Uranus images will allow refinement of atmospheric vertical structure models by comparison with the observed radial brightness variations. Data reduction is in progress.

B2. Photometry of Pluto

A major effort was devoted to the observation of Pluto-Charon mutual events. Tholen and Buie, with assistance from Lark and Storrs, succeeding in observing thirteen different events that occurred during the 1986 opposition of Pluto. Most of these events were observed through a Johnson B filter with the 2.2-m telescope, while a few were observed through an ultraviolet-blue blocking filter with the #1 0.61-m telescope on nights that were primarily devoted to photometry of Comet Halley. Representative data sets are shown in Figures 6-8. Figure 6 shows the inferior event (Charon passing in front of Pluto) of 15 January 1986 UT. The ordinate is the mean opposition blue magnitude and the abscissa is the Plutocentric ephemeris time. Coverage began with Pluto rising at 4 airmasses and continued until the onset of astronomical twilight. With the light gathering power of the 2.2-m telescope, it was possible to obtain a photometric resolution of approximately 0.004 mag per minute. At this level of precision, small deviations from the best fit model lightcurve are detectable. In particular, the end of the event seems to be

4
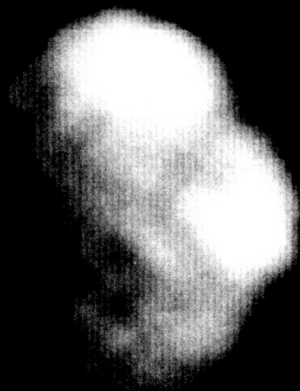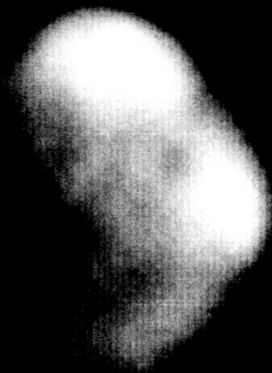
NEPTUNE 8900 A

21 MAY 1986

UH 2.23-METER

H.B. HAMMEL

11:14 UT

11:12 UT
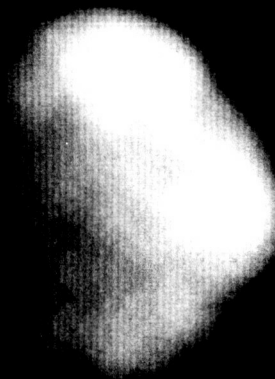
11:28 UT

NEPTUNE TIME SEQUENCES

20 May 1986 **4 June 1986**

11:53   10:27

13:10   10:58
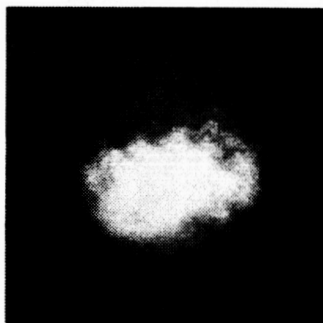
13:50   11:50
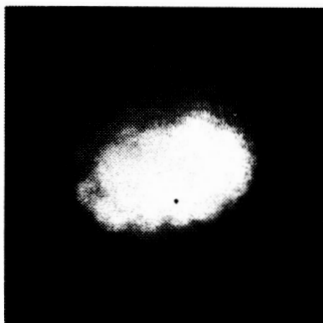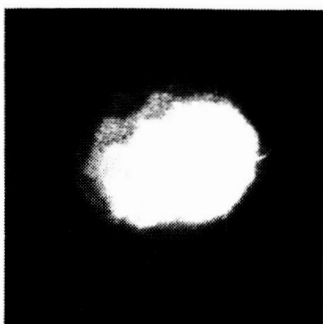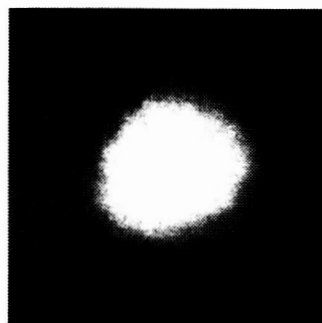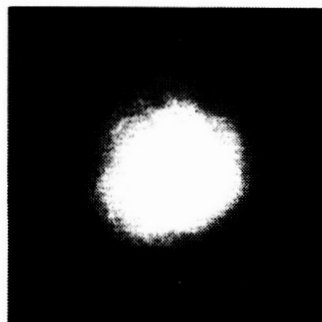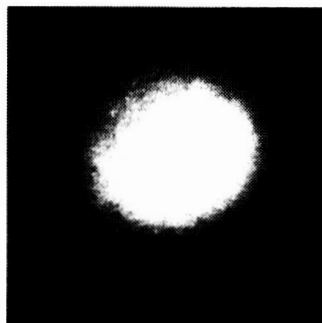
14:29   12:39
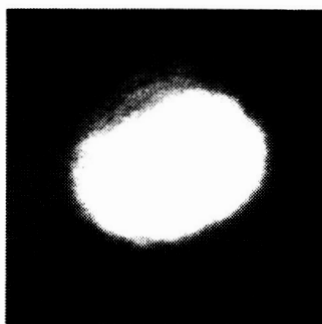
URANUS   21 MAY 1986

8900 A   8260 A

8900 A

LOW LIGHT

LEVELS

H.B. HAMMEL   U.H. 2.24-METER

Fig. 4

20 May 1986
Lat. = 38 ± 2 degrees
T = 17.4 ± 0.5 hours

4 June 1986
Lat. = 37 ± 2 degrees
T = 21.0 ± 0.5 hours

Planetary Central Meridian

Universal Time (hours)

Relative Longitude (degrees)

8

5·30

Profiles Across Uranus

8900 A (methane)

8260 A (continuum)

Data Numbers

Distance (arcsec)

Fig. 5

9
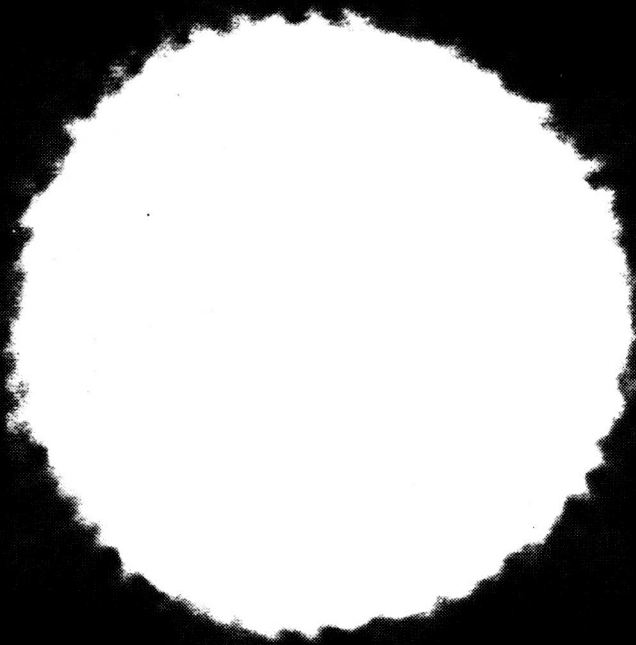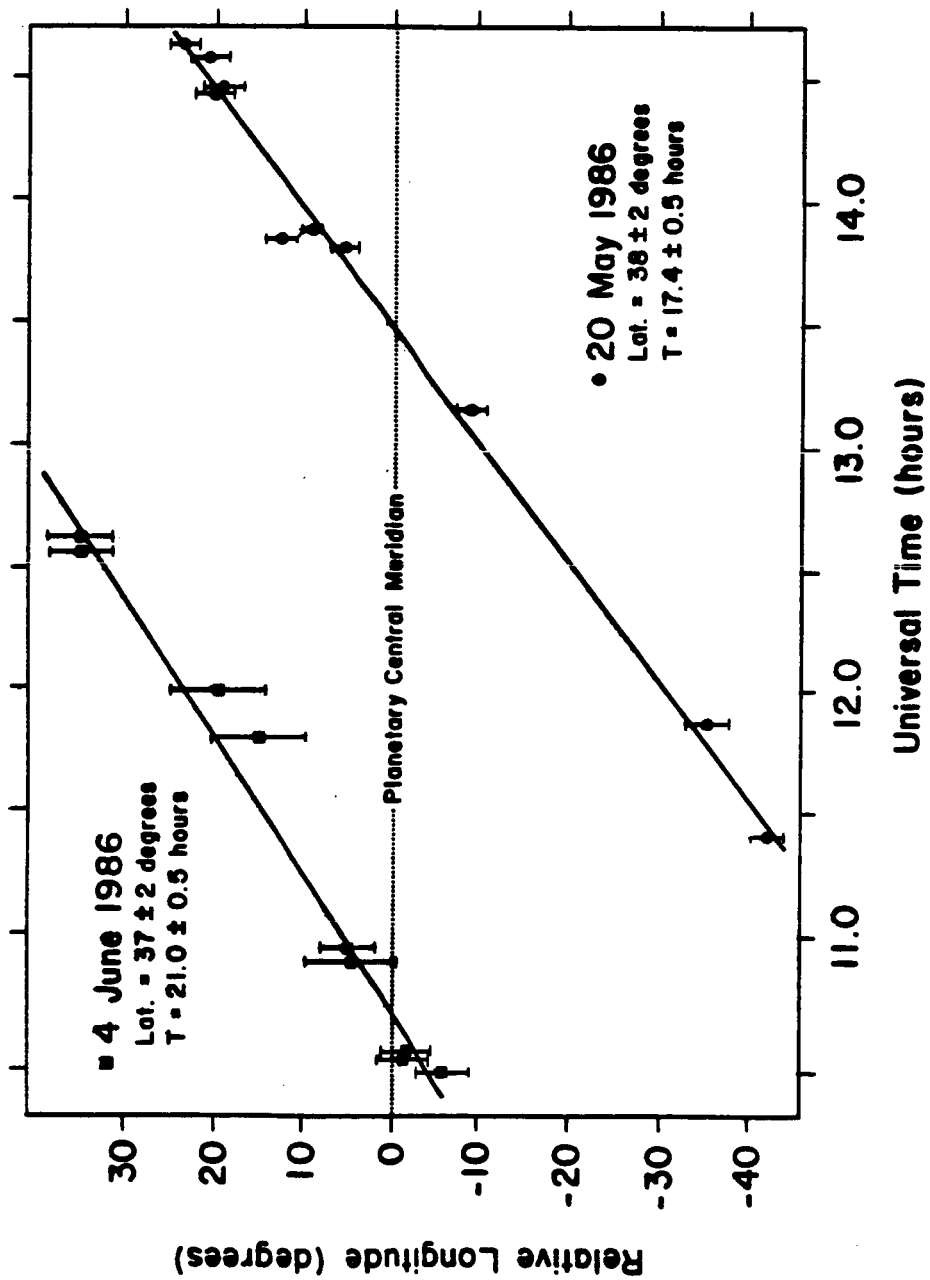
Fig~ 6.   Photometric observations of Charon passing
          in front of Pluto

1986 Jan 15 UT

Mag v.
Time

1986 Jun 11 UT

Fig. 7. Photometric observations of Charon passing in front of Pluto. See text for details.

Mag v.
, Time
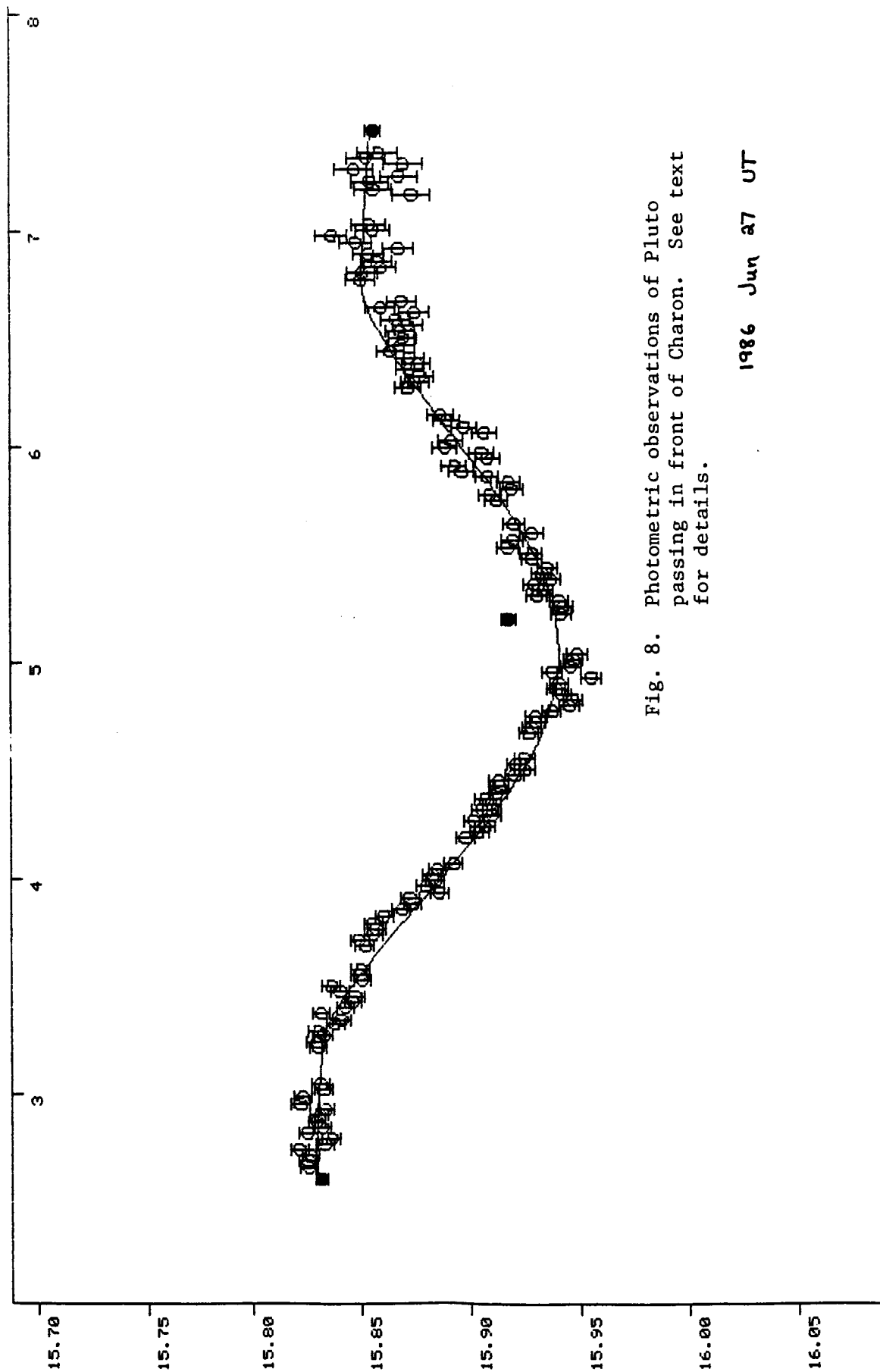
Fig. 8. Photometric observations of Pluto passing in front of Charon. See text for details.

1986 Jun 27 UT

Mag v. Time

12

systematically high compared to the model lightcurve (solid line), which may well be due to a dark spot on the southern limb of Pluto (see below).

Figure 7 shows the inferior event of 11 June 1986 UT. Again the abscissa is the Plutocentric ephemeris time, but this time the ordinate is a synthetic mean opposition blue magnitude. The data were actually obtained through the ultraviolet-blue blocking filter with the 0.61-m telescope. This filter transmits all light longward of about 5300 A. The GaAs photomultiplier tube used for all the observations begins to lose sensitivity rapidly longward of 9000 A and is essentially insensitive at 9300 A, so the effective bandpass of the filter-PMT combination is roughly 4000 A. This wider bandpass is necessary to increase the photon count rate to a high enough level to do useful time-resolved photometry with the 0.61-m telescope.

Figure 8 shows the superior event of 27 June 1986 UT observed with the 2.2-m telescope. The ordinate and abscissa are the same as for Figure 7. All but three of the data points were obtained through the blue filter. The remaining thre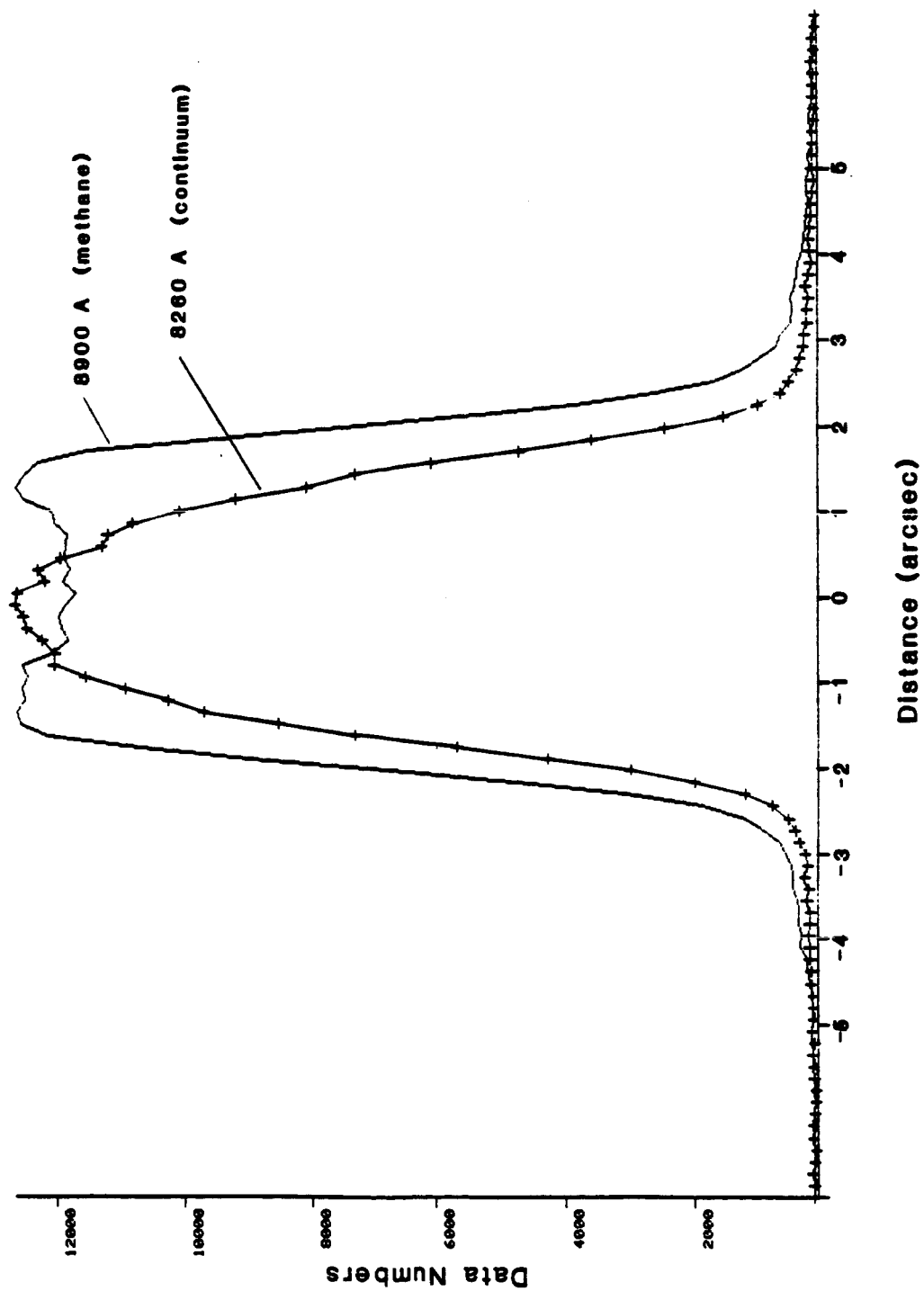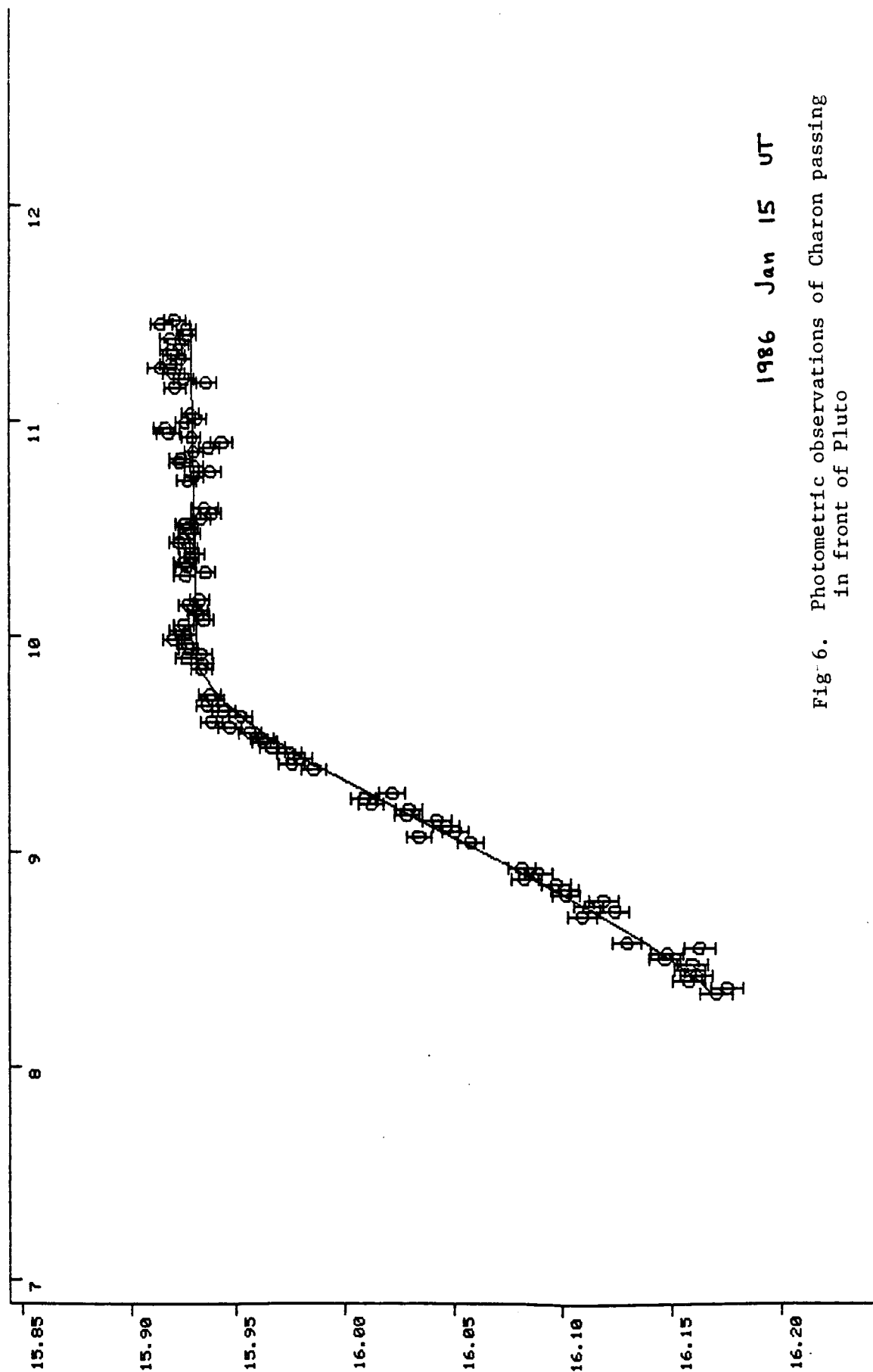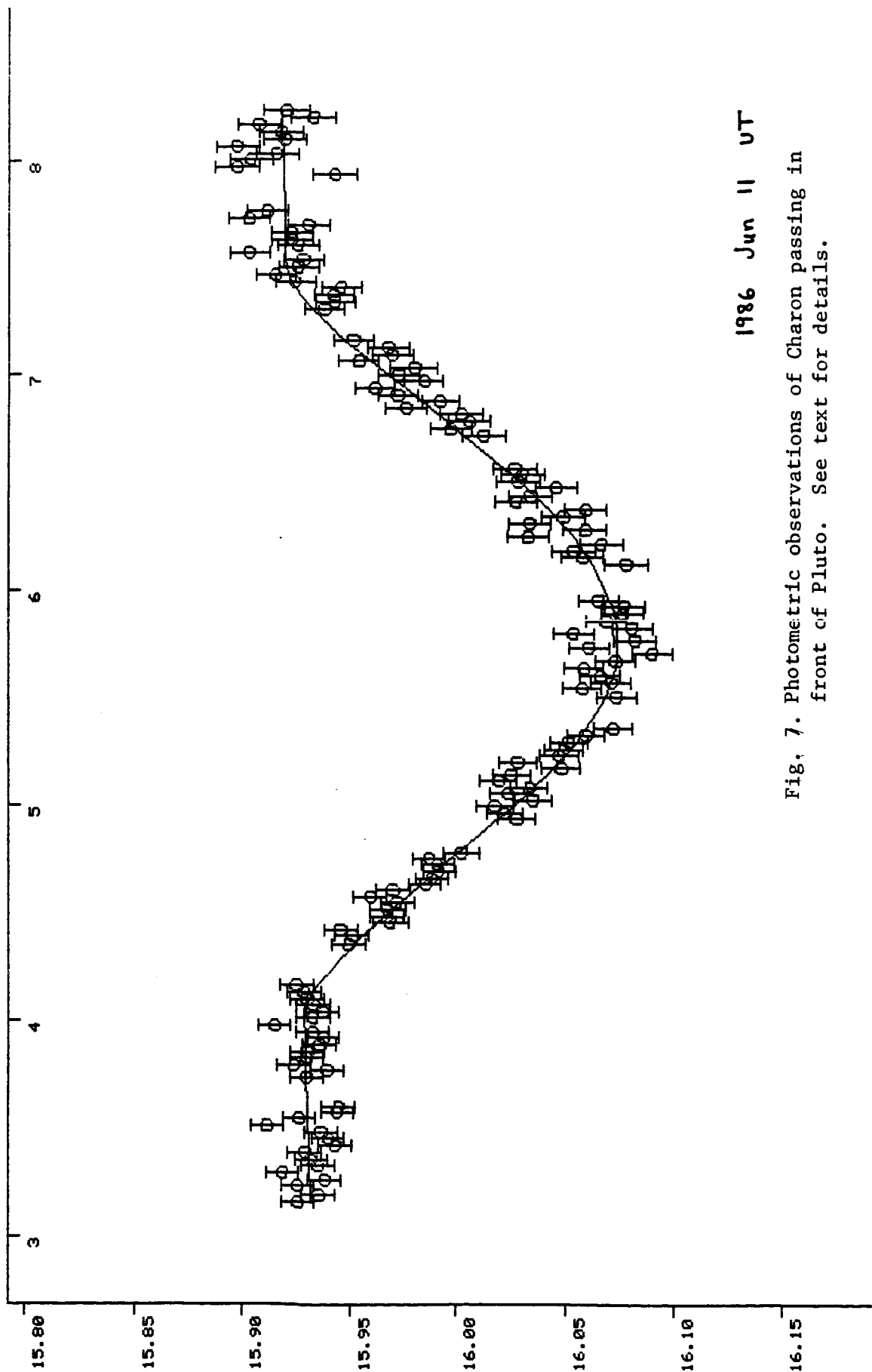e, shown as filled circles, were obtained with the blocking filter normally used at the 0.61-m telescope. These three points clearly show that the event depth is less in yellow light than it is in blue light, which means that Charon's reflectance spectrum is not as red as Pluto's reflectance spectrum. If the entire surface of Charon was the same color, however, an inferior event ought to be deeper in yellow light than in blue light. Figure 7 shows yellow light data plotted along with the blue light model lightcurve, and the data agree with the model rather well. Apparently the Pluto-facing hemisphere of Charon has a fairly neutral color, while the anti-Pluto hemisphere has approximately the same color as Pluto. Charon is yet another example of a solar system object with quite different hemispheres.

Figure 8 also shows a bump shortly after first contact, which may well be due to a small-scale surface albedo feature on Charon. Supporting data were obtained by R. Binzel at McDonald Observatory with their 2.1-m telescope. All data collected so far would seem to suggest that surface albedo features produce very subtle deviations from smooth model lightcurves, which means that large-aperture telescopes are required to extract such information from the mutual events.

Analysis of these data has yielded the most accurate values yet obtained for the various orbital and physical parameters for the Pluto-Charon system. These parameters are summarized in Table I. The derived density is surprisingly high. Given the water-ice compositions of many of the satellites of the outer planets and the methane-frost surface material known to exist on Pluto, most people were expecting the density of Pluto to be closer to 1.0 gm/cc. A density of 1.8 gm/cc would imply that at least half the mass of Pluto is due to rocky material, although further refinement of the density is necessary to place tighter constraints on the rock/ice ratio.

Table I

PLUTO-CHARON ORBITAL AND PHYSICAL PARAMETERS

a = 19,130   km   (assumed)

e = 0.0   (assumed)

i = 91.6   ± 1.6   deg ⎤ equator and equinox

Ω = 222.44   ± 0.15   deg ⎦   of 1950

L = 122.03   ± 0.22   deg

E = 2,446,600.5

P =   6.387204 ± 0.000047 days

Pluto   radius   = 1145 ± 46 km

Charon radius   = 642 ± 34 km

Sum of Pluto and Charon radii = 1786 ± 19 km

Pluto   blue geometric albedo   = 0.612 ± 0.017 ⎤ occulted material

Charon blue geometric albedo = 0.424 ± 0.018 ⎦   only

Pluto   reflectance spectrum: reddish

Charon reflectance spectrum: neutral (Pluto-facing hemisphere)

Mean density of system = 1.84 ± 0.19 gm/cc

Although observations of Pluto-Charon mutual events are being obtained worldwide, approximately 40% of all data have been collected at Mauna Kea since the onset of the events in late 1984.

The heavy observing schedule triggered by the appearance of Comet Halley provided us with a golden opportunity to monitor the rotational lightcurve of Pluto frequently. Altogether, Tholen and Buie collected 46 points on the lightcurve, which is shown in Figure 9. A detailed comparison of this lightcurve with the one assembled by Tholen and Tedesco from data collected between 1980 and 1983 shows that the lightcurve is continuing to evolve slowly. In particular, maximum light appears to have become slightly broader and brighter. These data have been used to develop a model for the surface albedo distribution of the entire surface of Pluto (see below).

Eventually, we hope to combine all data collected at various observatories worldwide to determine definitive orbital and physical parameters for the Pluto-Charon system. The success of this effort will be dependent upon how well each observers can transform their instrumental data to a common photometric system. To aid in this effort, Tholen and Buie have been selecting and standardizing comparison stars to be used worldwide during each opposition. In addition, a couple of transformation stars have been selected and are being standardized to help observers determine their color terms to the necessary precision.

Of course, to acquire Pluto-Charon mutual event data, one needs to know when to observe. One could simply add half-integer multiples of the orbital period to the time of one event to determine when future events will occur, but the changing geometry of the Earth, Sun, Pluto, and Charon produces time shifts that can lead to changes in the times of events by more than a half hour. Many observers require more accurate information regarding the times of the various contacts to plan their observations properly. Once again, the best available orbital and physical parameters were used by Tholen, Buie, and Swift to generate event circumstances for the 1987 opposition. This table of circumstances was published along with the selected comparison stars at the beginning of the 1987 opposition. Figure 10 is excerpted from that paper.

As the 46 new measurements of the brightness of Pluto have shown, the lightcurve continues to evolve. Persistent monitoring of the out-of-eclipse brightness is crucial to making the most of the mutual event observations. Buie has compiled a complete list of all Pluto photometry that spans the years 1953 to 1986. We now have a data base comprising over 340 points. A small excerpt from this data base is shown in Figure 11, where both the orbital lightcurve (formerly referred to as the secular dimming) and the rotational lightcurve are seen for different times since 1953.

A model was constructed to try and reproduce the lightcurve with a fixed surface albedo distribution. The model parameters include two bright polar caps, a dark equatorial band, and two spots near the equator. The sizes and

15

Rotational Lightcurve

Pluto - 1986

Period = 6.3872600 days

Mag v.
Rotational phase

Fig. 9

16

SUPERIOR

INFERIOR

Time
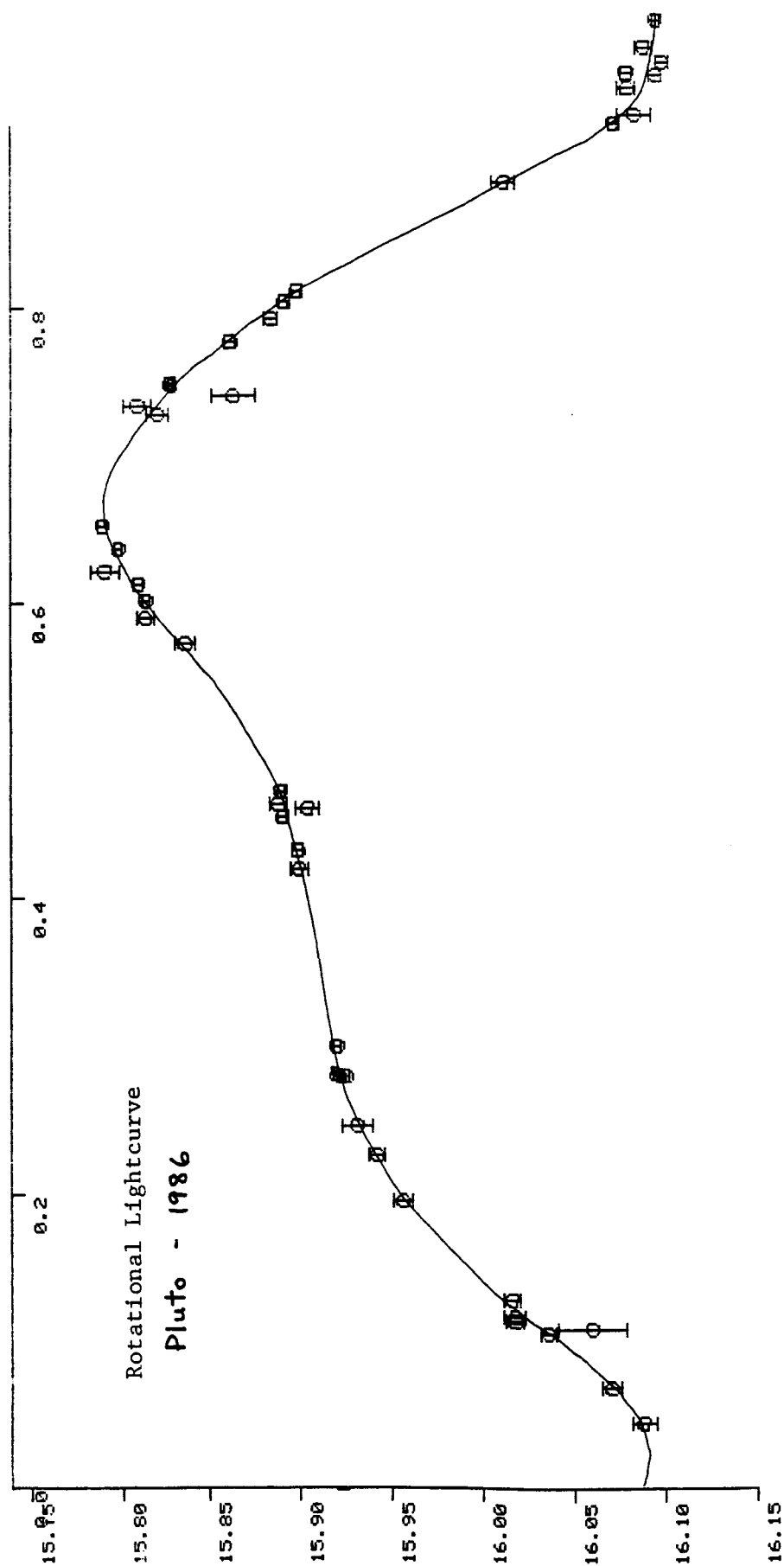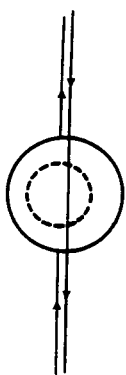
1987 Jan 30 12:30 UT
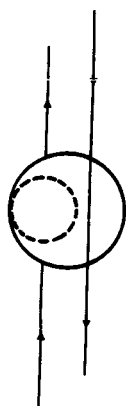
1987 Feb 02 17:24 UT

1987 Apr 29 22:52 UT

1987 May 03 03:20 UT

1987 Jul 28 09:03 UT

1987 Jul 31 13:41 UT

Fig. 10

Rotational Lightcurve of Pluto

Figure 11

18
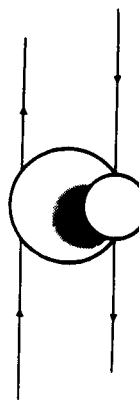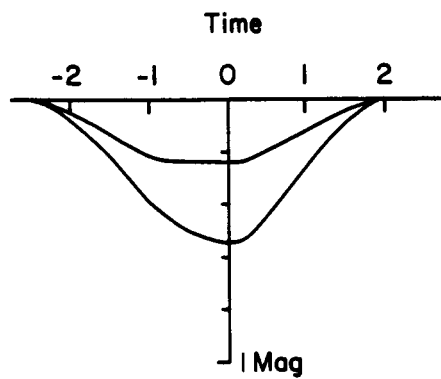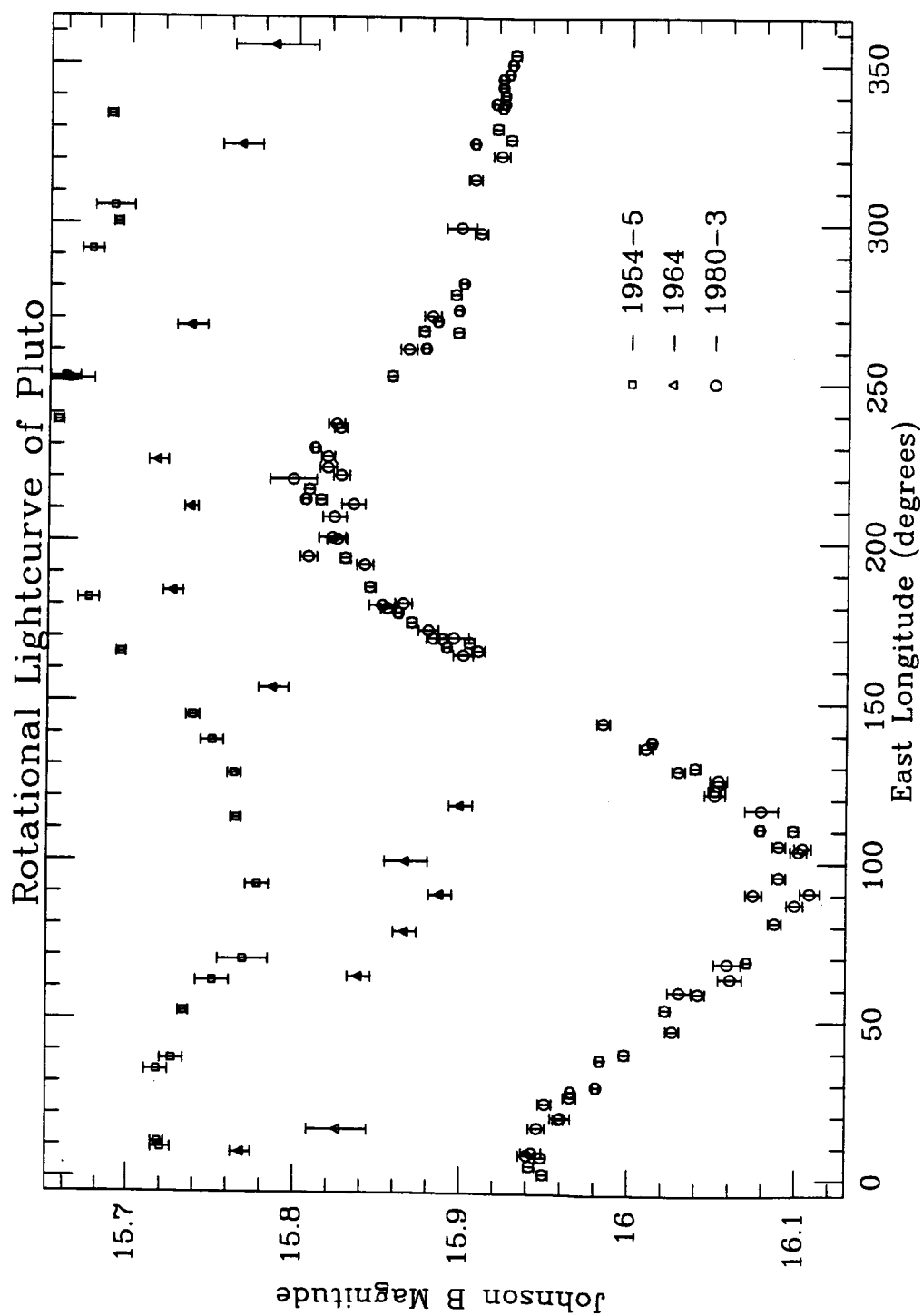
albedos of these surface features were optimized with a nonlinear least-squares analysis run on the CRAY XMP/48 at the San Diego Supercomputer Center. After more than 100 hours of execution time we have two possible surface albedo models that reproduce the the observed photometric behavior of Pluto to a high degree of accuracy. Table II summarizes the model parameters. The two models are very similar, with the only exception being the cause of the lightcurve from maximum light to the shelf near 330° E longitude. The smaller spot (#2) is either brighter than the equatorial band and causes the maximum or is darker than the background and is responsible for the shelf. Both models predict a dark equatorial band which has accurately predicted that the mutual events in 1987 would not be as deep as predicted by Tholen, Buie and Swift. With data of the quality that has been taken at the 2.2-m on previous events it will be possible to discriminate between the two models when the geometry is right sometime in 1987 or 1988.

Figure 12 shows an example of the quality of the model fit to the data. The fit is in general this good for all of the data. When grouped by the year of observation the typical residual is about 0.01 mag with some of the better years as low as 0.007 mag. For the first time we have a model that can explain the lightcurve of Pluto with geometry and a surface albedo model. We have generated some synthetic images of Pluto from the surface albedo model. A view of the shelf model can be seen in Figure 13. These are all equatorial views of Pluto with each image at 90° from the previous. In all images planetary North is up; this is intended to be a view that one might see from a spacecraft.

B3. Stellar Occultations

A number of predicted stellar occultations by Uranus, Neptune, and Pluto were observed by Buie, Tholen, Cruikshank, and W. K. Hartmann.

Confirmation of a dip in the signal as due to ring material generally requires observations at two different telescopes. For a subset of t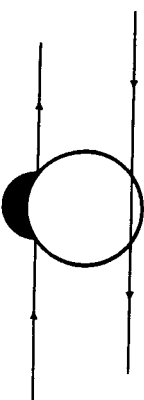he observations made at the IRTF, supporting observations were made at the 2.2-m telescope through an 8600-Å filter. Both Uranus and Neptune are much brighter at 8600 Å than at 2.2 μm, so the signal-to-noise ratio (SNR) is much lower. Although events corresponding to full extinction of the star could have been detected, the SNR was inadequate to confirm any of the short-duration partial-extinction dips seen in the IRTF data.

A stellar occultation by Pluto was predicted to occur over the Pacific region on 30 April 1986 UT, and the nominal ground-track was predicted to pass over Mauna Kea. We monitored the occultation star from both the IRTF and the #1 0.61-m telescope under marginal photometric conditions, but unfortunately no event was seen. Even though mutual event photometry of Pluto is yielding size information, a stellar occultation remains a valuable tool that provides a way to probe the atmosphere of Pluto, should one exist.

19

Table II

		Results of Square-Well Ring Profile Fits to 26 April 1986 Observations IRTF						
Ring	Event	Midtime (UTC)	Width (km)	Equivalent Width E (km)	Equivalent Depth A (km)	Fractional Transmission f_0	Normal Optical Depth	True Anomaly (deg)
6	I	13:38:59.456 ± 0.001	1.53 ± 0.08	0.56 ± 0.01	0.70 ± 0.01	0.63 ± 0.02	[0.46]	238.9
6	E	15:00:16.210 ± 0.001	1.66 ± 0.08	0.55 ± 0.01	0.67 ± 0.01	0.66 ± 0.02	[0.40]	130.5
5	I	13:38:24.221 ± 0.001	1.92 ± 0.05	1.10 ± 0.01	1.64 ± 0.03	0.42 ± 0.02	[0.86]	253.0
5	E	15:00:54.313 ± 0.001	1.77 ± 0.04	1.05 ± 0.01	1.61 ± 0.03	0.40 ± 0.02	[0.91]	143.8
4	I	13:37:52.645 ± 0.001	2.56 ± 0.03	0.91 ± 0.01	1.13 ± 0.01	0.64 ± 0.01	[0.44]	181.2
4	E	15:01:17.215 ± 0.003	1.66 ± 0.10	0.84 ± 0.03	1.18 ± 0.05	0.49 ± 0.03	[0.71]	71.4
α	I	13:34:50.183 ± 0.001	6.98 ± 0.02	3.83 ± 0.02	5.59 ± 0.03	0.44 ± 0.01	[0.80]	273.1
α	E	15:04:27.639 ± 0.001	10.32 ± 0.03	4.64 ± 0.03	6.20 ± 0.04	0.54 ± 0.01	[0.60]	159.6
β	I	13:33:27.657 ± 0.001	11.30 ± 0.03	2.94 ± 0.02	3.41 ± 0.02	0.74 ± 0.01	[0.30]	177.3
β	E	15:05:44.903 ± 0.001	8.02 ± 0.03	3.01 ± 0.03	3.78 ± 0.03	0.62 ± 0.01	[0.47]	62.2
η	I	13:31:21.111 ± 0.002	2.71 ± 0.06	0.74 ± 0.01	0.87 ± 0.01	0.72 ± 0.01	[0.32]	187.7
η	E	15:07:54.030 ± 0.002	3.30 ± 0.08	0.75 ± 0.01	0.85 ± 0.01	0.77 ± 0.01	[0.26]	70.3
γ	I	13:30:42.779 ± 0.001	2.15 ± 0.03	1.94 ± 0.01	5.18 ± 0.25	0.09 ± 0.01	[2.41]	118.5
γ	E	15:08:31.954 ± 0.001	2.09 ± 0.03	1.92 ± 0.01	5.46 ± 0.32	0.07 ± 0.01	[2.61]	0.4
δ	I	13:29:47.150 ± 0.001	2.77 ± 0.03	1.94 ± 0.01	3.40 ± 0.05	0.29 ± 0.01	[1.23]	24.1
δ	E	15:09:28.091 ± 0.001	3.31 ± 0.01	2.38 ± 0.01	4.25 ± 0.06	0.27 ± 0.01	[1.28]	265.1
ε	E	15:13:46.828 ± 0.003	82.47 ± 0.07	52.90 ± 0.17	85.38 ± 0.47	0.35 ± 0.01	[1.04]	133.6

Notes:
1) I and E stand for ingress and egress, respectively.
2) Numbers in square brackets were derived from other parameters in the fit.
3) True anomaly based on ring orbit model of French et al (1986) (in preparation).

20

Pluto–Charon Spot Model

o – Observational Data
× – Model Calculations

East Longitude (degrees)

Johnsonn B Magnitude

Figure 12

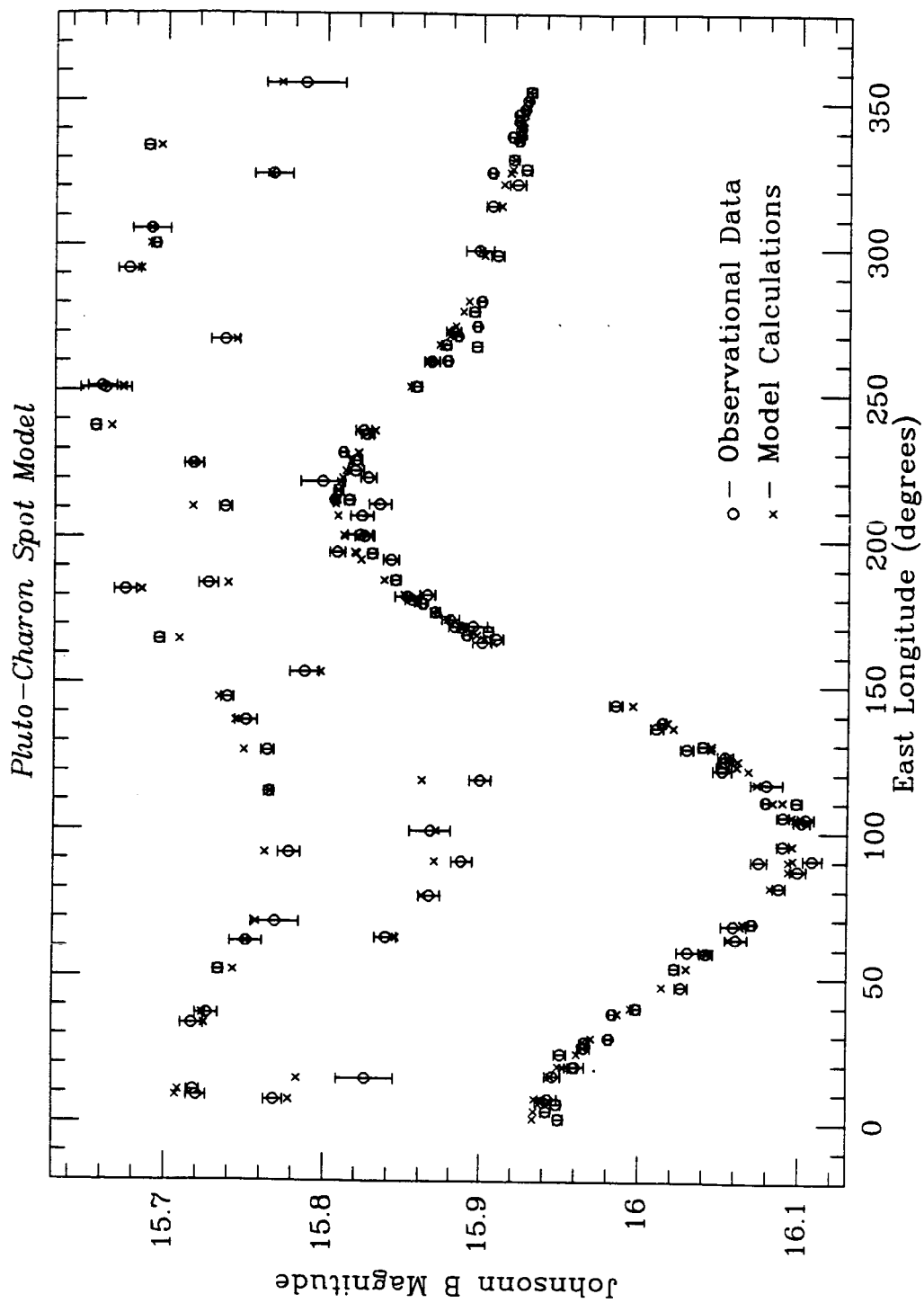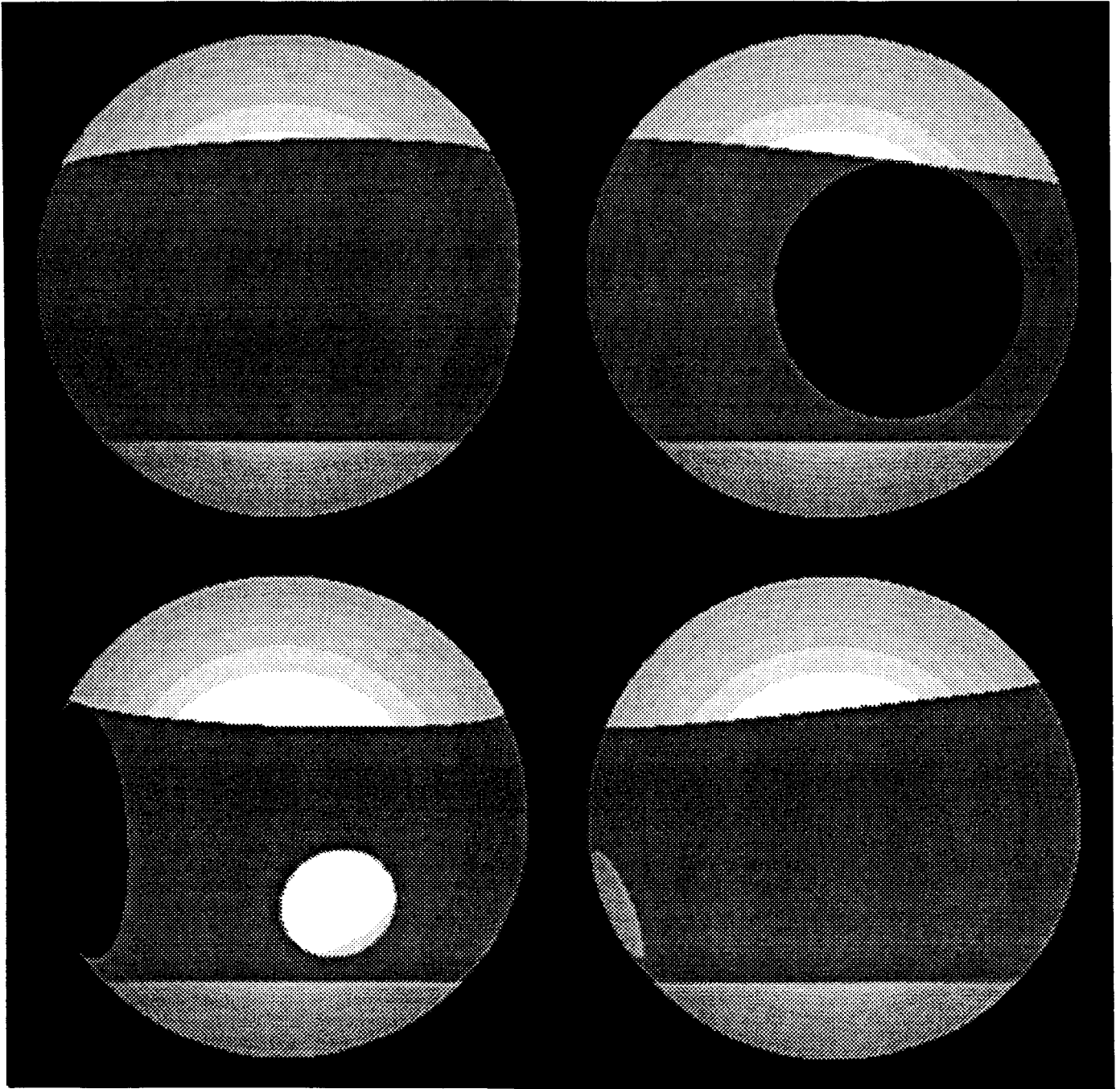## Pluto Spot Model

/scr/tests/_rbig
8BIT   CLIP
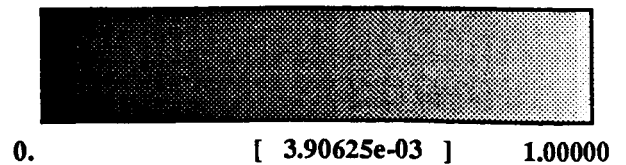
Wed Apr 8 10:02:53 1987

0.   [3.90625e-03]   1.00000

Figure 13   22

C. PLANETARY SATELLITES AND RINGS

C1. Eclipse Observations of Io, the Thermal Inertia of the Bright Regions, and Changes in the Thermal Output of the Loki Volcano

In the report of this grant from last year, Sinton reported that he got satisfactory agreement with the observed eclipse cooling and heating curves of Io only when a two-albedo model was used and that the best agreement, which was statistically significant, was found when the different albedo regions had different thermophysical parameters as well. It was found that the bright regions probably had ten times the thermal inertia of the dark regions. One possible conjecture for this difference is the presence of SO_2 gas in the interstices between particles. This possibility will be discussed later in this report in a section G.

The thermophysical parameters were determined solely from the extensive data set obtained in 1983. An important test of any model is whether it has predictive ability, i.e., if parameters are changed does it give agreement with observations. A parameter that does change significantly from year-to-year is the distance of Jupiter, and hence Io, from the Sun. In 1981 Jupiter was at aphelion; in 1986 it was at perihelion. This results in a distance change of nearly 5% and an insolation change of nearly 10%. Although this is a relatively small change in total flux, it will have larger consequences at 8.7 μm, a wavelength that is considerably shorter than the blackbody maximum for Io's normal emission and an even smaller fraction of the wavelength of the radiation peak when Io is eclipsed. Thus, with the change in solar distance from 1983, when the model parameters were set, to the 1986 observations we expect a substantial increase in the predisappearance flux from Io and an even greater change in the decrease in flux accompanying the eclipse.

Sinton and Charles Kaminski have continued their program of making IRTF observations of eclipse disappearances and reappearances. Their results for 1983 and 1986 are shown in Figure 14 along with the model predictions. Notice the marked increase in the depth of the eclipse between 1983 and 1986 not only in the model curves but also in the observational data. The only change in the model was the indicated change in the solar distance, R. The model, as mentioned, was fit to the 1983 data, not only at 8.7 μm but at four other wavelengths out to 30 μm. The solar distance effect is much smaller at these wavelengths, as expected, and the model is in good agreement with the observations at the longer wavelengths.

Another striking difference between the 1983 data and curves and those is the "jump" in the middle. The jump is a consequence of the thermal emission of the volcanoes, and the change in the aspect of these between observations made at an eclipse disappearance at a phase angle of ~9° before opposition to those made at a reappearance at a similar angle after opposition. The model
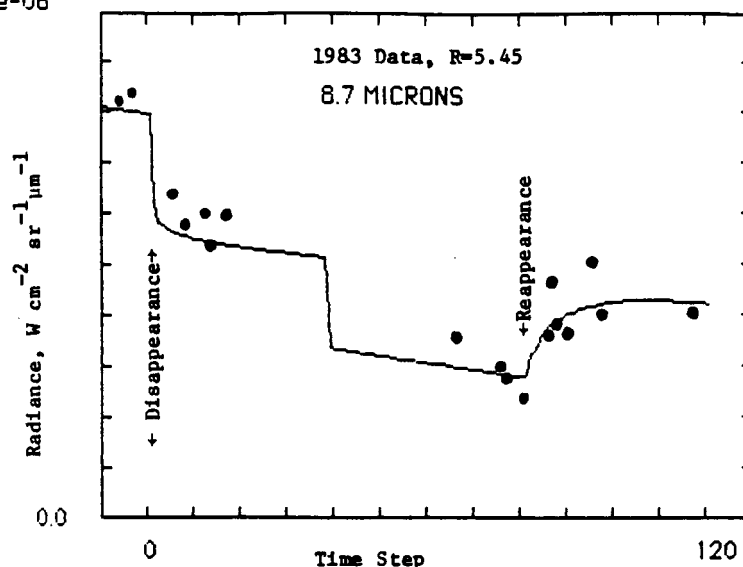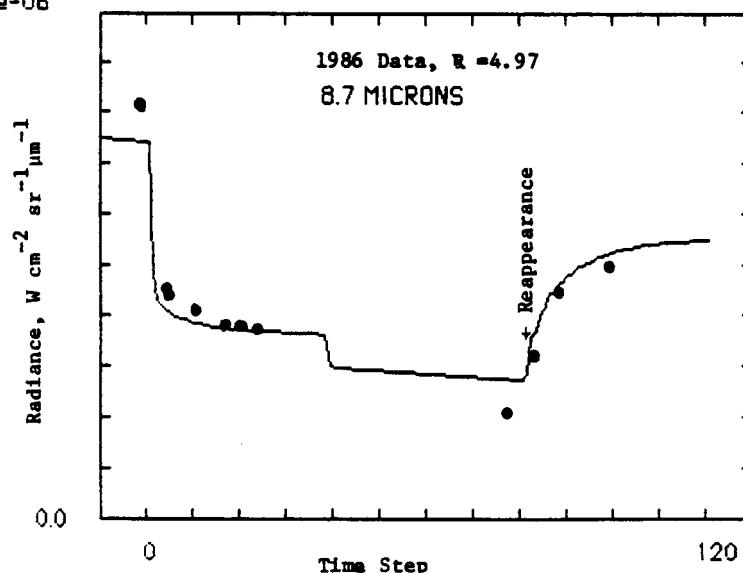
Figure 14. Observations at 8.7 μm of eclipses of Io in 1983 and 1986 compared. The thermophysical model parameters were established from the 1983 data (obtained when the Io-Sun distance was 5.45 AU). They not only fit the 1983 data, but they also provide a good fit to the 1986 data (when the Io-Sun distance was 4.97 AU). Note the marked change in the depth of the eclipse between the two epochs. The "jump" in the middle of the curves is due to the change in aspect of the volcanic sources between viewing them at disappearances and reappearances. The amount of the required step is a measure of the amount of volcanic thermal emission. The amount decreased markedly in 1986 compared to previous years.

24

curves partake in this change between the two seasons because the parameters specifying the volcanic emission are fitted by a least-squares routine, while the thermophysical parameters were not changed. The observations at the other wavelengths and the inferred volcanic flux also changed markedly in 1986. Since the results from 1980 to 1984 showed that the principal source of volcanic thermal emission as seen in eclipse observations arose from the Loki volcano, we infer that there has been a marked decrease in the flux from Loki. These data are summarized in Table III, which gives the model "volcanic" parameters for each year.

In most cases it has been possible to solve for the equivalent circular size, temperature, and longitude of both a hot source and a warm source. The longitudes are obtainable from the fact that the aspect and the accompanying foreshortening factor are different for the observations at disappearance and reappearance. In most cases the longitudes are near to that of Loki. The Voyager 1 IRIS instrument found that Loki was, perhaps, the most productive of thermal output and that if eclipse observations had been made in 1979 Loki would have been responsible for 75% of the observed flux. The penultimate line in Table III is particularly accurate. The number depends on model fitting of the flux observed at seven different wavelengths from 2.2 to 20 μm.

It is notable that the observed volcanic flux dropped markedly in 1986. Such a large drop can only have been produced by a marked decrease in the output from Loki. It is also significant that the longitude of the warm source has shifted to 334° W. During the Voyager observations there were several important sources, such as Creidne Patera, west of Loki. If there were a decrease in the flux from Loki, then a westward shift in the effective longitude of a single source, as in the model, would be expected. The hot source has also decreased in area and in power output. The longitude has not shifted. During the Voyager swing-by, the other sources near to Loki that would have been visible during an eclipse did not have a high-temperature component. Thus if Loki decreases its output, then no shift of effective longitude is expected for the hot source. We will see in the discussion of the polarization observations made in 1986 (section C3) that they, too, show a marked decrease in Loki activity.

C2. Further Reduction of Occultation Observations of 1985

Goguen, who is now at JPL, has been collaborating with Sinton in continuing the reduction of the set of observations of the 1985 occultations of Io by other satellites. Considerable progress has been made in the refinement of the relative positions of the two satellites (Io and the one that occulted it). Precision of location along the relative track of occultation has now achieved a precision of about 10 km. Thus the occultation method, in the rare

Table III

Volcanic Fluxes, Loki and Environs, 1980-1986

Parameter		1980	1981	1982	1983	1984	1986
Size, hot source,	(km)	30	10	28	34	17	7
Temp., " "	(°K)	564	522	[600]	541	[600]	555
Longitude," "	(deg W)	305	[310]	293	304	[310]	305
Size, warm source,	(km)	382	150	202	197	150	110
Temp., " "	(°K)	250	368	297	292	360	345
Longitude," "	(deg W)	[310]	[310]	312	316	[310]	334
Power, hot source	$(10^{13}$ W)	0.40	0.04	0.30	0.44	0.16	0.02
Power, warm "	$(10^{13}$ W)	2.55	1.83	1.42	1.26	1.69	0.76
Total power	$(10^{13}$ W)	2.95	1.86	1.87	1.70	1.85	0.79
Std. err. of above	$(10^{13}$ W)	0.27	0.06	0.08	0.06	0.10	--

Note: Bracketed quantities are assumed, the remainder are solved for.

instances when it can be applied, produces a precision in the location of volcanoes that is nearly an order of magnitude greater than the best Voyager IRIS resolution on Io. The final results are not yet in, but an example of a well-observed occultation is shown in Figure 15. This event (occultation of Io by Callisto that occurred on 10 July 1985) was observed at four telescopes on Mauna Kea at four wavelengths. A new volcano was found, and its position is 85° W and 25° S in a region that was poorly observed during the Voyager encounter. The volcano has now been located in the 8.7 μm curve, as well as in the 3.8 and 4.8 μm curves that were shown in the report last year. A high time resolution of the disappearance of the volcano behind Callisto's limb is shown as Figure 16. It is clear that the hottest part of the volcano is about 10 km in diameter. From the combination of the 3.8 μm data with the 4.8 μm data a color temperature of about 700 K and effective diameter of 10 km are obtained.

C3. Observations of the Polarization of Io at 3.8, 4.8, and 10 μm.

The light emitted by a dielectric (lava, for example) is polarized as a consequence of the Fresnel reflection laws. As a consequence the emissivity, which is one minus the reflectivity, is different for the viewing plane that contains the surface normal from that of the orthogonal plane. Goguen and Sinton previously used this fact to locate several volcanic sources on Io (1985, Science 230, 65-69). Location of sources is possible because as Io rotates on its axis, the plane of polarization will also rotate but in a manner that is uniquely related to the latitude and longitude of the source. Sinton and Goguen, in collaboration with B. Ellis (University of Texas), attempted to extend these observations on the IRTF this past year using the Ames Laboratory polarimeter, and, in collaboration with T. Nagata (formerly with Kyoto University; now at the IFA), with the Kyoto polarimeter on the UKIRT. Polarization of Io was measured at both times. The observed values, however, were much smaller than obtained earlier, and the position angle of the plane of polarization did not change with time throughout the night as expected. It now appears that the polarization that was observed this year was largely not due to emission from volcanoes. Rather, it was due to residual polarization of the reflected sunlight. This was observed, even though the time of making the observations was selected so that the solar phase angle was only about 1°-2°. Previously, we had felt that this requirement would ensure reduction of polarization of the reflected background light to a negligible amount. At very small phase angles, the plane of polarization is expected to be parallel to the Earth-Io-Sun plane. Figure 16 shows the position angle of this plane and the observed direction of Io polarization at 3.8 μm as a function of time. It is clear that the observed direction tracks the changing direction of this plane, which swings through nearly 180° as Io passes through opposition.
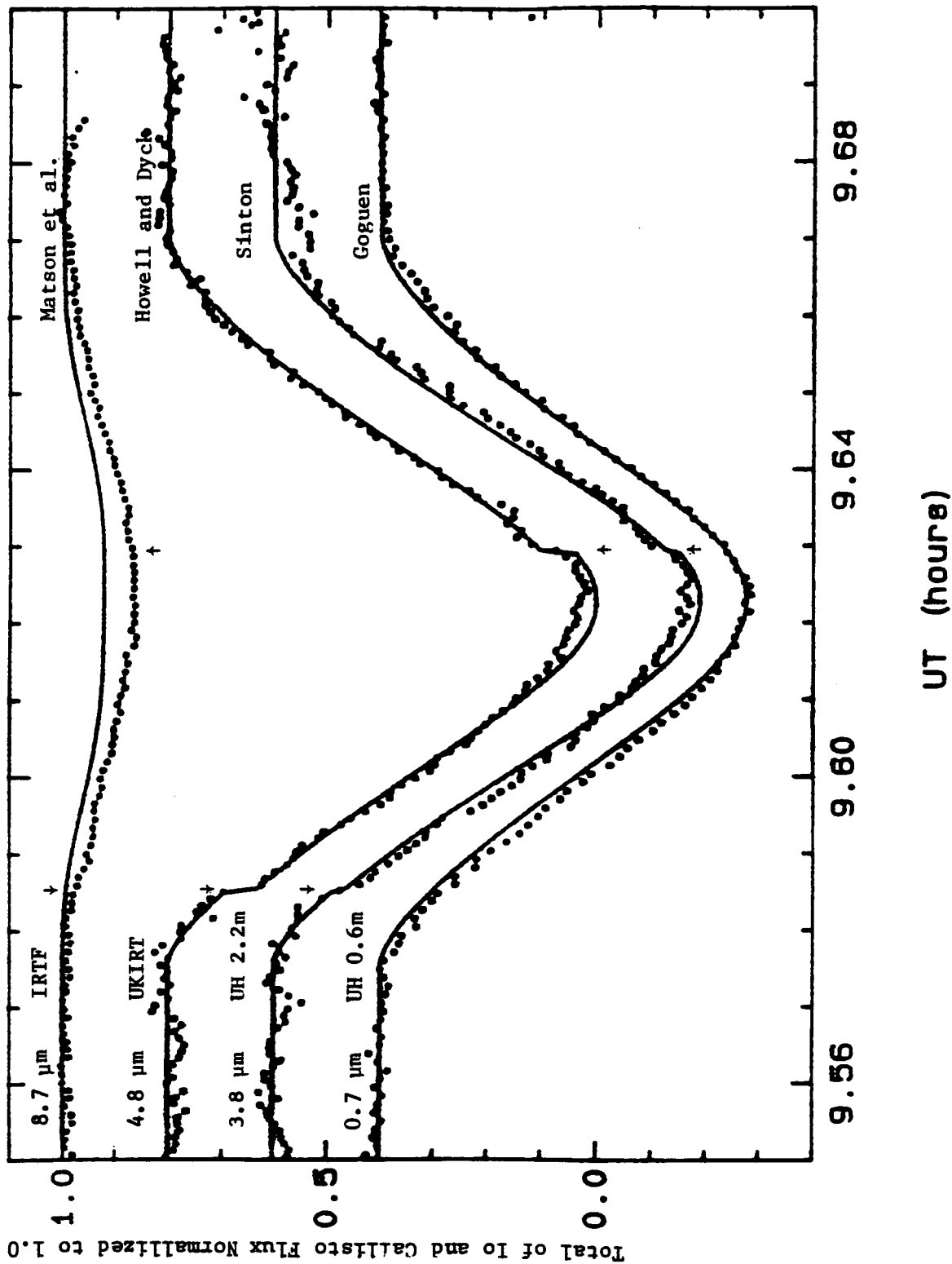
Figure 15. Model fits to the occultation of Io by Callisto that was observed at four wavelengths with four telescopes on Mauna Kea on 10 July 1985. All three infrared wavelengths exhibit sudden changes (arrows) of signal level as a volcano ingresses and egresses behind the limb of Callisto. The model fitting allows the determination of the center-to-center distance of Io and Callisto to within about 10 km. From the precise fitting, the coordinates of the volcano can be obtained. The volcano had not been observed before, as it was in a region that was poorly observed by the Voyager spacecraft.
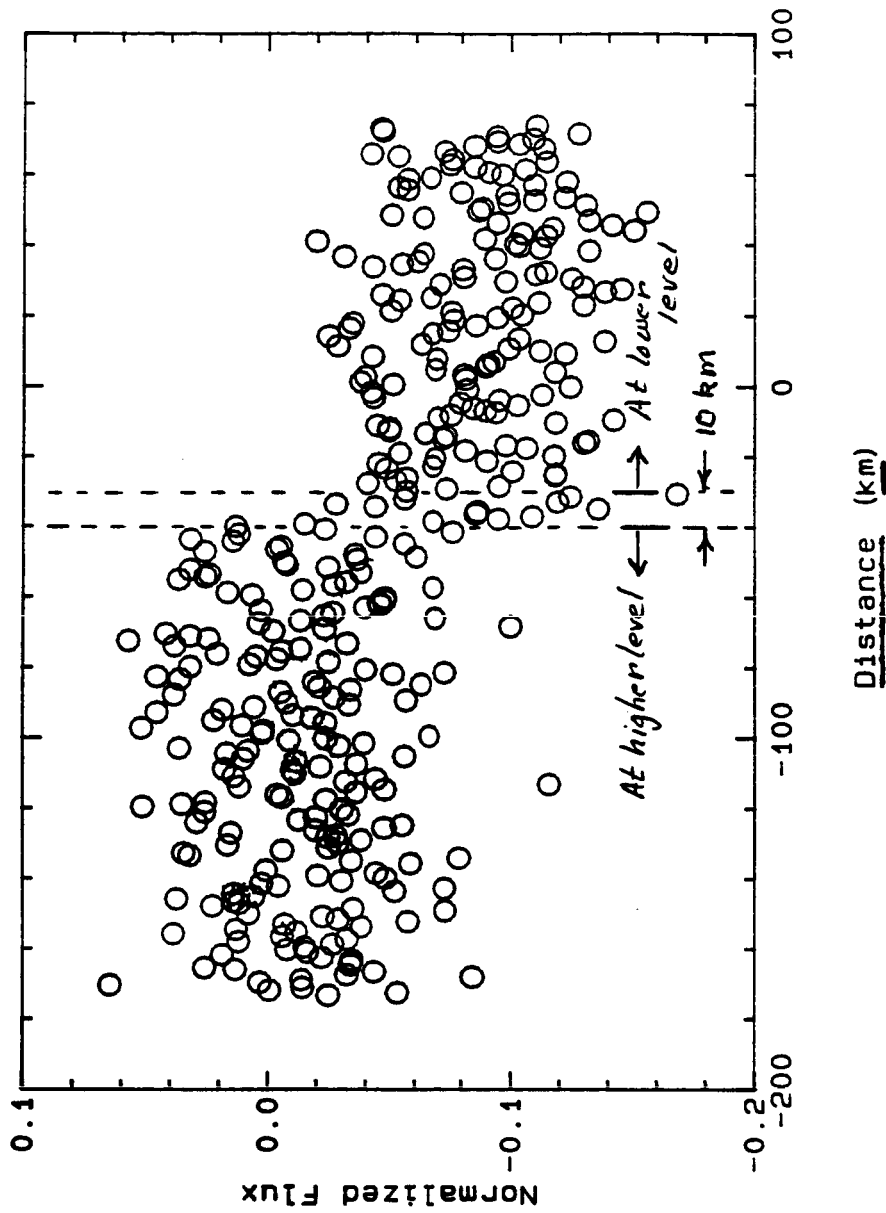
Figure 16. The ingress of the volcano from the 4.8-μm curve at high time resolution. The slope of the smooth part of the occultation model curve has been removed from the observed data, which have been plotted at 0.05 sec intervals. The transition between the higher level and the lower level takes place within 10 km of motion of Callisto's limb. Thus, the volcano is about 10 km or less in diameter. The resolution shown here is nearly an order of magnitude greater than the best obtained with the Voyager IRIS instrument.

The amount of polarization observed at either 3.8 or 4.8 μm was never more than 0.4%. In the 1984 observations the polarization produced by Loki was observed in amounts up to 1.6%, and the maximum polarization, which was at rotational longitudes of Io that were not observed, would have been about 2.5%. In the new observations we did acquire data when the polarization due to Loki would have reached the maximum value, and yet we never observed more than the above mentioned 0.4%. We conclude from these data that the amount of near-IR flux from Loki in 1986 was small enough that its contribution to the overall polarization of Io was negligible and that the thermal emission from Loki was at a low ebb in 1986. This conclusion is identical to that found from the eclipse observations discussed in an earlier section of this report. In view of the measurement of the residual background polarization, possible only because of the ebb of volcanic activity, we can now go back and correct our 1984 data for this polarization. We have not done this as yet. It is clear, however, that the correction will not change the major results of the paper. The correction will probably make invalid our determination of the location of a second source on the hemisphere that includes Loki.

Sinton has collaborated with David Aitken of the University of New South Wales, Australia, in interpreting observations that the latter made of the polarization of Io at 10 μm. Sinton had earlier advised Aitken exactly when to observe to have the maximum polarization from Io, which Sinton chose as the above mentioned rotational longitude for the maximum due to the Loki volcano. Aitken was able to make spectropolarimetric observations at that time and measured Io polarization between 8 and 12 μm. The observed broad-band polari-zation was about 0.5%. The spectrum of Io can be resolved into two com-ponents, one due to background thermal emission at 138° K and one at 336° K. The latter is presumably due to volcanic emission. The position angle of the polarization is within 2° of the polarization expected from Loki. Note that in this spectral region, there will be no contribution of reflected sunlight and so no polarization from that source is expected. However, there might be a residual polarization of the background thermal flux. If there were such polarization, the expected position angle would be 45° from that observed.

C4. Europa, Ganymede, and Callisto: Photometry at 3.8 and 4.8 μm

Last year we reported that Ganymede had a most remarkable linear phase effect of 0.08 mag/degree at 4.8 μm and 0.05 mag/degree at 3.8 μm. Based on one chance, rather bright observation at a phase angle of 5°, we conjectured that Europa might have an even greater phase dependence of about 0.4 mag/degree, even though it had been difficult to detect in earlier IRTF observa-tions at phase angles near to 10°. To test this hypothesis, observations were scheduled with the 2.2-m telescope at a phase angle of 2° since data were com-pletely lacking for angles <5°. The observations on two separate nights gave

4.8-µm magnitudes of 7.37 ± 0.25 and 7.21 ± 0.13. These data, when combined with IRTF data at 10° phase angle, yield an unremarkable linear phase dependence of 0.03 mag/degree that is not well determined and could be much larger but not so large as to have been responsible for the "bright" observation.

What then was responsible for the earlier bright observation at 5° phase angle? We have been unable to attribute the observation to a misidentification of satellites. The telescope positions were recorded by the software, and the observation was among several made of Europa at different wavelengths that are consistent. The telescope position was consistent with the position of Europa when compared to the indicated positions of the other satellites, which were observed at the same time. Moreover, there are no catalogued infrared sources in that region with which it could have been confused. The observation was made on 23 April 1981 at 9:03 UT and gave a M magnitude of 6.12, which is about 1.8 mag or a factor of 5 brighter than expected from the phase curve that was derived from other observations. At this point we might presume that there was an "outburst" from Europa on that night. However, there is one other fact that distinguishes the 23 April observation. It was the only observation that was made with the IRTF bolometer rather than with the InSb detector. It is possible, though it has not been reported, that there is a "red" leak in the 4.8-µm filters. The red leak would cause no problem when used with the InSb detector, but if the leak occurs beyond 12 µm it could cause a misinterpretation of results when used with a bolometer detector on cold solar system objects that are dark at 4.8 µm. Thus, at this time, we cannot say whether there was an outburst from Europa.

The earlier phase dependences of Ganymede and Callisto were confirmed in the new measurements at small phase angles. An interesting result of the new observations is that the "opposition surges" observed in the visible on almost all solar system objects are absent in observations of the Galilean satellites at 3.8 and 4.8 µm.

C5. Charon

Analysis of the Pluto-Charon speckle data collected in 1985 by R. Goody, J. Beletic, and Tholen was completed. Goody and Beletic (Harvard University) developed techniques to compensate for instrumental effects (such as phosphor persistence) in the PAPA camera, and final processing of the seven nights of Pluto-Charon speckle imaging was performed. Altogether 54 pairs of positional coordinates were extracted from the data, which makes it the largest, most homogeneous, and best calibrated speckle data yet obtained on the Pluto-Charon system. Tholen added these new data to the existing data set and performed another orbit improvement for Charon. The new data show the orbital radius to be slightly larger than previously determined, and the orbital inclination is somewhat higher. A paper describing these observations and results in currently in preparation.

C6. Outer Satellites of Jupiter

Although we had hoped to obtain new data on the outer Jovian satellites, Jupiter's opposition fell at a time that coincided with the Heidelberg Halley Symposium, the Paris DPS meeting, and the preparations for these meetings.

C7. Studies of Triton

In a continuation of the ongoing observational studies of Neptune's satellite Triton, Cruikshank, in collaboration with A. T. Tokunaga and R. G. Smith (IFA) and R. H. Brown of JPL, made new observations with the cooled-grating array spectrometer (CGAS) on the IRTF in May and August 1986. The CGAS was used with a 32-element detector array, which was arranged to cover the entire spectrum between 2.0 and 2.5 μm. This is the region of the spectrum that shows the strong 2.3-μm methane band and the 2.15-μm feature that we have attributed to the density-induced absorption in molecular nitrogen. In Figure 17 we show the data from these observing runs; see the captions for details.

The main characteristics of the new spectra are evident in the figures. The methane band at 2.3 μm is now seen with at least three distinct components. While it is not fully resolved, the band does show features not visible in the earlier data taken by Cruikshank and others with circular variable filter spectrometers. To study the new spectrum in some detail, we require comparison spectra of methane in various states. In Figure 18 we show the Triton average spectrum in comparison with laboratory spectra of liquid nitrogen and with methane dissolved in liquid nitrogen. The quantity of methane dissolved in each sample in Figure 18 is indicated in grams/liter. With concentrations of methane amounting to less than about 1.5% of the saturation value, the transmission spectra show the density-induced molecular nitrogen feature with a central wavelength of 2.15 μm, but as the concentration of methane is increased, the 2.3-μm methane band increases in strength and width so that the nitrogen feature is overrun by the time the concentration reaches about 1.5 mole percent. The central wavelength of the feature in liquid nitrogen from the spectra of R. N. Clark (USGS) et al. is 2.152 ± 0.002 μm, in precise agreement with the new Triton data.

Several points emerge from an examination of the spectra in Figure 18. First, there is an overall agreement in the shape and strength of the methane band at 2.3 μm. Three specific features in the methane spectrum, the minima at 2.22, 2.31, and 2.36 μm, are found in the Triton data, though not in the same relative strengths. Second, the central wavelength of the pure liquid nitrogen band coincides exactly with an absorption feature in the Triton spectrum at 2.150 μm. In addition, a marginal feature in the Triton spectrum appears at 2.05 μm.
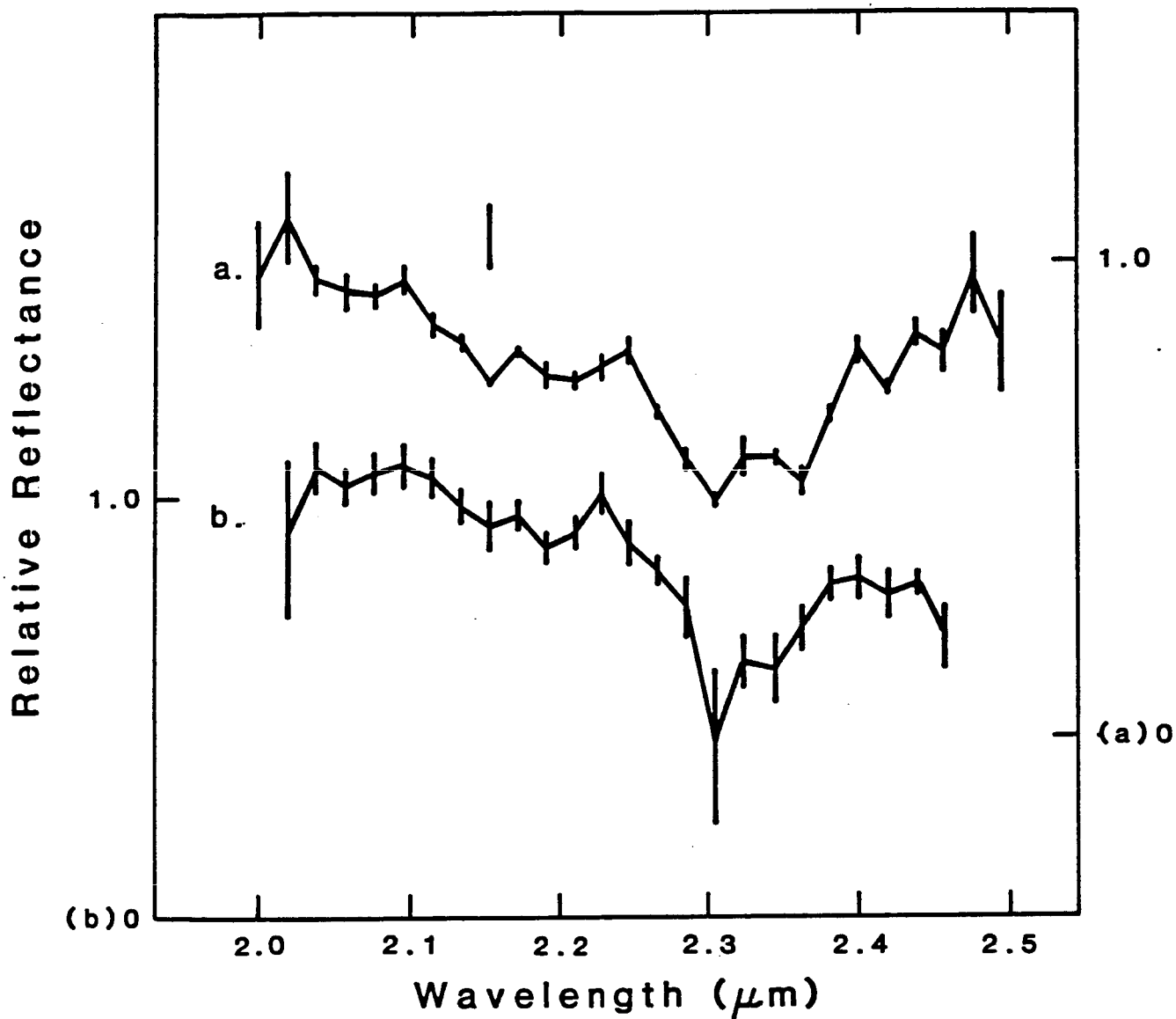
Figure 17.   Spectra of Triton. (a) is the grand average of five nights data taken 17-21 May 1986, and (b) is the average of data from 27 August 1986. The vertical line shows the position of the absorption attributed to molecular nitrogen.

33
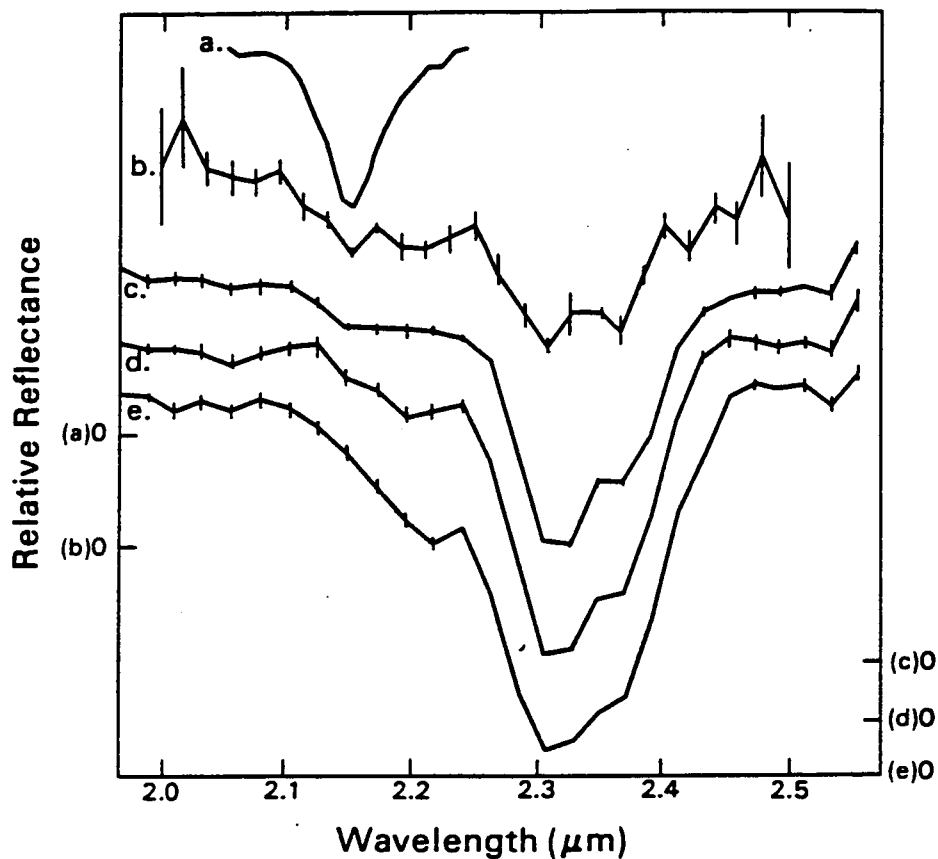
Figure 18. Spectra of Triton (b) and laboratory samples. (a) is a transmission spectrum of a 40-cm column of liquid nitrogen. (c,d,e) are transmission spectra of a 39-cm column of liquid nitrogen with various amounts of methane dissolved in it. The concentrations of methane in the liquid nitrogen for each of the three spectra are (a) 4.6 g/l, (b) 9.3 g/l, and (c) 18.6 g/l. For concentrations greater than about 10 g/l, the methane absorption obscures the liquid nitrogen band.

It is also useful to compare the new Triton data with spectra of gaseous methane, as was done by Cruikshank and Apt (1984). Because there are no adequate laboratory spectra for methane gas at the low temperature and pressure pertinent to Triton, we are obliged to use synthetic spectra computed with the best available band models and absorption coefficients. In Figure 19 we show the Triton data in comparison with a series of synthetic spectra computed by Dr. Jerome Apt and kindly made available for this purpose (for details of the band models see Cruikshank and Apt, 1984). Not only is the 2.3-µm band in the synthetic spectrum much wider for a given central depth than is the band on Triton, but the details of the structure are very different. There is no single example in the family of synthetic spectra shown that provides a satisfactory match to Triton.

Synthetic spectra of gaseous methane are strongly model dependent, as described by Apt et al. (1981). As in the case of the synthetic spectrum used by Cruikshank and Apt (1984) in their Figure 3, the spectra in Figure 19 of this paper were calculated with a low-temperature self-broadening coefficient of 0.355 cm^{-1} atm^{-1}. The gas abundances and pressures are those given in the figure caption; the temperature is T = 55 K.

Apt et al. (1981) computed the curve of growth for the absorption band at 2.3 µm under a variety of assumed model conditions. At values of less than about 100 cm^{-1} the equivalent width (EW) of the band is not strongly dependent upon the model (mean line spacing and broadening coefficient) nor upon the temperature. We have measured the equivalent width of the methane band in our Triton spectrum between 2.179 and 2.387 µm (corresponding to the interval used in the Apt et al. calculations) and find EW = 107 cm^{-1}.

Ideally, we would like to derive the abundance of gaseous methane on Triton from a band that is unsaturated and independent of the pressure and then use the stronger pressure-dependent 2.3-µm band to derive the surface partial pressure of methane by means of the Apt et al. (1981) curve of growth. The 0.89-µm methane band is the weakest feature that has thus far been detected in the Triton spectrum. Johnson et al. (1981) did not find this band at all when they observed at an orbital phase angle of 290°, nor did Combes et al. (1981) find it at phase angle 116°. Apt et al. (1983) detected the band weakly at phase angle 352°, thus adding to the evidence that the strength of the methane bands is dependent upon the viewing aspect, as has been discussed by Cruikshank and Apt (1984). The apparent spatial variability of the 0.89-µm band, plus the fact that methane ice seen in diffuse reflectance also shows an absorption band at the same wavelength, makes it clear that the gas abundance cannot be derived from observations of this band in the spectrum of Triton at spectral resolutions presently achievable.

We note that methane ice does absorb at the same wavelengths as the 0.89-and 2.3-µm gas bands, as can be seen in the reflectance spectrum published by Fink and Sill (1982) and in unpublished but frequently referenced
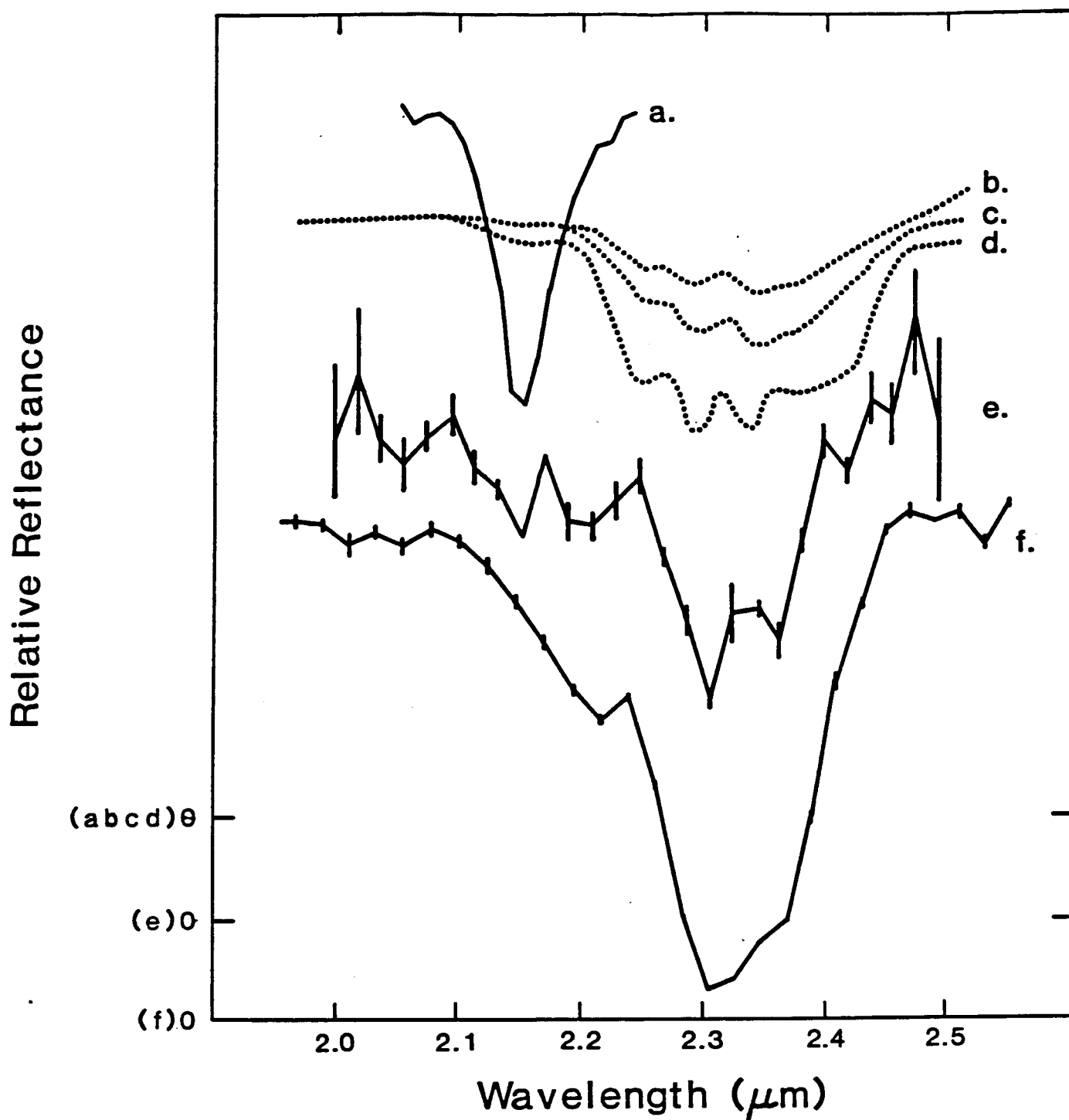
Figure 19

Spectra of Triton (e) and methane in various forms. (a) is a transmission spectrum of a 40-cm column of liquid nitrogen. (b,c,d) are synthetic spectra of methane gas computed by J. Apt for gas densities (at P = 1 mb, T = 55K) of (b) 15 m-am, (c) 50 m-am, and (d) 150 m-am. (f) is a transmission spectrum of 18.6 g/l methane dissolved in liquid nitrogen (39-cm column).

spectra by H. H. Kieffer. The strengths of the methane ice bands are strongly dependent upon the nature of the reflecting surface, as is the case with water ice (Clark, 1981). Very fine-grained frost yields the weakest absorption bands, while large crystals or a solid block of transparent or translucent ice results in very strong bands.

It thus appears that nongaseous methane on Triton makes a major contribution to the absorption spectrum and that we cannot derive the methane gas column abundance on the basis of the existing data. The most straightforward way by which to estimate the column abundance and partial surface pressure of methane is to use the equilibrium vapor pressure. The problem with this method is that the surface temperature of Triton is unknown because we remain ignorant of its albedo. In addition, the variation of temperature from the subsolar point to the dark hemisphere and to the polar regions, including the pole presently in long-term darkness, will have a profound effect on the local methane gas abundance because of the extremely strong dependence of vapor pressure upon temperature.

In Figure 20 we compare our Triton spectrum with reflectance spectra of methane ice from Fink and Sill (1982) and Kieffer (unpublished); the Fink and Sill data were taken at higher resolution than the others, but with a sample that gave overall less absorption strength. Several features in the Triton spectrum align well with those in the ice spectra, but the Triton band at 2.15 μm is not matched by any band in the laboratory data for methane.

While the details of the spectra match, the Triton spectrum has much less overall absorption in the 2.3-μm band than does either of the ice samples. It is, in fact, exceedingly difficult to prepare a laboratory sample of methane ice that will have a weak absorption spectrum, even if the sample is diluted with some neutral substance, such as charcoal. An additional laboratory problem is the strong tendency of methane frost samples to evolve rapidly to a solid sheet or glaze of ice. The absorption spectra of frosts of various kinds is strongly dependent upon grain size, as Clark (1981) has demonstrated and quantified for laboratory samples of water frost. The infrared bands are weakest for exceedingly fine grain sizes (on the order of 10 μm), and as the grain size increases the bands gain in intensity. In another paper, Clark et al. (1983) showed that the rate of metamorphism of grain size from small grains to large and then to a solid ice sheet is strongly dependent upon the volatility of the material. This metamorphism occurs because molecules preferentially evaporate from crystal edges and redeposit on crystal faces, thus causing the crystals to grow in size. Methane is enormously more volatile than water (higher vapor pressure), and at a given temperature the grain growth rate of methane is very much greater than than water (Clark et al., 1983). Clark et al. showed, for example, that on Triton or Pluto arbitrarily small methane frost grains would grow to 10 mm in 100,000 years at the assumed temperature of 50 K and would grow even faster at slightly higher temperatures.
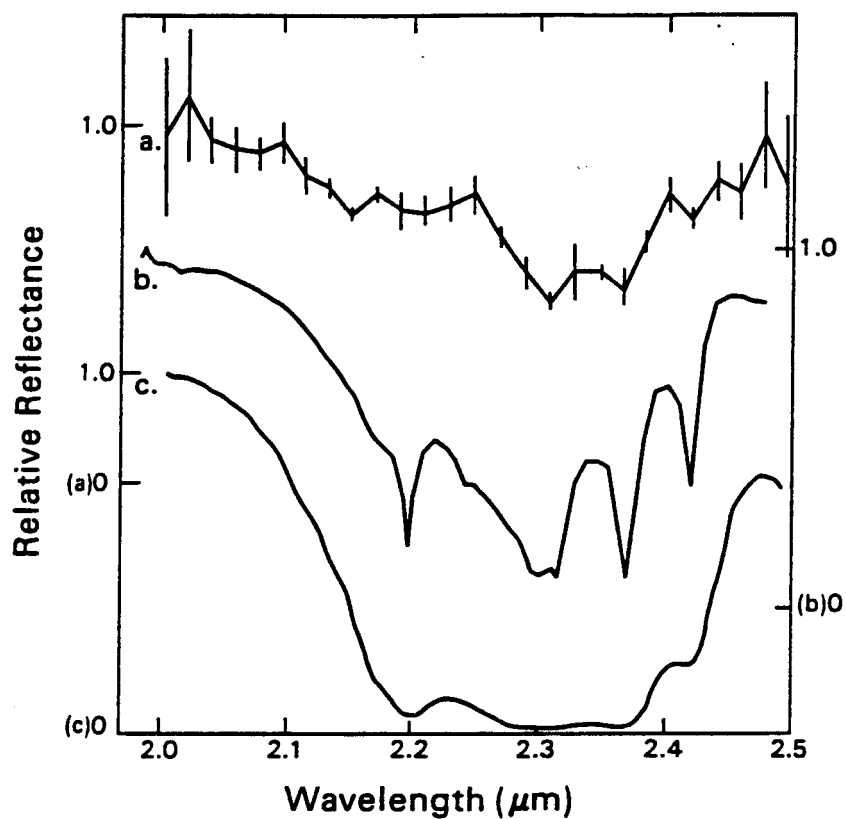
Figure 20

The spectrum of Triton (a) compared with two reflectance spectra of methane ice/frost. (b) is the spectrum of methane frost from Fink and Sill at 60K; (c) is a Kieffer spectrum of solid methane (unpublished).

In this context we note that Triton has a complex and extreme seasonal cycle resulting from the rapid precession of its orbital plane around Neptune's pole (P = 637 ± 40 years) and Neptune's sidereal period of 165 years. The subsolar latitude on Triton reaches 52° at some times, with large parts of the polar regions in long-term darkness (Harris, 1984; Trafton, 1984). Superimposed upon the seasonal cycle is Triton's diurnal cycle of 5.877 days. The combined effect of the diurnal and seasonal cycles and the alternating dark poles virtually ensures the mass migration of volatiles on Triton. It is not entirely unreasonable that the frequent condensation and sublimation of methane on a solid surface could produce a continuous supply of very fine frost grains consistent with the character of the 2.3-μm absorption band. The seasonal effects on the postulated nitrogen are difficult to estimate, since we are not yet confident of the physical state in which the nitrogen would be found (Lunine and Stevenson, 1985). Nitrogen is even more volatile than methane, however, and on a body where the temperature at a given location varies widely through the temperature range critical to the state of the material on a diurnal and seasonal basis, interesting effects might be expected.

We demonstrated above and in Figure 18 that the strength of the 2.3-μm methane band as seen in 1986 is approximated by a very small quantity of methane dissolved in liquid nitrogen. The spectral behavior of a liquid is a much closer approximation to that of a solid than to that of a gas because while some of the molecules are moving freely through the liquid, others are momentarily caged by their neighbors and are vibrating in the cages. The spectrum thus shows some of the characteristics of the molecules vibrating in a solid structure as opposed to the behavior in a gas (Castellan, 1983, p. 91).

There is a distinct qualitative difference in the appearance of the 2.3-μm band in the laboratory samples of liquid (Fig. 18) and ice (Fig. 19). For a given central depth of absorption (at 2.30 μm, for example), the width of the main core of the absorption band is much greater in the ice than in the liquid. In the limited set of laboratory data we present here, the Triton spectrum in the region 2.25-2.45 μm certainly resembles the liquid mixtures more than the ice samples.

Reference to Figure 17 suggests that the strong feature seen in earlier low-resolution spectra of Triton at 2.15 μm consists in part of the 2.20-μm component of the methane band plus an additional narrower feature centered at 2.15 μm.

This feature is not seen in the methane spectra from the laboratory, and because its central wavelength is the same as that for the first overtone of the density-induced nitrogen spectrum, we feel that the tentative identification by Cruikshank et al. (1984) as nitrogen is strengthened by the new data. No alternatives to this identification have been proposed, to our knowledge, but this alone does not make the nitrogen identification unique.

Cruikshank et al. (1984) showed that if there is sufficient nitrogen to show this band on Triton, it must occur in a condensed state, and they sug-

gested that liquid was more likely to produce the observed spectrum than would be nitrogen ice. They proposed a model of the Triton surface in which liquid nitrogen seas and expanses of solid methane occurred. Lunine and Stevenson (1985) concluded from the CH_4-N_2 phase diagram that a more likely configuration is for methane and nitrogen both to occur as solids in either a microscopic mixture or as a disequilibrium assemblage with a nonuniform distribution of the two components. The laboratory work on methane-nitrogen mixtures (Piscitelli et al., 1987) demonstrates the difficulty imposed by the very high solubility of methane in nitrogen. If liquid nitrogen and solid methane were both present on Triton, the nitrogen would probably be saturated or nearly saturated with methane. The spectrum is not consistent with any more than a minute quantity of methane dissolved in the hypothetical nitrogen sea.

It remains to be seen if the Triton spectrum is consistent with a solid mixture of the type suggested by Lunine and Stevenson (1985); laboratory data on solid nitrogen are difficult to obtain, and we know of no near-infrared spectra that relate directly to the problem at hand. We can say, however, that on the basis of the laboratory spectra in Piscitelli et al. (1987) and those given here, that the Triton spectrum in the 2.3-μm band is reasonably well matched feature-by-feature and in overall shape and strength by liquid mixtures of small quantities of methane dissolved in nitrogen.

Cruikshank and Apt (1984) noted the variability in strength of the methane band in Triton's spectrum throughout the range 0.8-2.5 μm, and found that the evidence was in favor of maximum absorption in the sector approximately defined by position angles 180° to 280°, corresponding roughly to the hemisphere of the satellite facing Neptune.

In preparing the coadded spectrum for May 1986 given in Figure 17, we have ignored the orbital variability of Triton's spectrum, because we could not see significant differences in the single-night data sets and because we wanted to maximize the signal precision of the entire data set. This procedure masks any orbital variability, of course, but in examining the individual nightly averages, we did not discern any strong tendencies toward variability of the methane band at a level above the intrinsic noise in each data set. This lack of variability was surprising because we were expecting to find the same trends reported in the earlier work.

We were further surprised by the overall weakness of the 2.3-μm methane band in the 1986 data in comparison to the spectra obtained in previous years and reported in our earlier papers (Cruikshank and Apt, 1984; Cruikshank et al., 1984). This startling difference is shown in Figure 21, in which the May 1986 grand average spectrum is compared with that of 2.4 June 1980. Though there may be some ambiguity as to the location of the continuum in each spectrum, the 1986 data have a maximum absorption depth of about 40% of the continuum, while those of 1980 show some 70% absorption (measured at the mini-
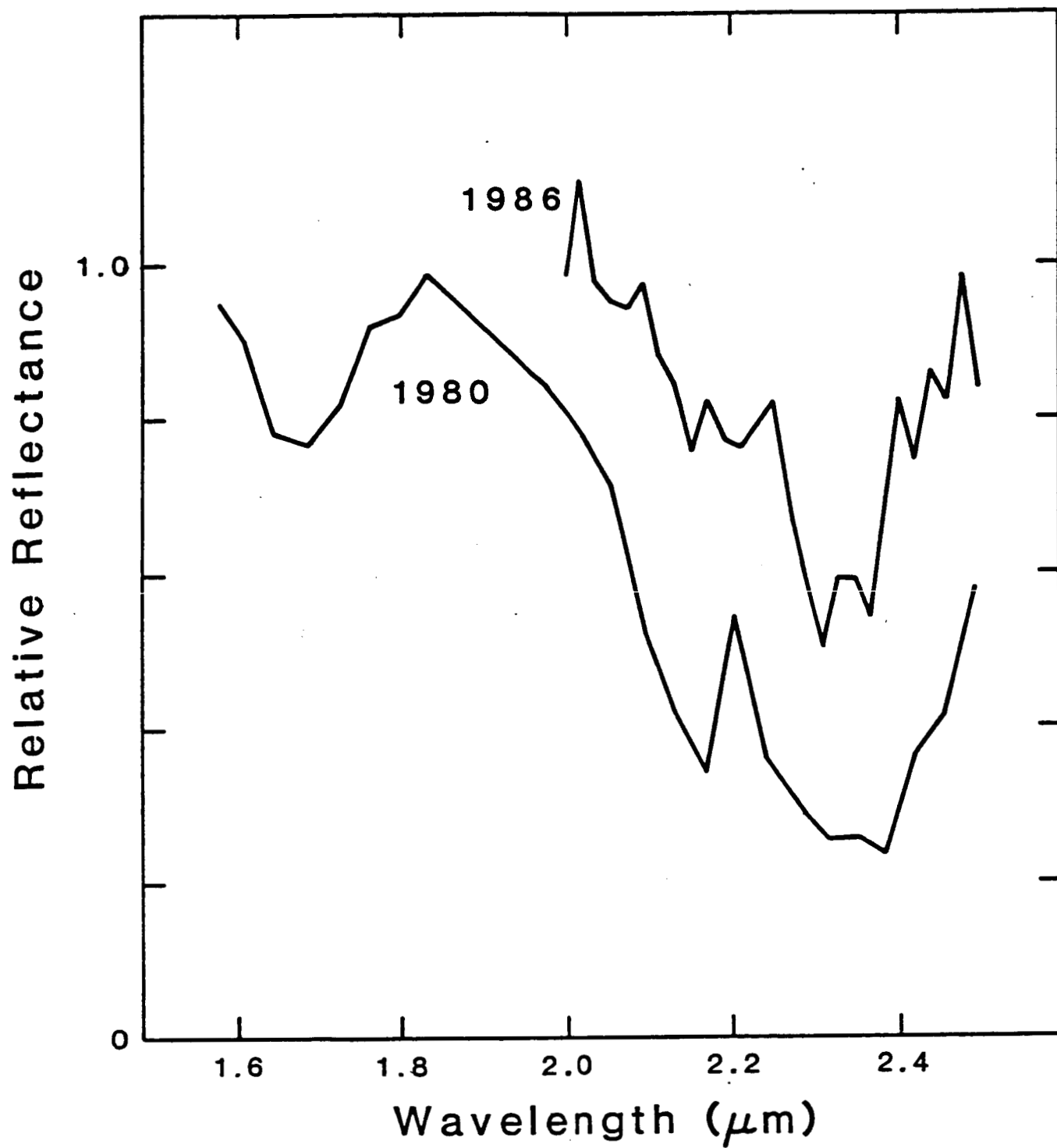
40

Figure 21

This figure compares portions of the Triton spectrum from May 1986, and from June 1980. The overall strength of the methane-nitrogen complex is much less in the 1986 data.

mum in each trace). The fact that the spectral resolution of the 1986 data is about 120, compared with 60 for the 1980 data cannot account for the difference seen in Figure 21. The band shape in 1986 is significantly narrower than in 1980, and the region around 2.1-2.2 μm is much weaker, while at higher resolution it should appear deeper.

Our new spectra are consistent with those obtained in April 1984 by Rieke et al. (1985) at similar resolution, but over a narrow wavelength range (2.1-2.25 μm). The Rieke data show a distinct but narrow band at 2.15 μm, coincident in wavelength and in strength with the band we see, and also an absorption at 2.2 μm, which we attribute to methane.

We cannot confidently attribute the difference in our spectra between 1980 and 1986 to any instrumental or geometric effect. We do note, however, that when we obtained spectra at several position angles in 1985 with the CGAS in an earlier stage of development, we found the absorption spectrum to be substantially weaker in the region 2.00-2.23 μm than we had anticipated (Tokunaga et al., 1985). In the regions covered, the spectra of both Rieke et al. (1985) and Tokunaga et al. (1985) should have shown a strong decrease in overall intensity toward the longer wavelengths if the spectrum was comparable to that in 1980, but such was not the case for either data set.

We are reluctant to conclude that Triton's spectrum changed markedly in the 1980s, but present evidence points in that direction. In a separate paper we will consider the complete data set available throughout the time period 1978-1986 in order to try to find a solution to this apparent enigma.

The new spectra obtained in 1986 confirm the presence of the strong methane band at 2.3 μm, but it appears generally weaker than earlier data at somewhat lower spectral resolution showed it six years before. Four specific features in the spectrum of methane, both as a frost and as a solute in liquid nitrogen, are seen in Triton's spectrum in the 2.3-μm region. In addition, all the data obtained by us in 1986 show a weak but persistent band at 2.15 μm coincident with the central wavelength of the 2-0 density-induced band of molecular nitrogen in the liquid state. We have compared the new Triton spectra to synthetic spectra of methane gas and find that a gaseous atmosphere alone cannot account for the relative strengths of the 0.89-μm band (Apt et al., 1983) and the band at 2.3 μm. The fact that methane ice shows strong absorptions coincident with the gas bands at both these wavelengths indicates that a pure gaseous spectrum cannot be observed on Triton.

If the methane bands on Triton are caused largely by frozen methane, then the material must be in the form of an exceedingly fine-grained frost in order to produce the very narrow 2.3-μm band we observe. Such fine grains may not be consistent with the extremely rapid metamorphism of fine grains to coarse grains and then to sheet ice predicted for methane from its known volatility (Clark et al., 1983) at the presumed temperature of Triton. Alternately, the methane bands may arise from very small quantities of methane dissolved in

liquid nitrogen; laboratory spectra by Piscitelli et al. (1987) show that the 2.3-μm methane band in this state is comparable in shape and strength to the band observed on Triton. We are still unable to evaluate from a spectroscopic point of view the viability of Lunine and Stevenson's (1985) proposal that methane and nitrogen would form a solid mixture of some kind on the surface of the satellite.

References

Apt, J., N. P. Carleton, and C. D. Mackay (1983). Methane on Triton and Pluto: New CCD spectra. Astrophys. J. **270**, 342-350.

Apt, J., J. V. Martonchik, and L. R. Brown (1981). Comparison of band model and integrated line-by-line synthetic for methane in the 2.3-μm region. J. Quant. Spectrosc. Radiat. Transfer **26**, 431-442.

Castellan, G. W. (1983). Physical Chemistry (3d ed.). Addison-Wesley, Reading, MA. 943 pp.

Clark, R. N. (1981). Water frost and ice: The near-infrared spectral reflectance 0.65-2.5 microns. J. Geophys. Res. **86**, 3087-3096.

Clark, R. N., F. P. Fanale, and A. P. Zent (1983). Frost grain size metamorphism: Implications for remote sensing of planetary surfaces. Icarus **56**, 233-245.

Combes, M., T. Encrenaz, and J. Lecacheux (1981). Upper limit of the gaseous CH_4 abundance on Triton. Icarus **47**, 139-141.

Cruikshank, D. P., and J. Apt (1984). Methane on Triton: Physical state and distribution. Icarus **58**, 306-311.

Cruikshank, D. P., R. H. Brown, and R. N. Clark (1984). Nitrogen on Triton. Icarus **58**, 293-305.

Fink, U., and G. T. Sill (1982). The infrared spectral properties of frozen volatiles. In Comets (L. Wilkening, Ed.), pp. 164-202. Univ. of Arizona Press, Tucson.

Harris, A. W. (1984). Physical properties of Neptune and Triton inferred from the orbit of Triton. In Uranus and Neptune (J. Bergstralh, Ed.), pp. 357-373. NASA Conference Publ. 2330.

Johnson, J. R., U. Fink, B. A. Smith, and H. J. Reitsema (1981). Spectrophotometry and upper limit of gaseous CH_4 for Triton. Icarus **46**, 288-291.

Lunine, J. E., and D. J. Stevenson (1985). Physical state of volatiles on the surface of Triton. Nature **317**, 238-240.

Piscitelli, J. R., D. P. Cruikshank, and J. F. Bell (1987). Laboratory studies of irradiated nitrogen-methane mixtures: Applications to Triton. Icarus (submitted).

Rieke, G. H., L. A. Lebofsky, and M. J. Lebofsky (1985). A search
for nitrogen on Triton. <u>Icarus</u> **64**, 153-155.

Tokunaga, A. T., R. G. Smith, R. H. Brown, D. P. Cruikshank, and R. N.
Clark (1985). The infrared spectrum of Triton at 2.0-2.25 μm.
<u>Bull. Am. Astron. Soc.</u> **17**, 698 (abstract).

Trafton, L. (1984). Large seasonal variations in Triton's atmosphere.
<u>Icarus</u> **58**, 312-324.

C8. Laboratory Studies Related to Triton

In our last report, we described laboratory observations of methane-
nitrogen mixtures made for comparison with the spectrum of Triton. The
results of that work have been written up in a paper by Piscitelli, Cruik-
shank, and Bell (Hawaii Institute of Geophysics, Planetary Geosciences Divi-
sion) that has been submitted to <u>Icarus</u>. The Triton studies noted in the
lengthy section immediately above have drawn considerably on the work by
Piscitelli et al., and we do not describe the results further here.

C9. Spectroscopy of Io

In a collaborative project with other investigators, notably R. Howell
(Wyoming), T. Geballe (UKIRT), and D. Nash (JPL), Cruikshank is completing the
analysis of a set of Io spectra in the region 3.5-4.2 μm. The new spectra
being studied have a resolution of about 500 and cover a range of Io longi-
tudes and times from 1983 through 1985. Several strong bands of SO_2 are
located in this wavelength region, and this substance is known to be a major
component of Io's surface; these same investigators have been working on prob-
lems of SO_2 on Io for a number of years. In the present work we have identi-
fied several new features attributed to SO_2, and have derived strengths of the
33S, 34S, and 18O isotopic bands; the isotopic ratios seem to be normal. The
data set has also been used to place new limits on the SO_2 gas abundance in
Io's (transient) atmosphere. The upper limit, subject to various caveats, is
0.1 cm-amagat, which would result in a very low surface pressure.

The new data set was compared in detail with laboratory specimens of sul-
fites and sulfates, both compounds that would be expected on Io, but neither
class of compounds can be identified with any certainty on Io. It is estab-
lished, though not very stringently, that the upper limits to the amount of
surface area covered by these compounds could be as high as 30%. Clearly, the
spectral evidence in this region covered by our data is not very restrictive
to the quantities of these compounds permitted below the detection level.

C10.   Volatiles on Europa

Cruikshank, in collaboration with Brown (JPL) and Tokunaga, has con-
tinued the spectrophotometric study of icy satellites; the data on Triton are
reported in section C7. We have also looked at Europa in the 2.3-μm region in
search of volatile signatures other than that of water ice. New data on the
leading and trailing hemispheres of Europa were obtained with the CGAS.
Spectra of the trailing side (CM 300°) obtained in 1985 show two weak absorp-
tions near 2.2 and 2.3 μm. Both of these features, as well as others, as seen
in spectra obtained by R. N. Clark (USGS) at a similar central meridian longi-
tude. However, with improved equipment and high-quality data, we cannot find
these absorptions in the Europa data taken in 1986. While we are skeptical of
any explanation that requires a major change in the spectral response charac-
teristics of the satellite between 1985 and 1986, there are no detectable
problems with the data sets that would suggest that the observed difference in
the spectra result from instrumental or other systematic effects.

Additional data will be obtained in 1987 to pursue the study of Europa in
the context of the other icy satellites being observed in this general program.

C11.   Uranus Ring Occultation Observations

Buie and Tholen are providing observations of stellar occultations by
Uranus seen from Hawaii as part of a collaborative effort with R. French at
MIT. Very high signal-to-noise data were obtained from an occultation
observed on 26 April 1986. All of the major rings were seen along with a
grazing atmospheric occultation. Figures 22a and 22b show an overview of the
ring events observed on Mauna Kea together with the model fits to the data.
In all cases the quality of the fit is remarkable and stresses the importance
of continued Earth-based monitoring of the Uranian ring system.

Most of the modeling and analyses are being done by French. The new data
have been added to the growing data base that constrains the orbit solutions
for the Uranian ring system. The latest work by French has identified a number
of resonances that are responsible for shaping and controlling the ring
system. This pushes the accuracy of the model to ±1 km in the semi-major
axes of the rings and ±0.01° in the direction of Uranus's pole, an accomplish-
ment that exceeds the capabilities of Voyager alone. In Figures 23a and 23b
we show a comparison of the stellar occultation of the ε and γ rings observed
at Mauna Kea in comparison to the Voyager X-band data.
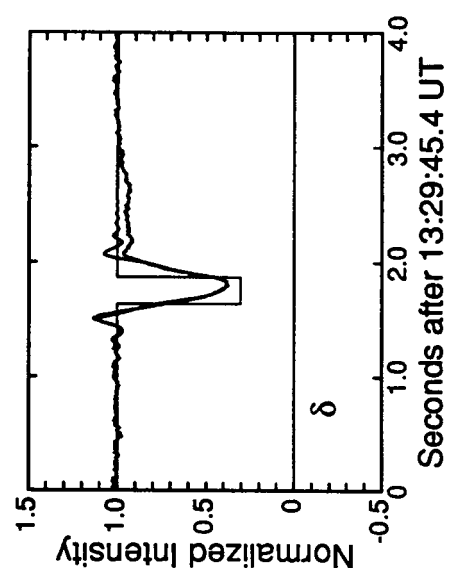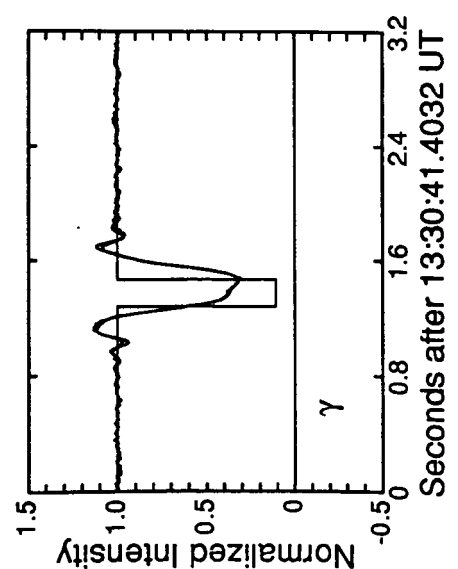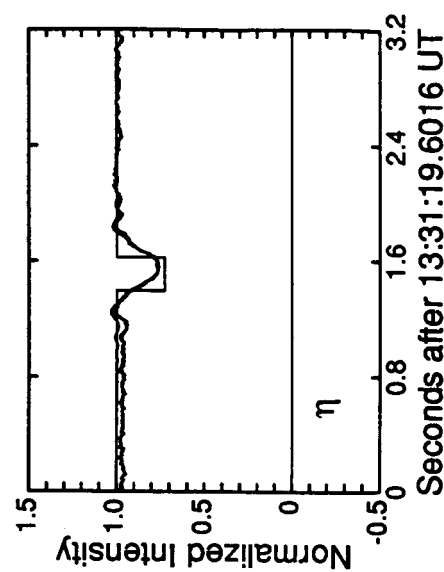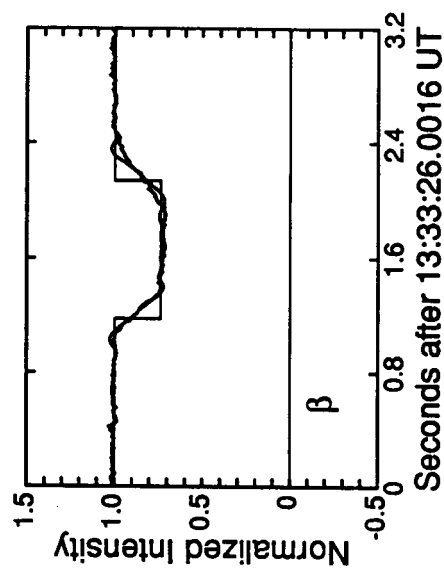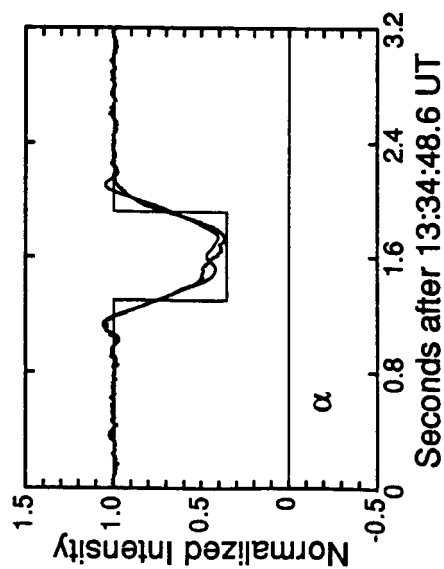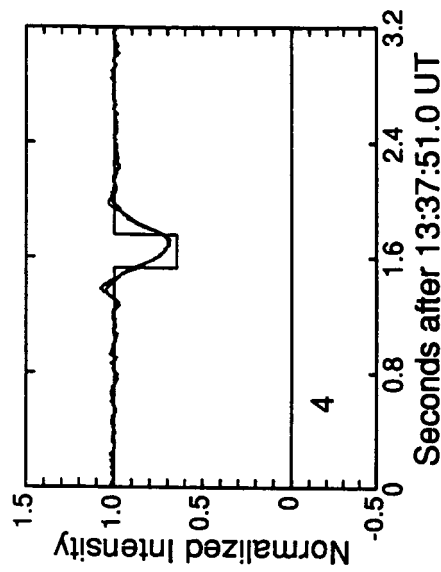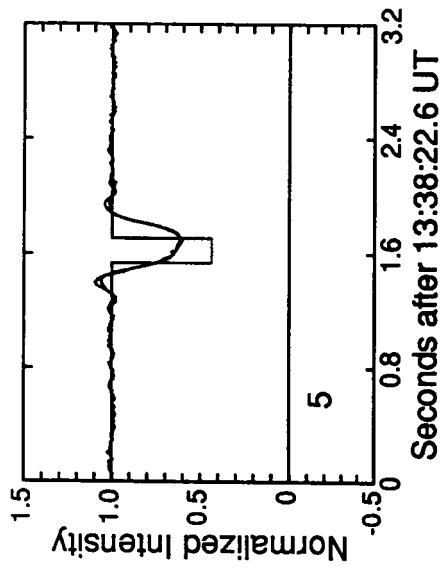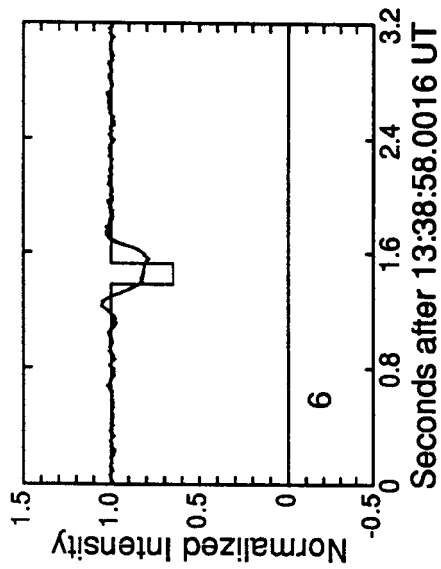
Figure 22a. Mauna Kea Observatory data on stellar occultation of 26 April 1986 by the rings of Uranus, with model fits (square wells).
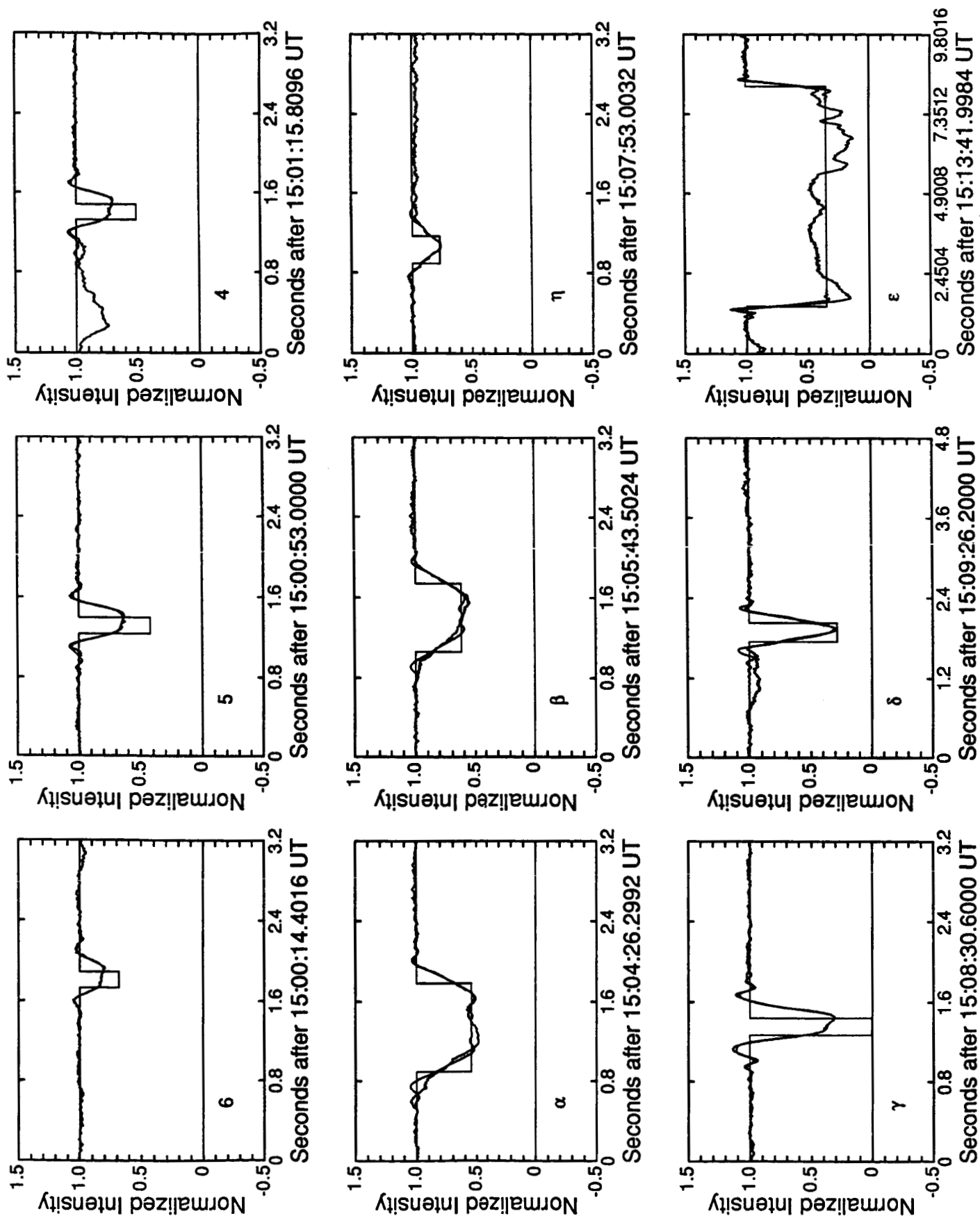
Figure 22b.   Mauna Kea Observatory data on stellar occultations of 26 April
1986 by the rings of Uranus, with model fits (square wells).

U28 MKO Epsilon Ring Egress
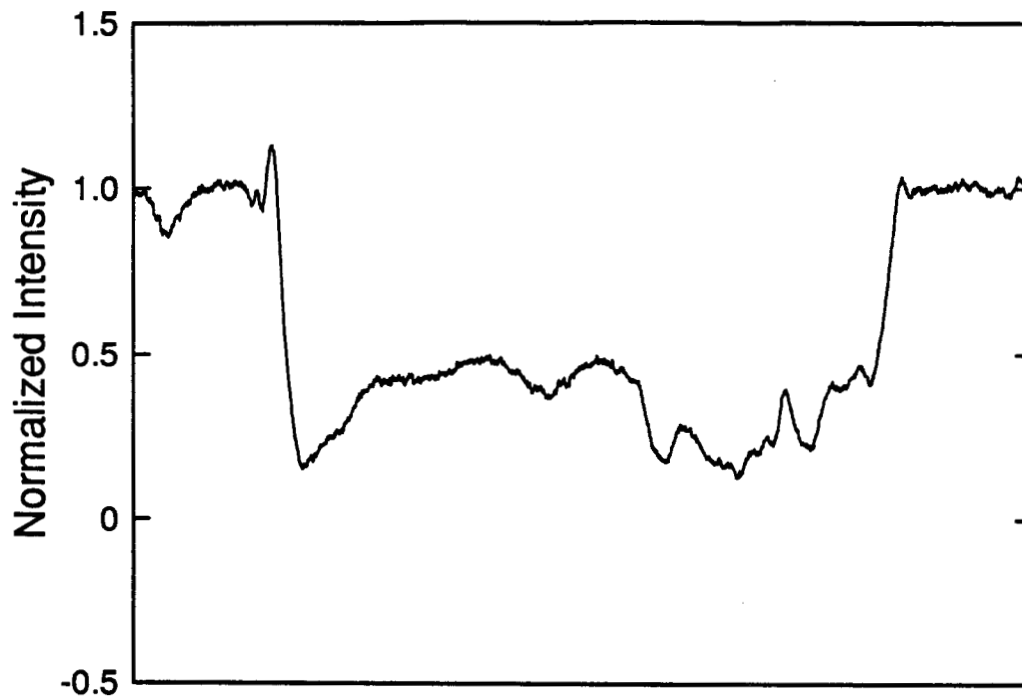
Voyager RSS X-Band Epsilon Ring Egress
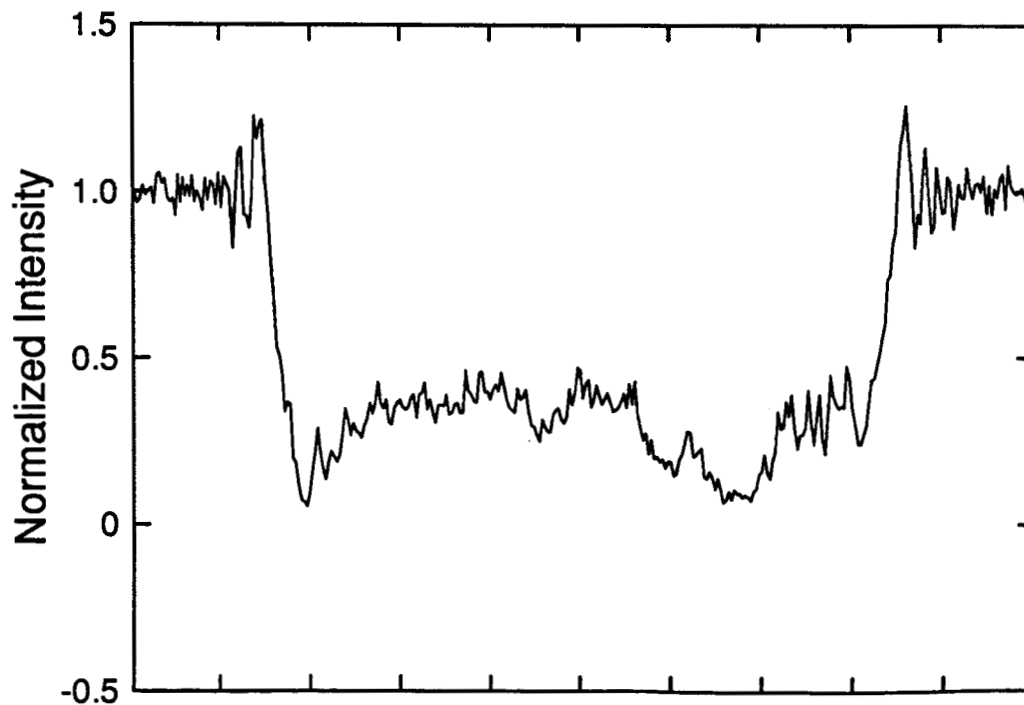
Figure 23a

Stellar occultation of the epsilon ring of Uranus (Mauna Kea)
in comparison with the Voyager 2 X-band occultation curve.

Voyager RSS X-Band Gamma Ring Egress

Seconds after 1:30:09.5922 UT

26 April 1986 IRTF Gamma Ring Egress

Seconds after 15:08:30.6 UT
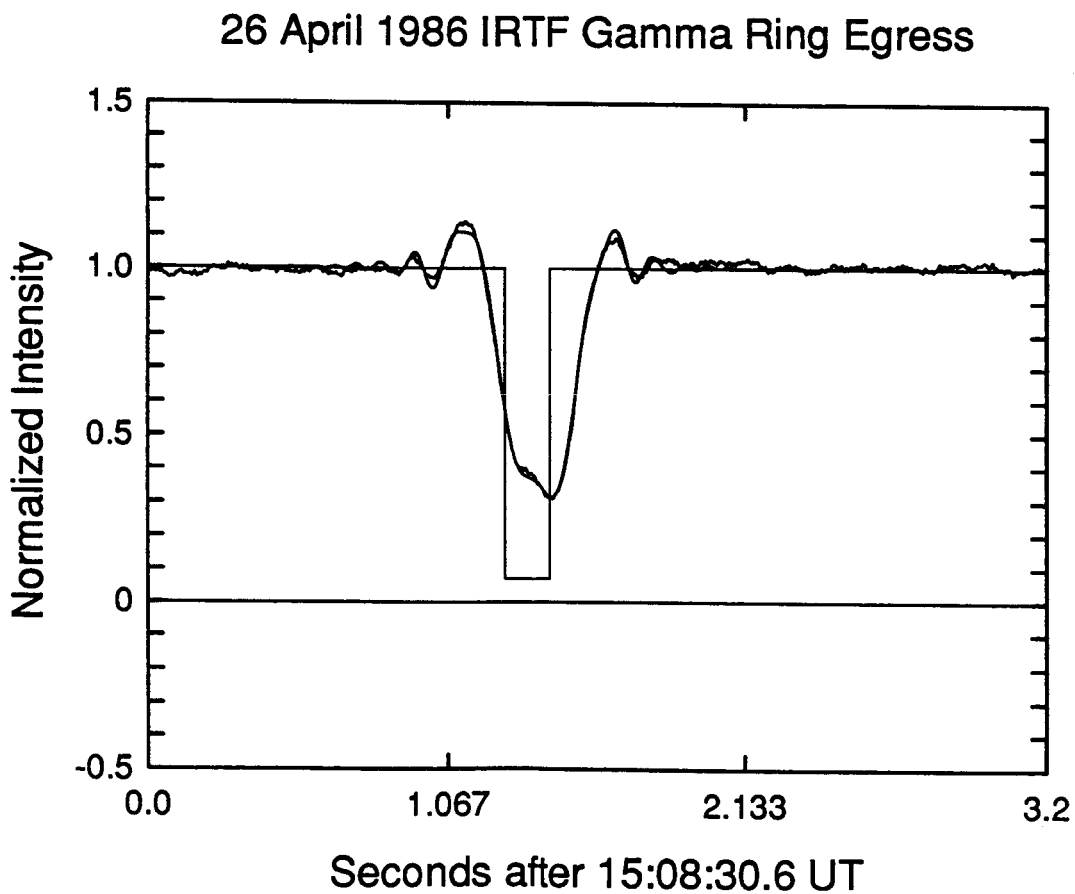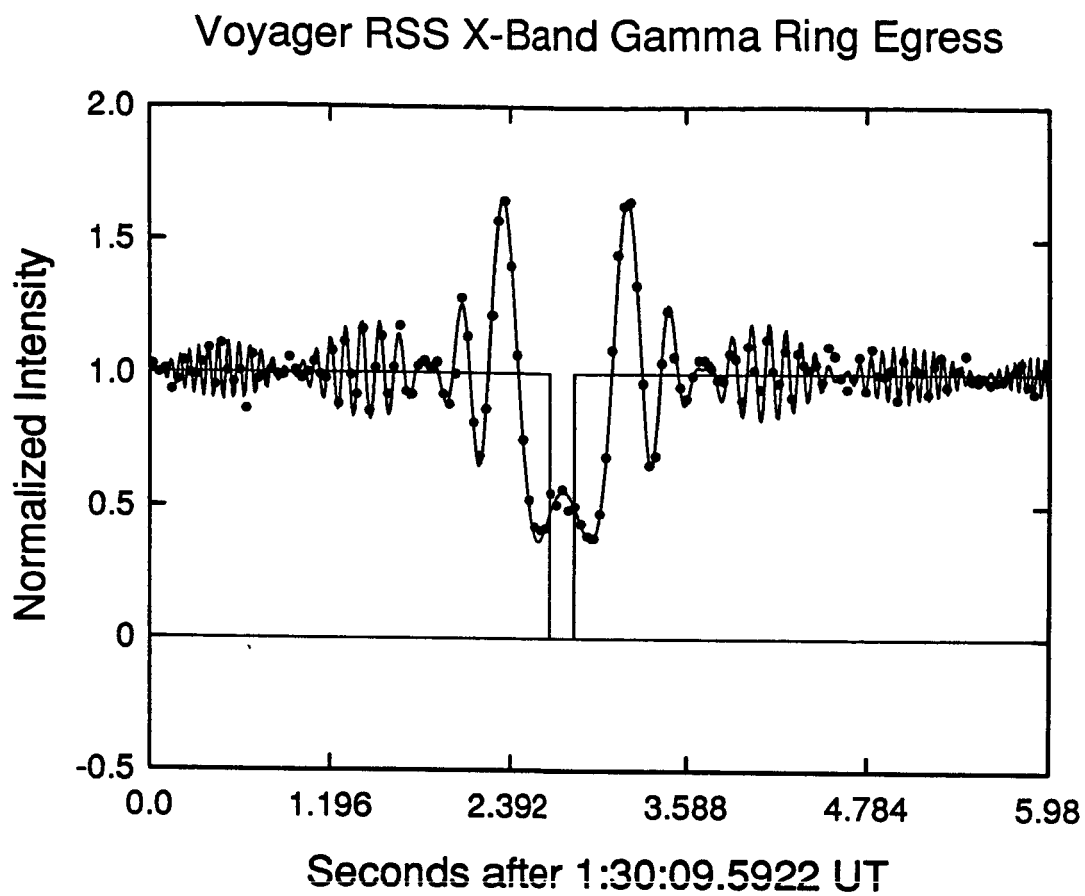
Figure 23b

Stellar occultation of the gamma ring of Uranus (Mauna Kea)
in comparison with the Voyager 2 X-band occultation curve.

49

D. ASTEROIDS

D1. Lightcurves of Trojan and Hilda Asteroids

Tholen and Hartmann resurrected a project to determine the rotational and shape characteristics of Trojan and Hilda asteroids. Because these asteroid populations are isolated from the main belt, one might expect them to have had a different collisional history. The goal of this project is to provide information on the collision evolution of these populations. Because the Trojan and Hilda asteroids are among the most distant asteroids, they are also among the faintest, thus requiring the 2.2-m telescope for these observations.

In 1986, this project was advanced on two fronts. First, data acquired in May 1984 by J. Goguen (formerly at IFA, now at JPL) Cruikshank, and W. K. Hartmann (PSI, Tucson) were reduced. Second, Tholen and Hartmann acquired new observations of asteroids (659) Nestor, (884) Priamus, (1172) Aeneas, (1345) Potomac, (1404) Ajax, (1868) Thersites, (2483) Guinevere, (3451) 1984 HA1, (3548) 1973 SO, and 1985 TQ, primarily in January, July, and December. Early results would seem to indicate that the average amplitude of a Trojan or Hilda asteroid lightcurve is higher than their main-belt counterparts, suggesting more elongated shapes, and that the average rotational period is longer. Some biases do exist in the data, however, and more statistics will be required to confirm these early conclusions. Two manuscripts describing the current state of the project are presently nearing completion.

Sample lightcurves are shown in Figures 24-26. The huge amplitude of the lightcurve for (2483) Guinevere was a surprise (Fig. 24). The asteroid is apparently as least as elongated as (624) Hektor. The rotational period is also longer than is typical of main-belt asteroids. The other two objects, (1172) Aeneas (Fig. 25) and (1345) Potomac (Fig. 26), also have longer periods and larger amplitudes than are typical of main-belt asteroids.

D2. Multicolor Photometry of Asteroids

Tholen continued efforts to obtain five-color photometry of outer-belt asteroids, planet-crossing asteroids, members of interesting dynamical families, and other objects whose eight-color classifications were ambiguous or unusual. The observations of the planet-crossing asteroids will be discussed in a section D3.

Color observations of Hilda asteroid (2483) Guinevere yielded a D-type reflectance spectrum, which is no surprise for that part of the asteroid belt, but during the course of the color observations, Guinevere brightened by 0.6 mag! As a result, the asteroid became one of the principal targets for light-curve photometry during the remainder of the observing run (see section D1).

Asteroids that were observed include (260) Huberta, (401) Ottilia, (1404) Ajax, (1565) Lemaitre, (1657) Roemera, (1868) Thersites, (2741) Valdivia, (3106) 1981 EE, and (3451) 1984 HA1.

2483 Guinevere   Period = 14ʰ.7
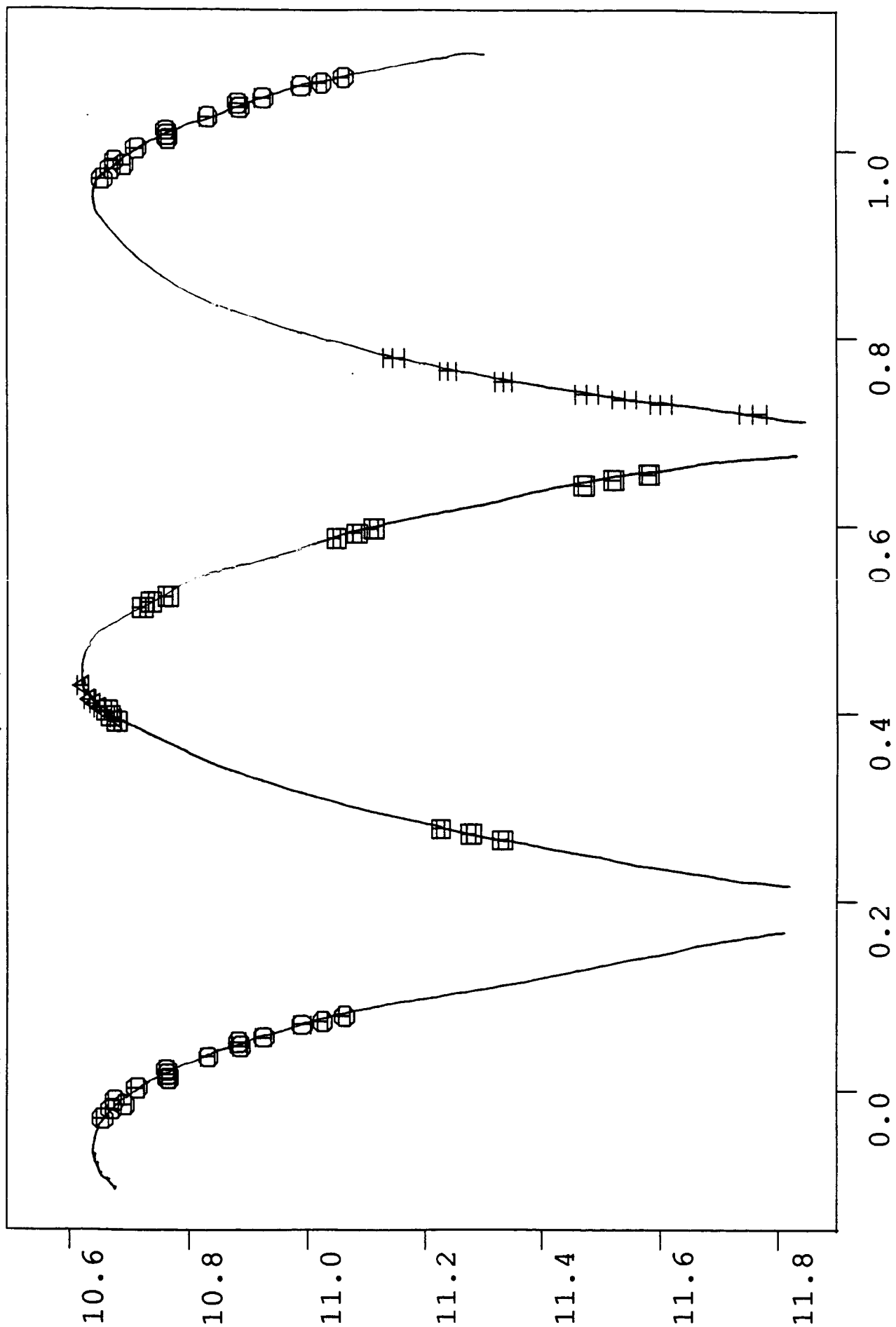
H mag v.
Rotational phase

Figure 24

51

Mag v.
Rotational phase

Figure 25

Period = 0.3650000 days

1172 Areas

o Jul 8
□ Jul 9
△ Jul 10

52

1345 Potomac
P = 11ʰ.398

Mag v.
Rotational phase

Figure 26

53
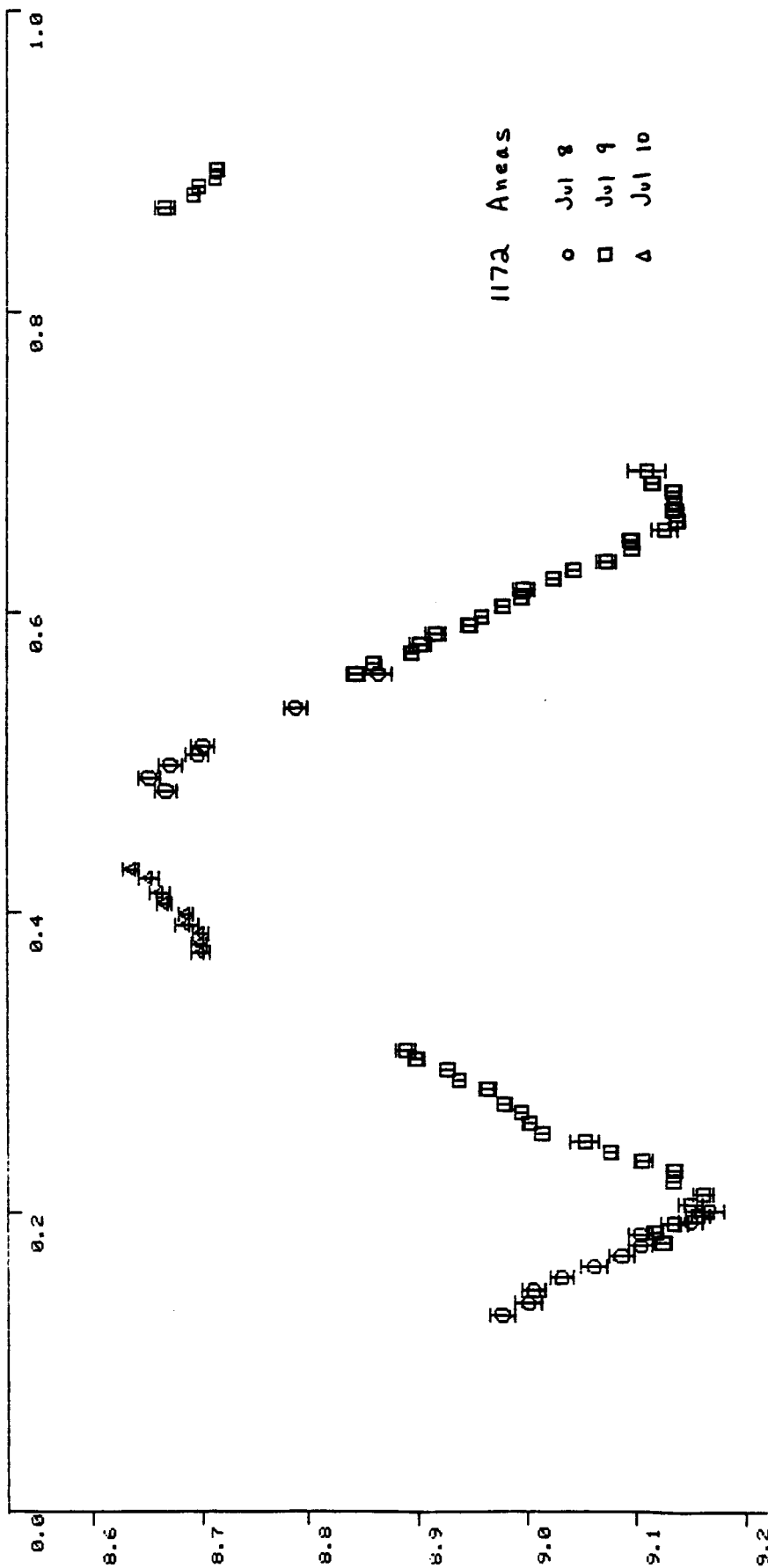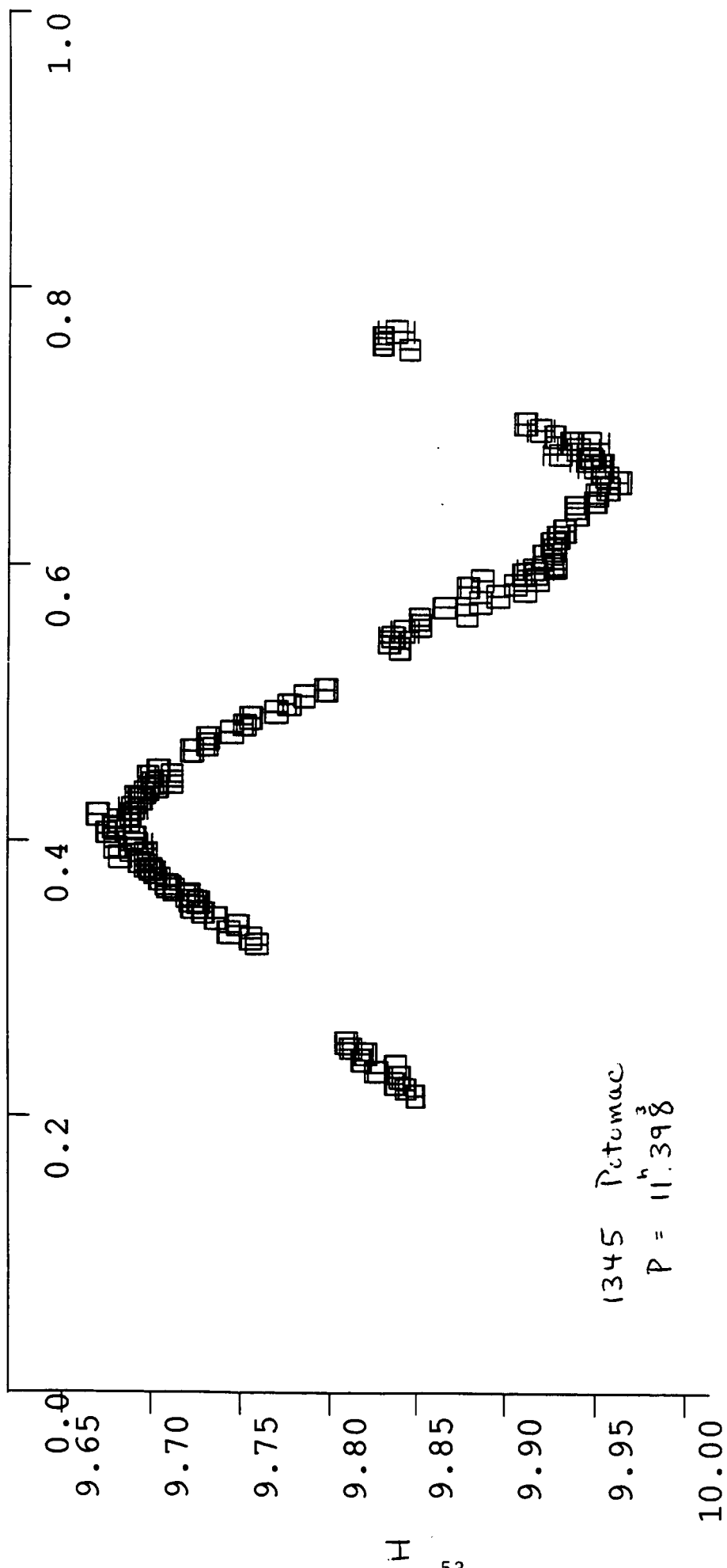
Tholen has continued to monitor the brightness of (2060) Chiron with the 2.2-m telescope to look for an outburst of the P/Schwassmann-Wachmann 1 variety. Such an outburst would explain the discrepant visual and infrared photometry obtained in previous years. Tantalizing data on this 19th mag object were obtained in late December 1986. On one night, Chiron was approximately 0.5 mag brighter than predicted, but the proximity of a field star has rendered the data questionable. The following night, Chiron was about 0.3 mag brighter than predicted, which is about a 3-σ fluctuation from the mean of all previous observations. It seems plausible that the tail end of an outburst was observed, but the data are not quite sufficient to confirm such an event.

D3. Planet-crossing Asteroids

Eleven planet-crossing asteroids were successfully observed at visual wavelengths by Tholen in 1986, all but one with the 2.2-m telescope. The objects include (1566) Icarus, (2074) Shoemaker, (3103) 1982 BB, (3199) Nefertiti, (3361) 1982 HR, (3551) 1983 RD, (3554) 1986 EB, 1984 AB, 1985 PA, 1986 DA, and 1986 JK. Infrared CVF observations of (3551) 1983 RD were also obtained by Cruikshank, Tholen, and Hartmann with the IRTF.

In 1986, (3551) 1983 RD made its first favorable apparition since discovery. During the discovery apparition three years ago, Tholen's five-color photometry yielded a reflectance spectrum that was identical to that of (4) Vesta, which at that time was the only asteroid known to have a reflectance spectrum indicative of essentially olivine-free pyroxene. New five-color photometry obtained in 1986 has confirmed the 1983 findings. Vesta has long been considered the eucrite meteorite parent body, but the delivery of eucrites from Vesta to Earth has remained a problem, one that might be solved if an Earth-approaching asteroid was found to be similar to Vesta. The discovery of 1983 RD's Vesta-like spectrum likely provided the missing link. The five-color photometry obtained in 1983 extended only to 9000 Å, however, and the telltale pyroxene and olivine absorption features extend out to 2 μm. To confirm the identification of 1983 RD as being Vesta-like, infrared observations were required. In 1986, 1983 RD became barely bright enough to observe with the CVF at the IRTF. Preliminary analysis of the new data clearly shows a strong pyroxene absorption feature, but a more careful reduction needs to be performed to make a more detailed comparison with the well-established infrared spectrum of Vesta.

Another exciting discovery was the A-type reflectance spectrum of (2074) Shoemaker. A-type asteroids are typified by a very strong olivine absorption feature in the near-infrared. Shoemaker is only the sixth known asteroid to have an A-type spectrum. Also, it lies near the $\nu5$ resonance with no known near neighbors. This object's orbit has probably evolved from the main belt. The widely dispersed A-type asteroids have unfortunately made it difficult to specify the likely source region for Shoemaker.

(3103) 1982 BB was found to have a very large amplitude lightcurve, making it one of the more elongated Earth-approaching asteroids. Additional observations are planned for early 1987 on the outbound leg of this object's orbit. Eventually, these data will be combined with similar data obtained by W. Wisniewski (Arizona) to provide more complete coverage of the lightcurve and a more precise determination of the rotational period.

Photometry of (1866) Sisyphus obtained in December 1985 was reduced in 1986. The lightcurve is of small amplitude (0.1 mag) and very short period (2.4 hr), making it one of the fastest rotating bodies in the solar system. The surprise is the incredible amount of structure in the lightcurve. Figure 27 shows the data acquired on 28 December 1985 UT with the 2.2-m telescope. The spike was seen twice, 2.4 hr apart, and is therefore confirmed. Whether the spike is due to a large protrusion coming into view on the limb of the asteroid or due to a glint from a large relatively flat area is not known yet. It is important to note that without the light gathering power of the 2.2-m telescope, the photometric resolution achieved would have not been possible; that is, the spike would have gone unnoticed, as well as much of the structure. This information may be crucial to the proper interpretation of some curious radar echoes obtained by S. Ostro (JPL).

D4. Near-Infrared Spectrophotometry of Asteroids

Cruikshank and Tholen, in collaboration with Hartmann continued their work on the near-infrared spectrophotometry of selected asteroids, including A types (olivine-rich) and their relationship to the S-type asteroids. Simultaneously, they obtained additional data on the spectrophotometric signatures from 0.8- to 2.5-μm of various P, C, and D types. An observing run in May 1986 was lost to clouds, but a run on the IRTF in October 1986 was very successful. During that run, excellent data were obtained for the following objects in the A-S and P, C, D projects: 1983-RD, 443 Photographica, 194 Prokne, 119 Althea, 4 Vesta, 352 Gisela, 27 Euterpe, 9 Metis, 17 Thetis, 12 Victoria, 2074 Shoemaker, 67 Asia, 1129 Atami, 14 Irene, and 87 Sylvia.

We are now working on the reduction of the data and will not be obtaining new observations until this project can be completed. We believe that we now have enough VJHK photometry and 0.8- to 2.5-μm spectrophotometry to complete our project on the A-to-S transition and on the basic characteristics of the C, P, and D types.

D5. Organic Molecules on Asteroid 130 Elektra

The carbonaceous chondritic meteorites are known to contain organic matter. Aliphatic and aromatic polymers constitute about 6% of the mass of

1866 Sisyphus   Period = 2ʰ.40
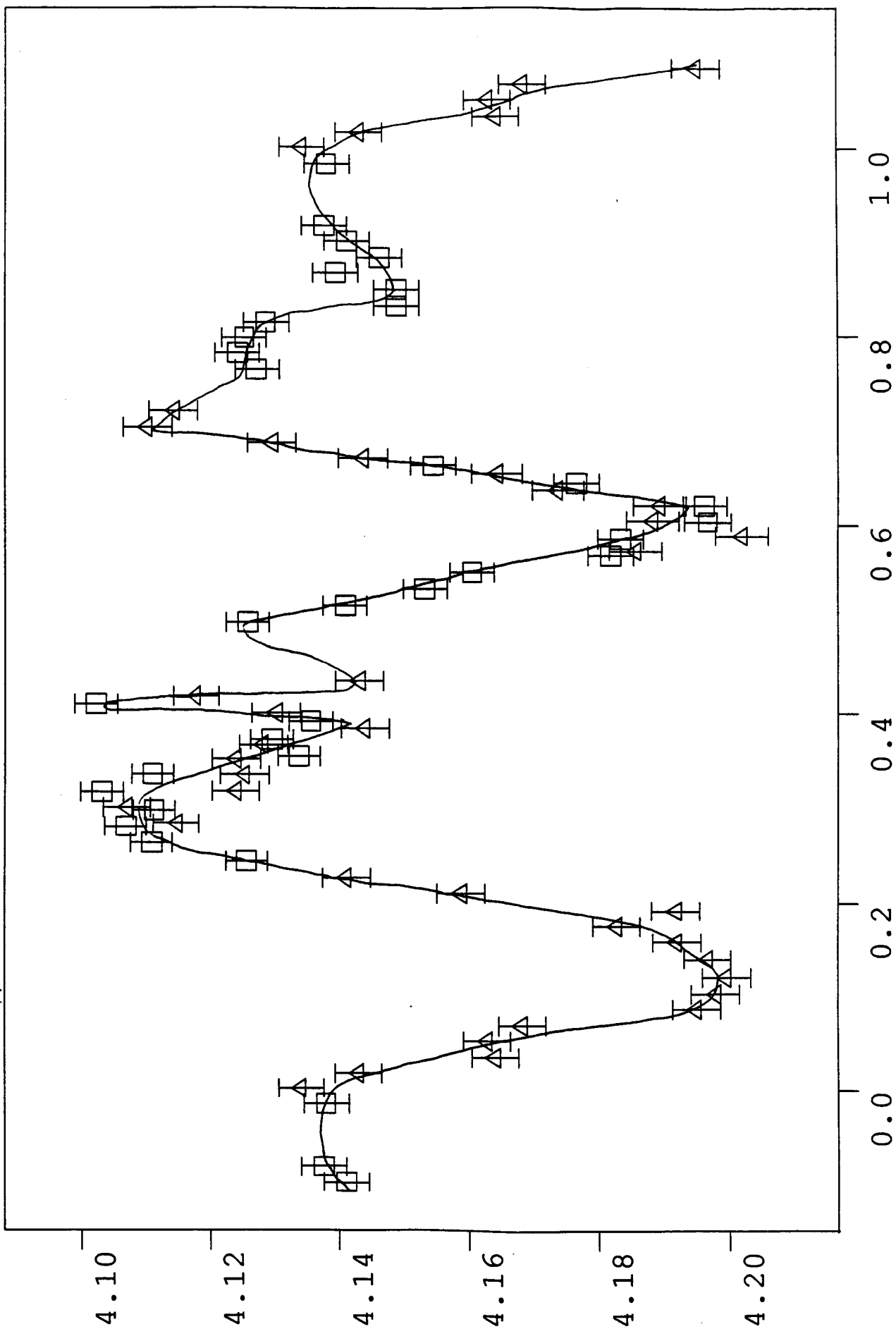
ΔV mag v.
Rotational phase

Figure 27

56

the volatile-rich CI chondrites, which are among the most primitive samples of matter in the solar system.

While the parent bodies of the carbonaceous chondritic meteorites are presumed to exist among the outer asteroids, the evidence is based on their mutual low albedos and, in some cases, reddish colors. L. A. Lebofsky et al. showed in 1981 that some, but not all, low-albedo C-type asteroids have a broad absorption in their spectra at 3 μm that is attributable to bound water in the mineral lattices. This finding is consistent with the bound water in the CI and CM carbonaceous chondrites. The strength of the ultraviolet absorption, attributed to charge-transfer transitions in iron and titanium, is related to the amount of water represented by the 3-μm absorption band, as has been shown by M. A. Feierberg et al. in 1985.

In the most primitive carbonaceous chondrites, such as Murchison (CM), a complex of very shallow bands at 3.4 μm is superimposed upon the 3-μm water band seen in diffuse reflectance. These features are caused by the C-H stretching mode and are common to all organic matter, though the exact positions and band shapes vary from compound to compound. Other carbonaceous meteorites, notably the less primitive samples, such as Allende (CV), do not show the C-H band clearly, nor do they have significant bound water evident in their reflectance spectra.

Cruikshank, in collaboration with A. Tokunaga (IFA) and R. H. Brown (JPL) used the cooled-grating array spectrometer (CGAS) at the IRTF in August 1986 to obtain spectra of the "wet" C-type asteroid 130 Elektra in search of the 3.4-μm C-H bands. Figure 28 shows the asteroid spectrum in the region of the 3.4-μm band. In the upper panel the spectrum is shown as a simple ratio to a solar-type star. For comparison, the laboratory reflectance spectrum of the insoluble organic extract from the Murchison CM meteorite is shown. The complex of bands at 3.4 μm in the meteorite sample is due to organics in the extract. The lower panel of the figure shows the same two spectra but with the continua removed computationally. Such removal of the continua aids in assessing the similarity and coincidence of the absorption features in the spectra. The natural continuum slope in the asteroid spectrum results from a combination of the water absorption band, the thermal emission of the asteroid surface, and the slight differences in the color of the Sun and that of the reference star in this spectral region. In the case of the laboratory spectrum of Murchison extract, the continuum slope results from the strong bound water absorption band and the details of the comparison beam of the spectrometer.

We suggest that the main features of the C-H band in Murchison are repeated in the spectrum of 130 Elektra. The band is very weak; in concentrated organic material from the meteorite it amounts to only about 5% absorption depth. Though the band strength depends on particle size and packing, we would not expect it to be as strong on the asteroid as in the laboratory
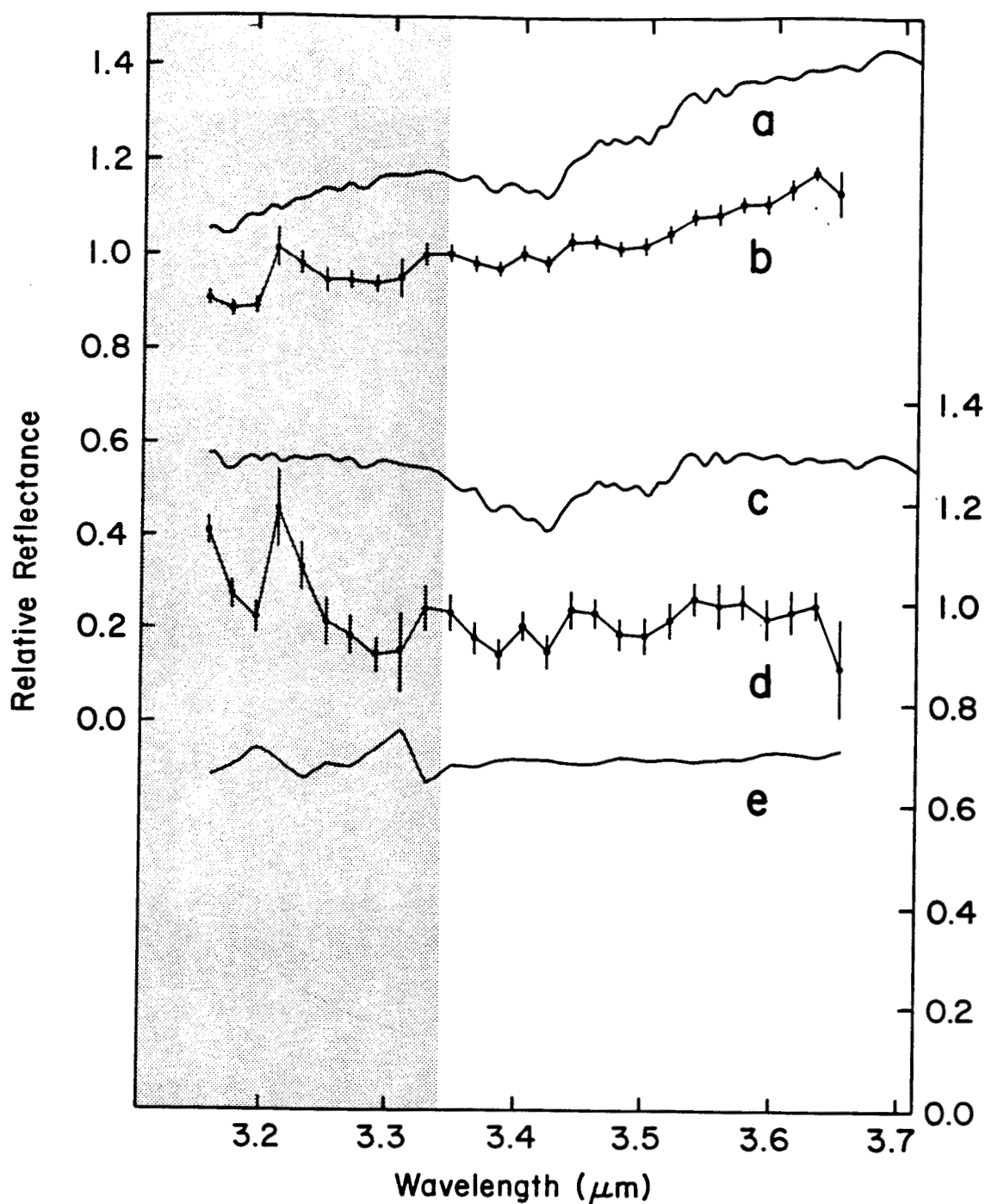
Figure 28

Reflectance spectra of asteroid 130 Elektra and an organic extract from the
Murchison carbonaceous chondrite. (a) is the spectrum of Murchison with two-
times vertical exaggeration to emphasize the weak features. (b) is the asteroid
spectrum (no exaggeration) with formal error bars shown. (c) is Murchison
with the continuum slope removed, and (d) is the Elektra spectrum similarly
flattened (and with two-times vertical exaggeration). (e) is the standard star
spectrum corrected for extinction. The portions of the spectra in the
hatched zone are unreliable because of telluric extinction which cannot be
fully corrected.

concentrate from the meteorite. The maximum absorption depth in the asteroid spectrum is about 4%.

The 3.4-μm band is diagnostic of the presence of hydrocarbons, but from this band alone it is not possible to determine just what molecules are involved. Murchison contains a vast array of hydrocarbons, any and all of which exhibit the C-H band we see on the asteroid. Also, the presence of the C-H band on an asteroid does not prove that all of the primitive carbonaceous chondrites originate from this or any other asteroid; comets are known to have this spectral feature, though it is normally seen in emission, as in the case of ground-based and spacecraft studies of Comet Halley in 1986.

We shall continue our studies of the 3.4-μm spectral region on asteroids, comets, and planetary satellites (particularly Iapetus), in an effort to elucidate further the connections among these objects and the meteorites in terrestrial collections.

D6. Modeling of Asteroid Rotational Lightcurves

Goguen and Research Assistant K. Uchida continued work that they had begun in the previous grant year on the modeling of asteroid rotational lightcurves using Goguen's photometric model for the surfaces of airless planetary bodies. They elected to model Trojan asteroid (624) Hektor because of its extreme lightcurve. Five small phase angle lightcurves were fit simultaneously with a general triaxial ellipsoid model. The input data span a period of 11 years and sample both small and large amplitudes. The model rotates counterclockwise about its shortest axis, and its surface has a lunarlike photometric function with normal reflectance of 0.022. The rotation period is 0.288335 days and the rotational pole direction is at ecliptic longitude of 314° and ecliptic latitude of +17°, in reasonable agreement with previous estimates. The semi-axes of the ellipsoid are A = 206 km, B = 93 km, and C = 78 km. The axial ratios of the model ellipsoid are close to those expected for Jacobi ellipsoids, a subset of triaxial ellipsoids that satisfies the conditions of hydrostatic equilibrium in a rapidly spinning body of uniform density. If (624) Hektor is assumed to be in hydrostatic equilibrium, the density implied by B/A, C/A, and the rotation period noted above is 1.0 g/cm^3. This model is stable with respect to binary fission, contrary to the conclusion reached by Weidenschilling in 1980 based on the maximum measured lightcurve amplitude alone.

Figure 29 shows the model fit (solid curve) to the five lightcurves studied. Note, also, that the phase is correctly fit, using the rotation period given above.

D7. Astrometry

Tholen continued a low-level effort to acquire astrometric positions of asteroids using the shaft encoders of both the IRTF and the 2.2-m telescope.
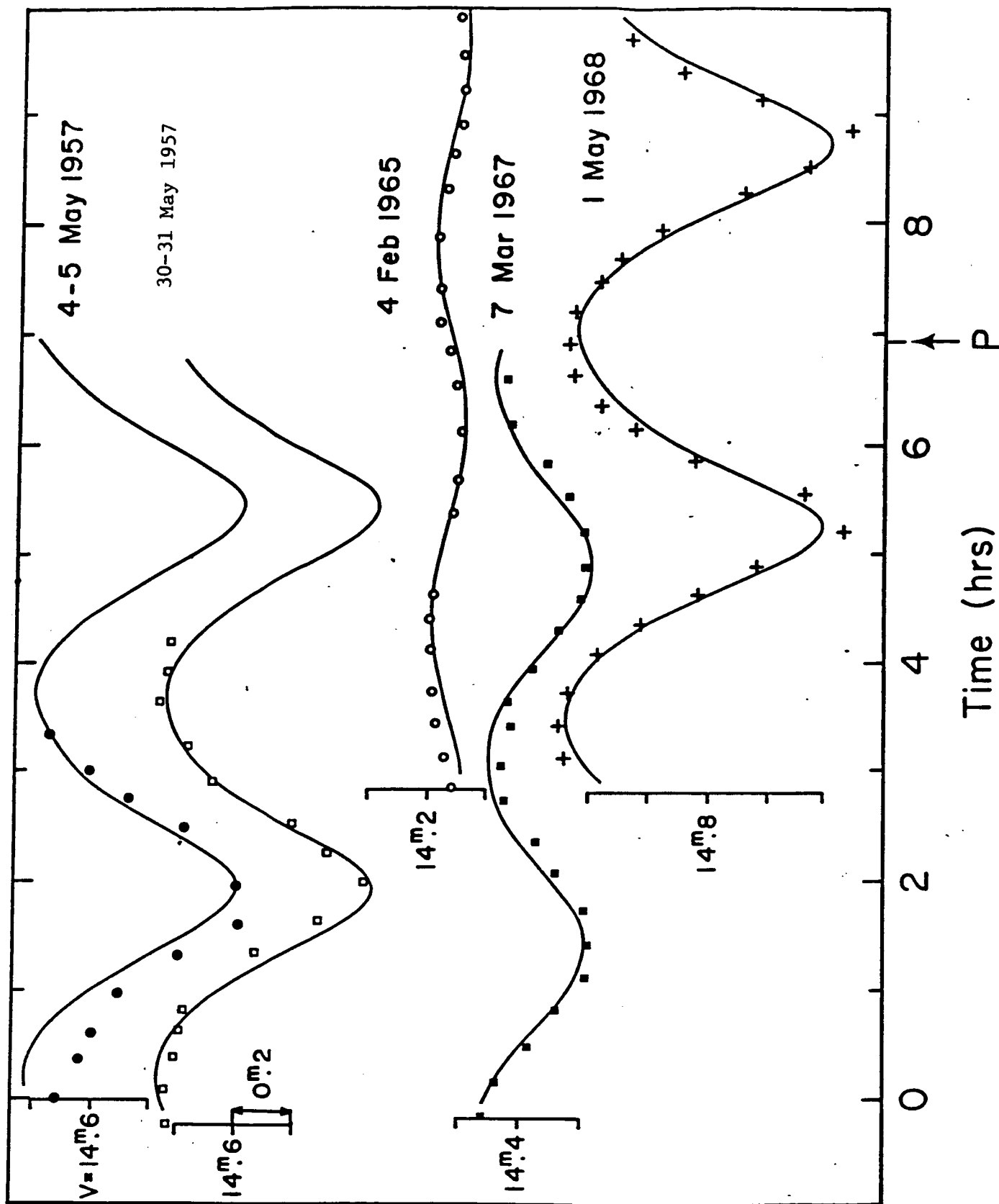
Figure 29

Observed lightcurves (points) and model for asteroid 624 Hektor. Both
the lightcurve amplitude and phase are properly fit with the model, as
described in the text.

Targets basically included those objects that were in need of astrometric observations for purposes of orbit improvement, such as newly discovered Earth-approaching asteroids, asteroids whose positions deviate significantly from ephemerides, etc. In 1986, astrometry was obtained on (659) Nestor, (3124) Kansas, (3548) 1973 SO, (3551) 1983 RD, (3554) 1986 EB, 1986 DA, and 1986 JK. All observations were published in the Minor Planet Circulars, and in the cases of 1973 SO, 1983 RD, and 1986 EB, they helped provide the definitive orbit solution that allowed them to be added to the catalog of numbered asteroids.

E. COMETS

E1. Photometry of Comet Halley

Tholen, N. Lark (Visiting Colleague), Hammel, and Piscitelli used the #1 0.61-m telescope nearly continuously from January to mid-June, except for the 7-week period around perihelion. An additional 43 nights of photometry were obtained, making a total of 65 nights of data on Halley collected between October 1985 and June 1986. In particular, nine consecutive nights of data were obtained from March 5 through 13, which covers the time of the five spacecraft encounters. These data were merged with similar data collected at Cerro Tololo by R. Millis and D. Schleicher (Lowell) to provide a better description of the activity of Halley during the spacecraft encounters. At that time, Halley was particularly active, showing changes in gas and dust production of more than a factor of 2 from night to night. Figure 30 shows the ultraviolet continuum magnitude (open circles) versus time during the spacecraft encounters along with ultraviolet minus blue color (filled circles). The color of the comet was obviously quite stable even though the dust production rate was varying by a tremendous amount. Reduction of the remainder of the extensive data set is an ongoing process.

E2. Monitoring of Comet Halley

Monitoring of Comet Halley continued throughout 1986. Observations were made in January, March, April, and June with the 2.2-m telescope, as well as with the 0.61-m telescope and the 0.3-m Schmidt camera throughout the early part of the year. Observations were made in support of the spacecraft encounters with P/Halley.

The 2.2-m telescope observations were made with the Galileo/IFA CCD at the Cassegrain focus. Images of the near-nuclear region were made through the International Halley Watch (IHW) standard filters as well as with special filters, which isolate emissions of the OH (0-0) and (1-1) bands (around 3100 Å), in an attempt to map the velocity field of the gas in the coma. Preliminary reductions of this data were reported at the October ESLAB symposium in Heidelberg. Final analysis of the OH data will be published before the end of this year.

A highlight of this effort is a continuous set of images in the IHW red continuum band taken throughout the spacecraft encounters with the comet in early March. Preliminary analyses of these images were uploaded to the IHW's computer for possible use in last-minute targeting of spacecraft to avoid dust jets. Further analysis will be useful in determining the state of the coma during the encounters and possibly in determination of the nuclear rotation rate. A list of all images submitted to the IHW near nucleus studies network for archiving is given in Tables IV and V.
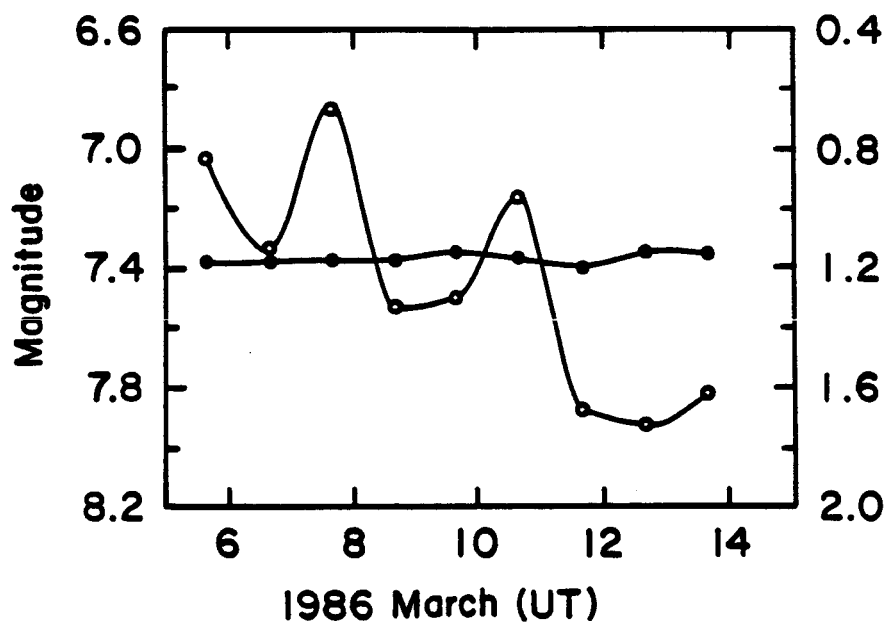
Figure 30

Table IV

Summary of CCD Images of Comet Halley, Mauna Kea Observatory, 1985-1986

Date (UT)	Time (UT)	Field (arcsec)	Filter[a]
22 Oct 85	09:23-10:07	69	open, IHW set
22 Oct	13:31-14:12	69	IHW set
23 Oct	10:17-12:03	69	open, IHW set
23 Oct	12:39-12:47	69	CN
24 Oct	11:15-12:39	69	IHW set
18 Nov	09:08-10:11	69	open, IHW set, red cont. mosaic
21 Nov	06:32-08:34	69	IHW set, H_2O^+ mosaic, H_2O^+ offset
21 Nov	11:13-11:58	69	H_2O^+, H_2O^+ mosaic, H_2O^+ offset
17 Dec	05:52-06:16	69	open, red cont. polarimetry
20 Dec	07:42-08:18	69	IHW set, open
04 Jan 86	06:03-06:25	69	IHW set, red cont. mosaic
05 Jan	04:50-06:27	69	IHW set, open, red cont. mosaic
06 Jan	04:57-06:10	69	IHW set, open, red cont. mosaic, red cont. offset, C_2 offset and mosaic
07 Jan	04:42-06:05	69	open, IHW set, red cont. mosaic and offset, C_2 mosaic & offset, H_2O mosaic
08 Jan	05:18-06:07	69	open, IHW set, red cont. mosaic, red cont. offset
04 Mar	15:29-15:35	135	red cont., red cont. mosaic
05 Mar	15:32-15:36	135	red cont., red cont. mosaic
06 Mar	15:13-15:41	345	IHW set, red cont. mosaic
07 Mar	15:26-15:34	135	red cont., red cont. mosaic, red cont. with 3° and 5° cont.
08 Mar	15:14-15:40	345	IHW set, red cont. mosaic, red cont. with 3° and 5° rotation
09 Mar	15:04-15:27	135	red cont., red cont. mosaic, red cont. with 5° and -5° rotation
10 Mar	15:20-15:24	360	red cont., red cont. with rotation
11 Mar	15:49-15:53	360	red cont., red cont. with rotation
13 Mar	15:58-15:59	210	red cont.
14 Mar	14:55-15:13	135	IHW set
18 Apr	09:26-09:29	135	red cont.
03 Jun	07:50-08:35	69	IHW set
04 Jun	07:07-08:09	69	IHW set

[a]IHW set" is the CN, C_3, CO^+, mid-continuum, C_2, red continuum, and H_2O^+ filters of the IAU/IHW comet filter set. Images taken through the OH0, OH1, and UV continuum filters are listed in Table V. "Mosaic" means a set of four images with the comet nucleus located in the four corners. The "offset" images are centered 30, 60, 90, or 120 arcsec from the comet.

Table V
Cometary OH Data

Object	Date (UT)	Time (UT)	Filter	Comments
G-Z	11 Sept	13:46-15:16	OHO,OH1,UVC	6 images
Halley	22 Oct	11:38-12:51	OHO,OH1,UVC	4 images
G-Z	22 Oct	14:37-15:25	OHO,OH1,UVC	3 images
Hartley-G	23 Oct	6:04-7:07	OHO,OH1,UVC	3 images
G-Z	23 Oct	13:31-15:08	OHO,OH1,UVC	3 good images
Hartley-G	24 Oct	5:33-7:10	OHO,OH1,UVC	4 images, cirrus
Halley	24 Oct	12:53-15:21	OHO,OH1,UVC	7 images
Thiele	18 Nov	6:09-8:07	OHO,OH1,UVC	3 good images
Halley	18 Nov	11:17-14:49	OHO,OH1,UVC	3 good images
Halley	21 Nov	8:55-10:08	OHO,OH1,UVC	3 images
Halley	19 Dec	7:37-8:18	OHO,OH1,UVC	4 images
Ciffreo	19 Dec	9:14-10:12	OHO,OH1,UVC	6 images
Halley	20 Dec	5:04-7:28	OHO,OH1,UVC	3 good images
Halley	4 Jan	4:39-5:56	OHO,OH1,UVC	3 good images
Halley	5 Jan	5:29-5:56	OHO,OH1,UVC	3 images
Halley	6 Jan	4:57-5:21	OHO,OH1,UVC	3 images
Halley	7 Jan	4:45-5:10	OHO,OH1,UVC	3 images
Halley	8 Jan	5:08-5:34	OHO,OH1,UVC	3 images
Halley	4 Mar	15:47-16:20	OHO,OH1	3 good images
Halley	5 Mar	15:38-16:10	OHO,OH1	3, bad focus
Halley	7 Mar	15:39-16:18	OHO,OH1	2 good images
Halley	9 Mar	15:31-16:03	OHO,OH1	2 good images
Halley	18 Apr	9:29-9:50	OHO,OH1,RC	--
Halley	3 June	6:40-7:34	OHO,OH1,RC	very weak

Note: Images were obtained through the IHW filters on most nights.
G-Z = Comet Giacobini-Zinner, Hartley-G = Comet Hartley-Good.

The 0.3-m Schmidt camera was used continuously during the dark phases of the Moon, to monitor the development of P/Halley's tail. The comet was observed on 31 nights during the first four months of the year, with a total of 72 plates being obtained. These were mostly blue-sensitive IIIa-J plates, which showed the gas tail, but several 3a-F plates were taken with a red filter to monitor the development of the dust tail. These have been loaned to the IHW large-scale studies network for archiving and analysis. A list of the plates submitted is given in Table VI. Figure 31 is a representative picture of Halley obtained with the Schmidt on 20 March 1986.

E3. Coordinated IR and Visible Mapping of Comets

Hammel, Cruikshank, and Storrs collaborated in 1985 and 1986 with C. Telesco (MSFC), H. Campins (PSI, Tucson), and others to produce simultaneous visible and infrared maps of comets P/Giacobini-Zinner and P/Halley. The IR mapping was done with a 20-element bolometric array; the Galileo/IFA CCD was used on the 2.2-m telescope to obtain the visible images.

From the simultaneous visible and IR images, albedo maps were calculated. The morphology was similar for both comets: a region of darker albedo was found in the anti-sunward direction, following the direction of the tail curvature. The albedo distribution is thought to be an effect of particle size distribution. Details are provided in the attached paper by Hammel et al. (1986).

E4. High-Dispersion Spectroscopy of Comet Halley

Buie and Cruikshank collaborated with T. C. Owen (Stony Brook) and B. Lutz (Lowell) to obtain high-dispersion spectra of the CN violet band using the coudé spectrograph (camera number 3) at the 2.2-m telescope. The CCD camera was used for this work, in January and April 1986.

Buie concentrated on the reductions of the spectra, and preliminary results were presented at the 20th ESLAB Symposium in Heidelberg. The spectra contain information about the $^{12}C^{14}N$ violet band system in Comet P/Halley. While the resolution of the data was not enough to resolve clearly any lines due to the less abundant $^{13}C^{14}N$ isotope, synthetic spectra computed by D. Schleicher (Lowell) enabled us to identify several $^{12}C^{14}N$ lines that have excess emission in the wings of the strong lines. We have interpreted this excess as evidence for the presence of the $^{13}C^{14}N$ isotope in measurable quantities. Work is continuing to determine an isotopic ratios from these data.

COMET HALLEY PLATE CATALOG

Table VI

PLATE #	DATE UT	START UT	EXP. TIME (min.)	EXP. MIDTIME	PLATE #	PLATE TYPE (baked)	FILTER	OBSERVER
1	23 OCT 1985	12:22:36	60	23.537 OCT 1985	1	IIIa-??	none	Buie
2	01 DEC 1985	06:02:26	25	01.260 DEC 1985	2	IIIa-??	none	Cruikshank
3	10 DEC 1985	06:20:00	30	10.274 DEC 1985	3	IIIa-??	none	Storrs
4	10 DEC 1985	07:28:30	30	10.322 DEC 1985	4	IIIa-??	none	"
5	10 DEC 1985	08:30:07	30	10.365 DEC 1985	5	IIIa-??	none	"
6	10 DEC 1985	09:26:12	20	10.400 DEC 1985	6	IIIa-??	none	"
7	11 DEC 1985	03:00:00	30	11.219 DEC 1985	7	IIIa-??	none	"
8	11 DEC 1985	04:20:00	30	11.274 DEC 1985	8	IIIa-??	none	"
9	11 DEC 1985	07:23:00	30	11.318 DEC 1985	9	IIIa-??	none	"
10	11 DEC 1985	08:28:05	30	11.363 DEC 1985	10	IIIa-??	none	"
11	02 JAN 1986	06:53:00	13.5	02.291 JAN 1986	11	IIIa-??	none	Cruikshank
12	03 JAN 1986	05:17:00	30	03.231 JAN 1986	12	IIIa-??	none	"
13	03 JAN 1986	06:06:30	30	03.265 JAN 1986	13	IIIa-??	none	"
14	04 JAN 1986	05:21:15	30	04.234 JAN 1986	14	IIIa-??	none	"
15	04 JAN 1986	04:58:00	15	04.212 JAN 1986	15	IIIa-??	none	"
16	04 JAN 1986	06:01:01	30	04.261 JAN 1986	16	IIIa-??	none	"
17	05 JAN 1986	05:24:45	30	05.236 JAN 1986	17	IIIa-??	none	"
18	05 JAN 1986	06:01:30	30	05.261 JAN 1986	18	IIIa-F	25 Wratten	"
19	06 JAN 1986	05:51:00	30	06.254 JAN 1986	19	IIIa-F	none	"
20	06 JAN 1986	04:55:00	45	06.220 JAN 1986	20	IIIa-??	none	Buie/Storrs
21	07 JAN 1986	09:14:45	30	07.229 JAN 1986	21	IIIa-??	none	"
22	08 JAN 1986	06:02:47	30	08.242 JAN 1986	22	IIIa-??	none	"
23	08 JAN 1986	05:16:32	30	08.230 JAN 1986	23	IIIa-F	28 Wratten	"
24	09 JAN 1986	05:12:00	30	09.227 JAN 1986	24	IIIa-??	none	"
25	09 JAN 1986	05:48:00	17	09.252 JAN 1986	25	IIIa-??	none	"
26	09 JAN 1986	06:26:00	40	09.275 JAN 1986	26	IIIa-??	none	"
27	10 JAN 1986	05:05:00	35.5	10.226 JAN 1986	27	IIIa-F	none	"
28	10 JAN 1986	05:53:00	30	10.258 JAN 1986	28	IIIa-??	none	Storrs
29	11 JAN 1986	05:34:00	30	11.242 JAN 1986	29	IIIa-??	none	"
30	11 JAN 1986	06:10:30	13.5	11.260 JAN 1986	30	IIIa-F	none	"
31	12 JAN 1986	04:10:00	07	12.260 JAN 1986	31	IIIa-??	none	"
32	12 JAN 1986	05:34:00	30	12.242 JAN 1986	32	IIIa-??	none	"
33	13 JAN 1986	07:10:30	30	13.307 JAN 1986	33	IIIa-??	none	"
34	13 JAN 1986	05:44:15	20	13.248 JAN 1986	34	IIIa-F	none	Buie
35	14 JAN 1986	05:13:00	27	14.228 JAN 1986	35	IIIa-??	none	"
36	16 JAN 1986	07:07:15	30	16.313 JAN 1986	36	IIIa-??	none	"
37	17 JAN 1986	05:18:00	25	17.230 JAN 1986	37	IIIa-F	none	Storrs
38	03 MAR 1986	15:19:00	20	03.645 MAR 1986	38	IIIa-F	28 Wratten	Buie
39	04 MAR 1986	15:36:00	08	04.652 MAR 1986	39	IIIa-F	28 Wratten	Cruikshank
40	05 MAR 1986	14:52:33	20	05.627 MAR 1986	40	IIIa-??	none	"
41	05 MAR 1986	15:19:20	10	05.642 MAR 1986	41	IIIa-??	none	Cruikshank/Buie
42	06 MAR 1986	15:11:23	20	06.640 MAR 1986	42	IIIa-F	28 Wratten	"
43	06 MAR 1986	14:46:38	20	06.623 MAR 1986	43	IIIa-F	28 Wratten	"
44	07 MAR 1986	15:14:38	20	07.642 MAR 1986	44	IIIa-F	none	"
45	07 MAR 1986	14:48:55	20	07.624 MAR 1986	45	IIIa-F	25 Wratten	Cruikshank
46	08 MAR 1986	15:07:15	21.75	08.638 MAR 1986	46	IIIa-??	none	"
47	08 MAR 1986	14:40:30	20	08.618 MAR 1986	47	IIIa-??	none	"
48	10 MAR 1986	14:43:00	20	10.620 MAR 1986	48	IIIa-F	none	Storrs
49	11 MAR 1986	15:56:30	30	11.675 MAR 1986	49	IIIa-??	none	"
50	12 MAR 1986	14:48:00	30	12.627 MAR 1986	50	IIIa-F	none	Cruikshank
51	13 MAR 1986	14:38:00	10	13.620 MAR 1986	51	IIIa-F	28 Wratten	"
52	16 MAR 1986	14:27:40	20	16.613 MAR 1986	52	IIIa-F	28 Wratten	"
53	16 MAR 1986	15:09:30	22	16.633 MAR 1986	53	IIIa-??	none	"
54	17 MAR 1986	14:55:49	30	17.633 MAR 1986	54	IIIa-??	none	"
55	17 MAR 1986	14:23:37	25	17.608 MAR 1986	55	IIIa-??	none	"
56	18 MAR 1986	15:03:50	25	18.636 MAR 1986	56	IIIa-??	none	Buie
57	19 MAR 1986	15:00:00	30	19.635 MAR 1986	57	IIIa-??	none	"
58	20 MAR 1986	14:46:00	30	20.626 MAR 1986	58	IIIa-F	28,25 Wratten	Storrs
59	24 MAR 1986	14:40:00	45	24.527 MAR 1986	59	IIIa-F	28 Wratten	"
60	24 MAR 1986	15:28:00	15	24.650 MAR 1986	60	IIIa-??	none	"
61	25 MAR 1986	14:35:00	?	? MAR 1986	61	IIIa-??	none	"
62	03 APR 1986	12:16:00	30	03.522 APR 1986	62	IIIa-F	25 Wratten	Buie
63	16 APR 1986	10:45:10	37	16.461 APR 1986	63	IIIa-F	25 Wratten	Storrs
64	17 APR 1986	08:18:00	60	17.367 APR 1986	64	IIIa-??	none	"
65	17 APR 1986	07:15:00	30	17.313 APR 1986	65	IIIa-??	none	Cruikshank
66	17 APR 1986	09:26:00	30	17.403 APR 1986	66	IIIa-??	none	"
67	17 APR 1986	10:37:00	30	17.453 APR 1986	67	IIIa-??	none	"
68	17 APR 1986	12:22:12	20	17.522 APR 1986	68	IIIa-??	none	"
69	18 APR 1986	10:11:00	30	18.435 APR 1986	69	IIIa-??	none	Buie
70	18 APR 1986	10:48:00	30	18.460 APR 1986	70	IIIa-??	none	"
71	18 APR 1986	11:24:20	18	18.486 APR 1986	71	IIIa-F	28 Wratten	Storrs
72	18 APR 1985	12:46:00	18	18.538 APR 1986	72	IIIa-??	none	"
73	18 APR 1986	08:18:00	30	18.356 APR 1986	73	IIIa-F	28 Wratten	"

E5. Other Comets

Tholen obtained five-color photometry of Comet Wilson on one night. The resulting colors were rather red, which now seems to be the norm as more and more color statistics are accumulated on comets. Photometry through the IHW filters was also obtained on one other night. It showed that Wilson had not yet developed very strong gaseous emission features.

F. LABORATORY STUDIES OF DARK ORGANIC MATERIALS

In the context of our continuing studies of solar system bodies of very low albedo, such as regions on planetary satellites, certain asteroids, and cometary nuclei, we have undertaken a series of laboratory spectroscopic observations of materials that may be present on some solar system bodies.

Cruikshank, with the help of Research Assistant K. Uchida, collected from various other investigators, a suite of stable organic compounds that were made under various conditions of relevance to planetary science. These substances, described below, were prepared to a uniform series of grain sizes by grinding and were then observed in diffuse reflectance with the spectrometers at the laboratories of R. N. Clark (USGS, Denver) and J. Salisbury (USGS, Reston). With Clark's spectrometer, the reflectance from 0.3 to 3.0 μm was measured, while Salisbury's instrument was used from 2.5 to 25 μm. Representative spectra in both wavelength regions are shown in Figures 32 and 33.

The materials assembled in this study include the following:

a. Kerogen, prepared from coal tar by dissolution of the soluble fraction. This material is that proposed by Veverka and Gradie as the possible coloring agent in the Trojan asteroids.

b. Lampblack

c. Insoluble organic extract from the Murchison CM carbonaceous chondrite, provided by L. Alaerts.

d. Bulk Murchison meteorite

e. Bulk Allende CV carbonaceous chondritic meteorite

d. Hydrogen cyanide polymers, prepared by C. Matthews

e. Stable residue from the proton irradiation of methane ice, prepared by G. Strazzulla

f. Tholins produced in the laboratory of B. Khare and C. Sagan from spark or UV irradiation of gaseous mixtures of relevance to planetary atmospheres.

We are preparing a publication that will include an atlas of all the spectra. These data constitute a useful resource for those scientists interested in the occurrence and distribution of organic matter in the solar system. We will continue our own comparative spectroscopic work in the search for the composition of the dark material that is found in so many bodies in the outer part of the solar system. This work takes on special relevance to comets in the context of the confirmation of the low albedo of Comet Halley by in situ spacecraft measurements and the discovery of organic emissions in the spectrum of the nuclear regions of the comet.

Kerogen: Residual insoluble material in coal tar after treatment
with toluene, hexane, and acetone. Particle size 90-125 um.
Prepared by Keven Uchida and Dale Cruikshank from recipe by
Jonathan Gradie.
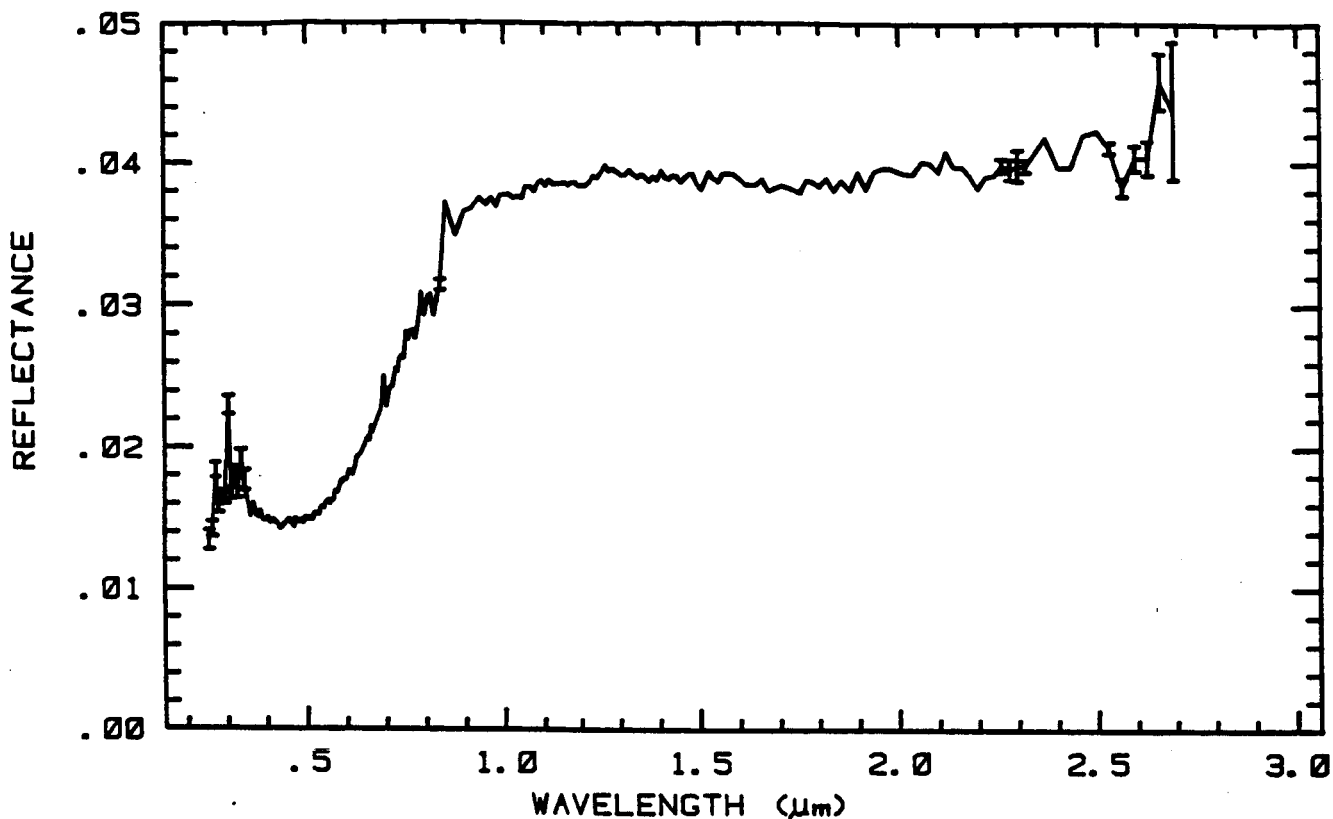
Kerogen .25-2.7um 8.5x ABS REF   opd8832   f 315   V200p813ECg

NICOLET DX V4.56   27 May 86 11:59:25
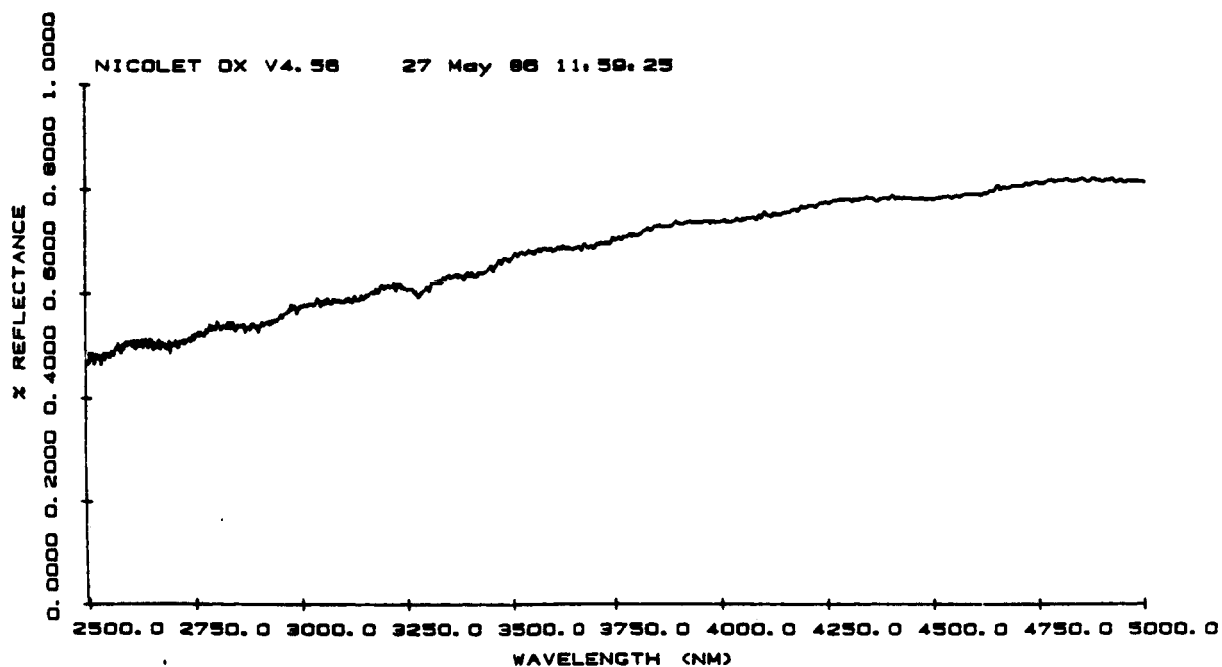
Figures 32 & 33. Reflectance spectra of a laboratory sample of kerogen taken in
two different wavelength regions in the laboratories of R. N. Clark and
J. W. Salisbury.

G. THEORETICAL AND ANALYTICAL STUDIES:
THERMAL INERTIAS AND THERMAL CONDUCTIVITIES OF PARTICULATE MEDIA

The remarkably high thermal inertia found for the bright regions of Io
led Sinton to ponder whether it was a consequence of a high thermal conductiv-
ity caused by the conduction of SO_2 gas within the interstices of the frost
particles. Considerable work had been done on the thermal conductivity of
particulate media, both laboratory and theoretical studies, prior to the
Apollo lunar landings, but relatively little recent work has been done. The
theoretical calculation of the thermal conductivity for such media is of
interest to chemical engineers for calculating the conduction in catalytic
beds and to the petroleum industry for locating oil bearing shales, as well as
being of interest to planetary scientists. Sinton has found that all such
papers in the literature are flawed by a misunderstanding of the thermal con-
ductivity of gases at low pressures. The transfer of heat between particles
by conduction by a gas at low pressures is a process that in first order does
not depend on the separation of the particles. This lack of dependence on
separation is also true for transfer by radiation. The previous treatments
are flawed in assuming that a thermal conductivity, which implies that conduc-
tion between particles is inversely dependent on their separation, can be
used. The theoretical treatments in the literature do not represent very well
the behavior of the thermal conductivity of particulates. To construct a cor-
rect theory, Sinton has focused attention on the conductance of heat between
individual particles. Conductance considers the amount of heat exchanged bet-
ween two particles at their actual separation. Processes that are considered
in this calculation are, besides radiation and gaseous conduction, conduction
by point contacts, conduction through the particles, and gaseous conduction
around (bypassing) the particles. After evaluating the heat conductance bet-
ween adjacent particles, it is then possible to derive the bulk thermal con-
ductivity of a particulate medium.

At least seven different sets of data giving the thermal conductivity of
particulates as a function of gas pressure ranging from high vacua to atmo-
spheric pressure are in the literature. These have been used to test the
theory. Model curves were fit to the data by a least-squares fitting proced-
ure with free parameters of particle size, porosity, contact conductance, and
a parameter from vacuum technology called the accommodation coefficient. The
accommodation coefficient is to gaseous conduction as emissivity is to radia-
tion. It expresses the fraction of heat that is actually transmitted from a
molecule to a surface upon impact.

The agreement that the model fitting gives between the known particle
size and that determined from the fitting for the size is impressive. The
porosities of most of the laboratory samples were not recorded. The results
from the models are given in Table VII. The fitted parameters, rows 7 to 10,

Table VII

Results from Fitting Model to Laboratory Data

Sample:	#1	#2	#3	#4	#5	#6	#7
Material	pumice	pumice	pumice	basalt	basalt	qtz. sand	qtz.sand
Size (μm)	0-44	44-104	104-149	44-104	44-104	74-104	590-840
Density	0.88	0.80	0.84	1.27	1.27	[1.55][a]	[0.95]
Porosity	--	--	--	[0.46]	[0.46]	0.59	0.36
Temp. (°K)	277	296	296	331	221	[293]	[293]
Reference[b]	1	1	1	1	1	2	2
α	0.36±0.06	0.54±0.04	0.44±0.01	0.43±0.03	0.39±0.08	0.32±0.08	0.16±0.01
d (μm)	10±1	57±5	180±23	94±21	83±9	136±8	652±4
e	0.87±0.07	1.00±0.07	0.61±0.09	0.25±0.07	0.27±0.06	0.37±0.02	0.64±0.04
Rc (Ks/cal)	169±21	54±5	65±5	18±4	20±3	2.2±0.1	0.36±0.03
Number	8	9	6	9	9	10	13
RMS (%)	12.5	11.1	4.0	10.5	18.3	5.9	9.6
size ratio	0.46	0.77	1.43	1.28	1.12	1.52	0.91

[a]Items in brackets are estimated.

[b]References: 1 = Wechsler et al. (1972); 2 = Woodside and Messmer (1961).

have the meanings: α = porosity, d = particle size, e = accommodation coef-
ficient, Rc = contact resistance (reciprocal of contact conductance). Number
is the number of data points for each sample and RMS characterizes the accu-
racy of the model fit to the data. What is particularly gratifying is the
last line, which expresses the ratio of the determined particle size to the
mean size of the sieve fraction from line 2 of the table. They are all close
to unity. The particle sizes range from 20 to 700 μm for the different
samples. Thus, it appears that the agreement is not fortuitous.

Figure 34 shows the agreement between the model calculations and the data
for the basalt samples, #4 and #5 in Table VII. Note that these two data sets
were for the same sample at two widely different temperatures. A separate
fitting was made combining all of the data on this sample and the determined
parameters were close to the means of those under #4 and #5 above. Figure 34
shows that the model is capable of fitting thermal conductivity data of
particulate media at a wide range of environmental pressures and temperatures.

There are a number of applications of this theory to the planets. An
immediate application is to the extensive set of thermal inertia measurements
made of Mars by the Viking orbiters. Briefly, it was found that there was a
bimodal distribution of thermal inertias (Palluconi and Kieffer, 1981, Icarus
45, 415-426). The maxima of both modes were dependent upon the altitude of
the surface above the zero reference level. If the particle sizes and other
parameters for either mode are not dependent upon the altitude, then the
observed thermal inertia should depend on the altitude as a consequence of the
variation of atmospheric pressure from site to site. From the model it is
found that at high pressures (1 mb to 1 bar) the thermal inertia should vary
with pressure as $(A + BP)^{1/2}$, where A and B are constants and P is the
pressure. The pressure in the Mars atmosphere was assumed to vary as
$\exp(-h/H)$ with the scale height H = 10 km. The gas was assumed to be CO_2.
The resulting fitting, Figure 35, is quite good. Note that the degree of
curvature in the model curve is dependent upon the assumed scale height.
In some calculations the scale height was left as a free parameter. The
obtained scale height was changed by only a few percent from that adopted
here. The constants A and B maybe related to the porosity and particle size.
For the high thermal inertia regions the derived particle sizes and porosities
are 80 μm and 15%. For the low thermal inertia regions they are 45 μm and
61%. Thus the primary difference between the high and low inertia regions is
the porosity. For these results, an accommodation coefficient of 1.0 has been
assumed. Changing this parameter changes only the derived particle size. The
contact conductance is unimportant at the high pressures experienced on Mars.

These results for the high thermal inertia regions do not agree with the
interpretation that is given in the literature (e.g., Palluconi and Kieffer),
where it is assumed that there is a variation of particle size with altitude.
If such a variation did exist, then the observed thermal inertia would vary
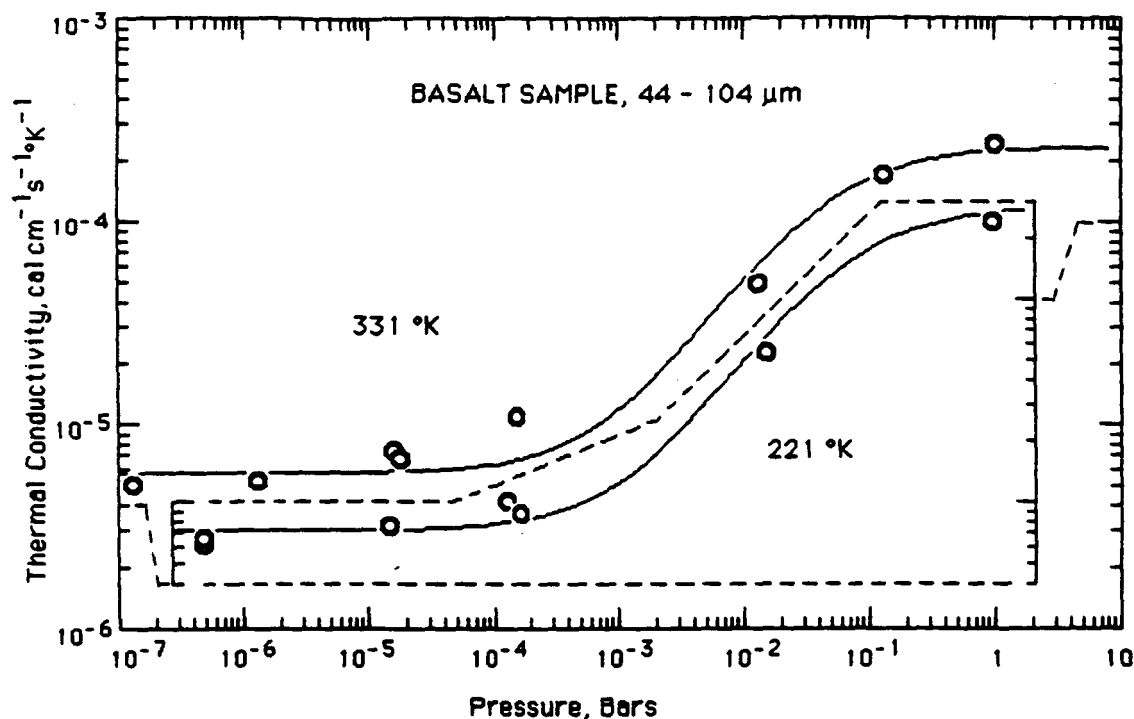
74

Figure 34. The laboratory data at two temperatures and a wide range of pressures are compared to the model calculations for the basalt sample having a size range of 44-104 μm. The model fitting yielded a size of 88 μm.
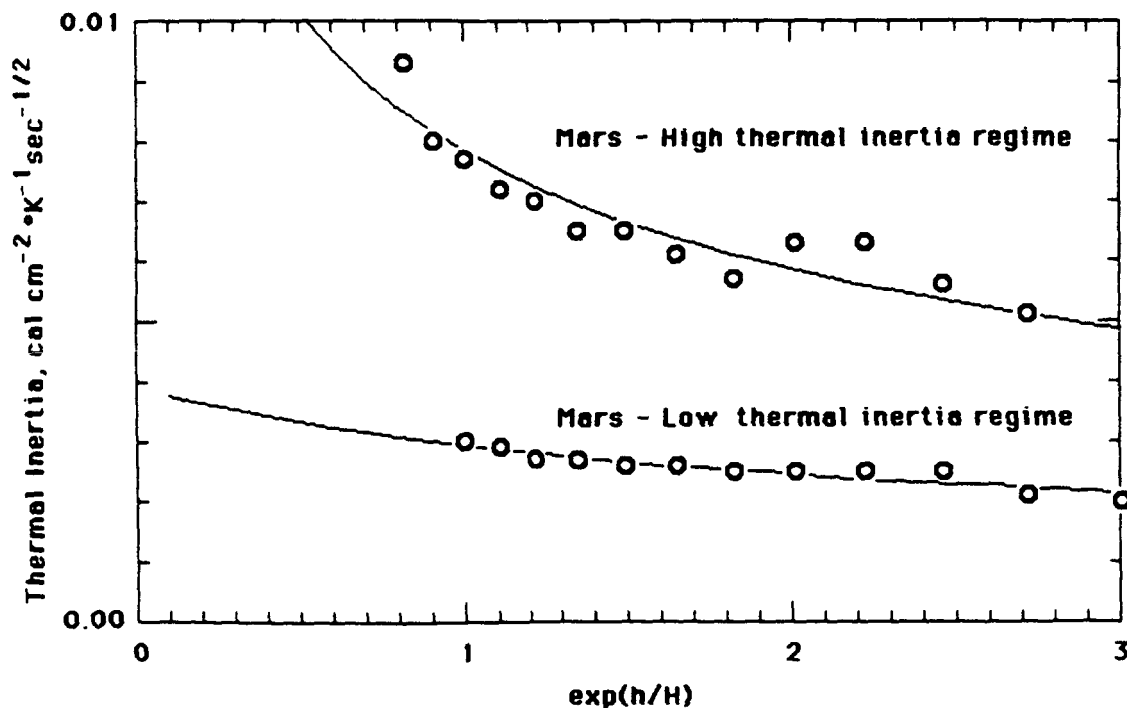
Figure 35. The Mars thermal inertia data from Palluconi and Kieffer (1981, Icarus 45, 514-426) are compared to models based on the new theory of thermal conduction in particulate media. For each of the two regimes, the particulate media are assumed to have the same size particles and porosity. The change in thermal inertia with altitude on Mars is produced by the change in atmospheric pressure, which is here assumed to vary exponentially with the generally assumed scale height of 10 km.

even more with altitude than the models with the known scale height are capable of fitting.

It is interesting, of course, to derive properties of the lunar regolith from its known thermal inertia and to compare these with the "ground truth" obtained from the Apollo missions. For particulates in a high vacuum only a combination of the fundamental parameters can be obtained. We have, arbitrarily, assumed that contact conduction is negligible in the lunar case. Then we are able to obtain the product of one minus the porosity raised to the 2/3 power and the particle size. The derived value for this is 52 μm. The value for lunar fines, using the volumetric median of the particle size, is 43 μm.

We can use this same modeling to derive this parameter for Mercury. The result is essentially the same as for the Moon. This is as expected because it is believed that the same process is responsible for producing the regolith in the two cases.

The thermal inertias have been determined for only two asteroids. The thermal inertia of Ceres has been only crudely obtained. It is, however, larger than that expected from the lunar result. The thermal inertia of Eros was obtained with better accuracy. It is considerably higher than expected from the lunar agreement. The high values may be interpreted as indicating a larger particle size than found on the much more massive Moon and Mercury. Evidently, the smaller particle sizes either are not produced in meteorite impacts on the asteroids or they are not retained by gravitational attraction.

Lastly, we get back to the question of the thermal inertia in the bright regions of Io. Sinton found that the higher thermal inertia cannot be explained by interstitial gas if the particle sizes are similar to those in the darker regions. One alternative is that the particle sizes are larger. If so, then the derived particle size is 4 mm. If this be the case, then the SO_2 frost would be like graupel. (Anybody for skiing Io?) Another alternative is that contact conductance is important or that the particles are needle shaped and contribute important conductance of heat through the long, skinny needles. Yet another possibility is that there is a "solid-state greenhouse effect" as has been investigated by R. H. Brown and D. L. Matson at JPL for high-albedo frosts. This would produce an apparent high thermal inertia in observations.

H. EXTRASOLAR PLANETARY MATERIAL:
THE SEARCH FOR DARK COMPANIONS OF K AND M GIANTS

The presence of dark companions around main-sequence and red giant stars can be inferred from the former's gravitational influence on the latter. By observing the radial velocity of the primary over an extended period of time, shifts in the radial velocity due to the companion can be detected. As an example, Jupiter causes a shift of 12 m/s in the Sun's radial velocity. Therefore the identification of Jupiter sized objects requires a precision in the radial velocity measurements of at least this much. We are aiming for a precision of <10 m/s.

K and M giant stars are excellent candidates in the search for low-mass (<0.05 solar masses) companions because their first overtone bands of CO in the 2.2-2.5 μm spectral region are relatively unblended and quite strong, therefore allowing high-precision measurements. The CO line frequencies can be determined very accurately in the laboratory. By placing N_2O cells in the beam we obtain the zero point calibration. Due to the brightness of our objects we can achieve high signal-to-noise ratios of about 200 in <4 hours of integration. With a spectral resolution of 2 km/s using the CO bands at 3900 to 4500 cm^{-1}, we achieve the desired radial velocity precision of <10 m/s. With this method, possible global oscillations and large-scale convective effects could also be identified.

Since 1978 Hall and collaborator K. H. Hinkle (KPNO) have been taking measurements on several K and M giants. Using the 4-m Mayall telescope on Kitt Peak with a rapid scanning Fourier Transform Spectrometer at the coudé focus they have obtained high quality infrared (1 to 5 μm) spectra of several giants as well as of Sirius and the Sun for comparison. Each measurement consists of a pair of scans: one forward and one backward. By taking the average and the difference between the two, an accurate subtraction of the noise is possible.

Recently Heyer retrieved the 1978-1986 data of 11 objects from KPNO for data analysis at IFA. The objects are β And, α Boo, αCet, γ Dra, β Gem, μ Gem, α Hya, α Tau, β UMi, Sirius, and the Sun.

Two necessary steps have to be undertaken to facilitate the analysis of this data. Since KPNO uses a different data format, the collected data needs to be reformatted and made readable by the devices available at IFA. Before attempting the actual analysis of the measurements, the radial velocities obtained have to be corrected to their heliocentric value. However, because of the high precision required, the common ephemeris correction is not sufficiently accurate.

Step one has been accomplished. Heyer is currently investigating the precision required of the heliocentric velocity correction. There are several programs available with varying degrees of accuracy. The final choice should

be sufficiently accurate but not overstrain our computer account. Concurrently, Hinkle and Heyer continue observations at KPNO on α Boo, β UMi, and the Sun.

Upon concluding the investigation concerning the heliocentric velocity correction, all accumulated data needs to be thus corrected and then analyzed for shifts in the stellar radial velocities. This will be done on the Institute's VAX 11/785 computer using some programs already available and some to be developed. At the same time further data will be collected at Kitt Peak, since long-term measurements are required to find possible shifts. Periods of 100 s to over 3 years could be expected.

III. OPERATION OF THE 2.2-M TELESCOPE

The University of Hawaii's 2.2-m telescope, which was dedicated in 1970, was the first major facility on Mauna Kea. This telescope and the scientific work accomplished with it have been largely responsible for the acceptance of Mauna Kea as the premier observing site in the northern hemisphere. Throughout the 1970s and the 1980s, observations with the 2.2-m telescope have made major contributions to planetary science, and this telescope remains the primary instrument for ground-based optical and synoptic studies of the solar system.

During the past several years, we have made substantial improvements to the operation of the telescope. Since these improvements are not generally known, and since a large fraction of our proposed budget will be used for the operation of the telescope, we will provide a short summary here.

A. Telescope Control System

The status of the telescope control system on August 1, 1984, was the following: The position encoders were the original telescope equipment and were no longer being manufactured. The control computer was an LSI 11/02 with single-density, single-sided floppy disks. The control program was virtually undocumented FORTH code. This system yielded pointing with an accuracy of 19 arcsec radius rms measured against approximately 150 stars all over the sky.

Our plan to modernize this aspect of the telescope operation consisted of three parts: (1) purchase new position encoders and design and fabricate the interface to the control computer, (2) install an LSI 11/23 computer with double-density, double-sided floppy disks, and (3) completely rewrite and document the control software, which would be based on that used at the IRTF.

The new encoders and the interfaces were working on the telescope by April 1985. This aspect of the modernization was funded by the State of Hawaii. The LSI 11/23 and its new disks, also funded by the State of Hawaii, were operating properly by early November 1985. The new software is now written, debugged, and partially documented. We expect to start using the new software during the spring of 1987. Based on the residuals to the flexure maps were have made, which are 1.8 arcsec radius rms, we expect to improve the telescope pointing by an order of magnitude. The salaries of the project scientist and part-time programmer for the software upgrade were funded by NASA.

Our plans for the future in this area are to finish the new software and to modify the control system to accept inputs from an autoguider.

B. Data Acquisition System

The data acquisition system consists of IR and CCD subsystems. On August 1, 1984, the IR subsystem contained and LSI 11/02 computer with single-sided,

single-density floppy disk drives, a 10 Mb hard disk, a CAMAC crate with devices, a 1600 bpi tape drive, and a 10-year-old lock-in amplifier. A version of the IRTF photometry program was implemented. The CCD subsystem was portable and contained an LSI 11/02 computer with 32 Kb of memory and single-sided, single-density floppy disk drives, a De Anza image-processing and display system, and a 1600 bpi tape drive. The two subsystems were completely independent, but both provided quick-look data reduction, e.g., IR magnitudes, flat fielding, and so forth.

Our plan to modernize this aspect of the telescope was to provide a resident CCD on-line data acquisition and control system of greatly increased capability, a VAX computer for off-line analysis, a much higher capacity hard disk, and the sharing of all available peripherals in the acquisition system by the two CPUs. At present, the CCD subsystem contains a 68010-based computer from Integrated Solutions, Inc., operating at 12 MHz with 3.25 Mb of memory. A 190 Mb hard disk, a dual-density, dual-sided floppy disk, and a 1600 bpi tape drive are shared between the two subsystems via an easily configurable patch panel. These upgrades were funded by the State of Hawaii with partial salary support from NASA. We have also purchased with State funds a new dual-input lock-in amplifier from Princeton Applied Research and have interfaced it with the IR system. We have brought up at the 2.2-m telescope a VAX 730 computer with 2 Mb memory, 450 Mb hard disk, and two 1600 bpi streamer tape drives. The same data analysis software that is used on our VAX in Honolulu is now running on the 2.2-m telescope's VAX, and we are in the process of implementing IRAF.

In the future we plan to have the VAX control the IR data acquisition using the program written for an identical machine at the IRTF. This scheme will save the 2.2-m telescope the cost of software development and improve maintainability. We also intend to connect the CCD data acquisition computer to the VAX via a high-speed link and acquire an image display for the VAX. Figure 36 shows our final desired configuration.

C. Operation from the Control Room

On August 1, 1984, the astronomer needed to be at the mirror cell in order to observe. Nearly every instrument was manually operated and nearly all guiding was done visually through an eyepiece. This situation was also dangerous in addition to being inefficient, since the mirror was 20 feet above the floor.

Our plan to modernize this aspect of the telescope operation was to provide remote operation of all instruments and to build a fully remote TV guider. Funds for the TV guider were provided by the NSF on December 15, 1984. We have purchased a new TV camera with a Gen II intensifier and have
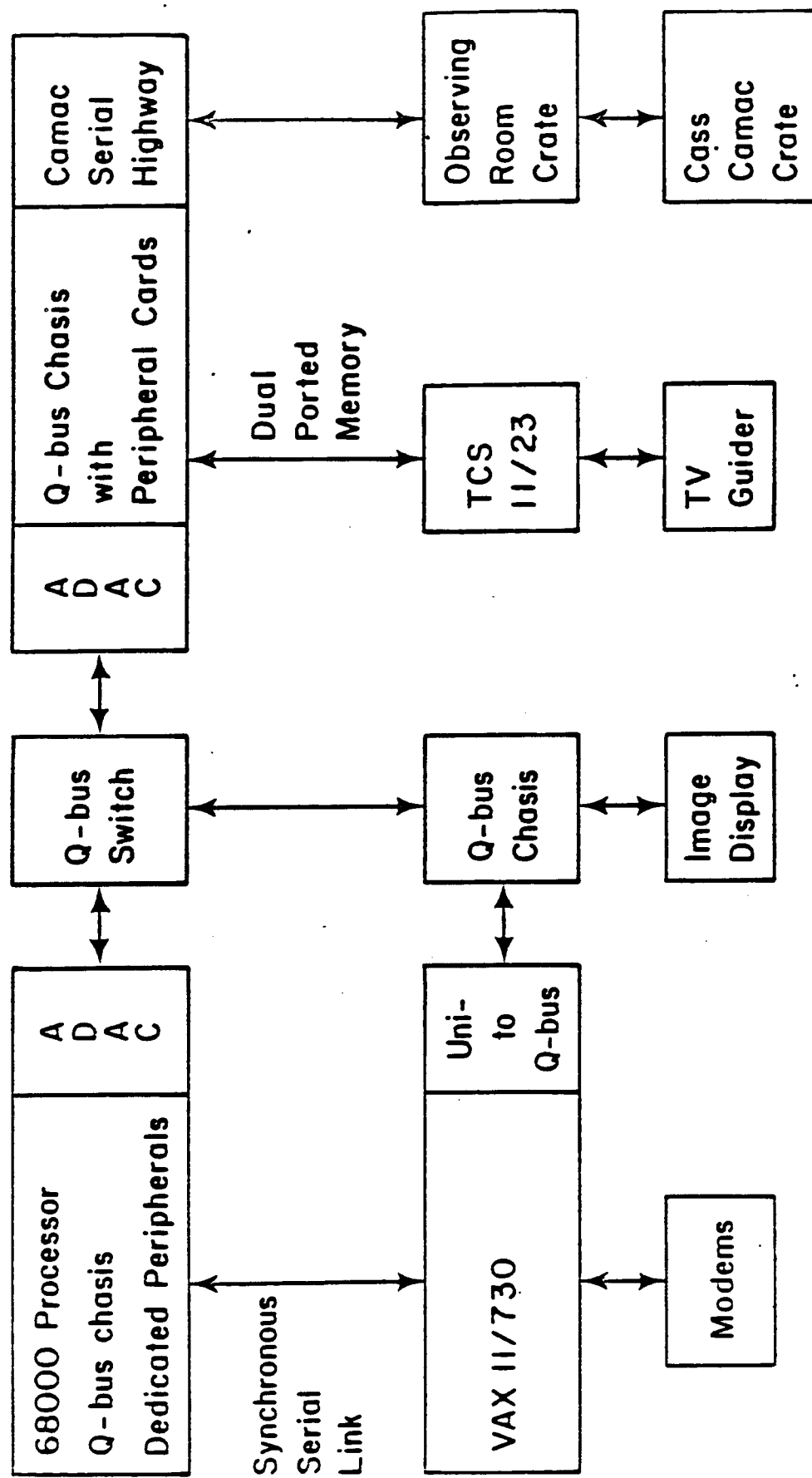
Fig. 36. Integrated computer systems for the 2.2-m telescope.

built the TV guider. We commissioned this new guider during August 1986. We have purchased a space TV camera using State of Hawaii funds. We have also provided for remote operation of nearly all our instruments: the CCD camera with motorized filter wheel, the Cassegrain Faint Object Spectrograph, and the IR CCD. All future instruments are planned to be remotely controlled as well.

D. Dome Seeing and High-Resolution Imaging

The seeing on Mauna Kea was known to be good, but this conclusion was based on subjective reports of the astronomers, not on systematic, objective measurements. We have conducted quantitative measurements for a period of 12 months (Aug. 1985-Aug. 1986) at the 2.2-m telescope using a seeing monitor permanently mounted on a folded Cassegrain focus. We find the median seeing at the 2.2-m telescope is 0.88 arcsec. We believe that the dome makes substantial contributions to this average because the seeing degrades with increasing temperature difference between a point near the primary mirror and the outside air. When this is <0, the median seeing is 0.78 arcsec.

Even prior to these results, however, we realized that the 2.2-m dome was degrading the seeing. We contracted with an architectural firm that had made similar studies for the CFHT and IRTF to recommend changes to our dome thermal environment with the associated cost. This study was funded by the State of Hawaii and was completed in June 1985. We then identified a source of funds to implement the suggested improvements and sent the the project out for bid last spring. Unfortunately, the bids were twice as expensive as estimated by the architect, so we were not able to proceed. The University has given this item a high priority on its FY 88 capital improvement budget that is now before the State Legislature.

To further modernize the facility, the Director and other scientists at the Institute for Astronomy have taken several new instrumentation initiatives. They are noted here briefly.

The Institute has been awarded four of the Texas Instrument CCD detector arrays that are from the same batch as those used in the Hubble Space Telescope; one has arrived so far. We are using it, chiefly on the 2.2-m telescope. To support this development further, we have pending with the NSF a major grant proposal on which Dr. Henry is the PI.

In addition to all of the above, we have received a high-sensitivity two-dimensional IR array detector that we have used for several runs on the 2.2-m telescope. This detector shows outstanding sensitivity, and we anticipate future heavy use.

A substantial fraction of the assigned time on the 2.2-m telescope has been given to planetary observations since the telescope was first put into operation. NASA, through the planetary program, has supported a concomitant fraction of the operating expense of the telescope and associated equipment.

Most of the NASA-supported time is used by IFA scientists, but a large fraction is used by the planetary scientists of the Planetary Geosciences Division of the Hawaii Institute of Geophysics. In addition, some solar system time is made available to outside users with programs of interest to NASA.

The statistics on planetary use of the 2.2-m telescope in 1986 are as follows:

First quarter   35%
Second quarter 46%
Third quarter   32%
Fourth quarter 14%

Total for 1986 32%

IV. PAPERS PUBLISHED OR SUBMITTED FOR PUBLICATION IN 1986

Binzel, R. P., A. L. Cochran, E. S. Barker, D. J. Tholen, A. Barucci, M. DiMartino, R. Greenberg, S. J. Weidenschilling, C. R. Chapman, and D. R. Davis (1987). Coordinated observations of asteroids 1219 Britta and 1972 Yi Xing. Icarus (submitted).

Buie, M. W., and U. Fink (1987). Methane Absorption Variations in the Spectrum of Pluto. Icarus (in press).

Cruikshank, D. P. (1986). Mauna Kea: A Guide to the Upper Slopes and Observatories. Institute for Astronomy, Honolulu.

Cruikshank, D. P. (1986). Dark matter in the Solar System. COSPAR (1986 volume, in press).

Cruikshank, D. P. (1986). Telescopic studies of the satellites of Saturn. In Solid Bodies of the Outer Solar System, ESA SP-242, pp. 51-59. (Proc. of a conference at Vulcano, Italy).

Cruikshank, D. P., and R. H. Brown (1986). Satellites of Uranus and Neptune, and the Pluto-Charon system. In Satellites (J. Burns and M. S. Matthews, Eds.), pp. 836-873. Univ. of Arizona Press, Tucson.

Cruikshank, D. P., R. H. Brown, A. T. Tokunaga, R. G. Smith, and J. R. Piscitelli (1986). Volatiles on Triton: The infrared spectral evidence, 2.0-2.5 micrometers. Icarus (submitted)

Goguen, J., H. B. Hammel, and R. H. Brown (1986). V Photometry of Titania, Oberon, and Triton. Icarus (submitted).

Hammel, H. B., and M. W. Buie (1987). An atmospheric rotation period of Neptune determined from methane-band imaging. Icarus (in press).

Hammel, H. B., C. M. Telesco, H. Campins, R. M. Decher, A. D. Storrs, and D. P. Cruikshank (1986). Albedo maps of comets P/Giacobini-Zinner and P/Halley. 20th ESLAB Symposium on the Exploration of Halley's Comet, ESA SP-250, Vol. I, pp. 73-77.

Hammel, H. B., C. M. Telesco, H. Campins, R. M. Decher, A. D. Storrs, and D. P. Cruikshank (1987). Albedo maps of comets P/Halley and P/Giacobini-Zinner. Astronomy and Astrophysics (in press).

Hanel, R., and others, including D. Cruikshank. (1986). Infrared observations of the Uranian System (Voyager 2 IRIS Team report). Science 233, 70-74.

Harris, A. W., J. W. Young, J. Goguen, H. Hammel, G. Hahn, E. F. Tedesco, and D. J. Tholen (1987). Photoelectric lightcurves of the asteroid 1862 Apollo. Icarus (submitted).

Hartmann, W. K., D. J. Tholen, and D. P. Cruikshank (1987). The relationship of active comets, "extinct" comets, and dark asteroids. Icarus 69, 33-50.

Piscitelli, J. R., D. P. Cruikshank, and J. F. Bell. (1986). Laboratory studies of irradiated nitrogen-methane mixtures: Application to Triton. Icarus (submitted).

Piscitelli, J. R., D. J. Tholen, N. Lark, and H. B. Hammel (1986). Photoelectric photometry of comet P/Halley from Mauna Kea Observatory. 20th ESLAB Symposium on the Exploration of Halley's Comet, ESLAB SP-250, Vol. III, pp. 499-502.

Schleicher, D. G., R. L. Millis, D. Tholen, N. Lark, P. V. Birch, R. Martin, and M. F. A'Hearn (1986). The variability of Halley's comet during the Vega, Planet-A, and Giotto encounters. 20th ESLAB Symposium on the Exploration of Halley's Comet, ESA-SP 250, Vol. I, pp. 565-567.

Sinton, W. M. (1986). Through the infrared with logbook and lantern slides. Pub. Astron. Soc. Pacific 98, 246-251.

Telesco, C. M., R. Decher, C. Baugher, H. Campins, D. Mozurkewich, H. A. Thronson, D. P. Cruikshank, H. B. Hammel, S. Larson, and Z. Sekanina (1986). Thermal-infrared and visual imaging of comet Giacobini-Zinner. Astrophys. J. 310, L61-L65.

Tholen, D. J., M. W. Buie, and C. E. Swift (1987). Circumstances for Pluto-Charon mutual events in 1987. Astron. J. 93, 244-247.

Tholen, D. J., D. P. Cruikshank, W. K. Hartmann, N. Lark, H. B. Hammel, and J. R. Piscitelli (1986). A comparison of the continuum colors of P/Halley, other comets, and asteroids. 20th ESLAB Symposium on the Exploration of Halley's Comet, ESA SP-250, Vol. III, pp. 503-507.

Veeder, G. J., M. Hanner, and D. J. Tholen (1987). The nucleus of comet P/Arend-Rigaux. Astron. J. (in press).

ATTACHMENT

ALBEDO MAPS OF COMETS P/GIACOBINI-ZINNER AND P/HALLEY

H.B. Hammel A.D. Storrs
   D.P. Cruikshank

C.M. Telesco R.M. Decher

H. Campins

Institute for Astronomy
University of Hawaii
Honolulu, Hawaii USA

NASA Marshall Space
 Flight Center
Huntsville, Alabama USA

Planetary Science
 Institute
Tucson, Arizona USA

ABSTRACT

Near-simultaneous infrared and visual maps of
P/Giacobini- Zinner (P/G-Z) and P/Halley are com-
bined to create maps of the spatial variation of
geometric albedo. P/G-Z shows a minimum in albedo
near 0.07 with an increase of a factor of 2 over
about 30 arcsec. The lowest albedos are offset
from the nucleus in the anti-sunward direction,
coincident with a dust tail observed in the IR.
The P/Halley albedos are higher than those found
for P/G-Z and range from 0.2-0.4, but the trend of
darker albedo in the anti-sunward direction (along
the tail) is the same. We attribute the albedo
distribution to large, dark, fluffy grains con-
fined to the orbital plane close to the nucleus.
The high albedo values in P/Halley may be due to
enhanced flux in the visual image because of the
comet's very small phase angle.

Keywords: Halley, Giacobini-Zinner, Mapping,
Albedo distribution, Dust

1. INTRODUCTION

In this paper we present visual and infrared map-
ping of comets P/Giacobini-Zinner and P/Halley.
The visual maps trace the distribution of light
reflected by dust, while the IR maps trace the
dust's thermal emission. By combining the two
data sets, we construct maps of the spatial dis-
tribution of albedo in the near-nuclear regions of
these comets. From this information and the infor-
mation in the individual maps, we hope to build a
consistent picture that explains both the albedo
distribution in each comet and the difference in
albedo between the comets. The observations and
data reduction of P/Giacobini-Zinner are presented
first, followed by a discussion of P/Halley. The
final section summarizes the results.

2. P/GIACOBINI-ZINNER

2.1 Observations

Near-simultaneous observations of P/Giacobini-
Zinner were made from two sites on 4 August 1985.
Additional details about the observations can be
found in Ref. 1.

2.1.1 Visual observations. The visual data con-

sist of a single CCD image taken with the
University of Hawaii 2.24-meter telescope (Mauna
Kea Observatory). The 5-minute exposure was taken
through an imaging quality filter obtained from
the International Halley Watch (IHW). The filter
samples the red continuum at 6840 Å. The image
scale of the 500x500 array was 0.138 arcsec/pixel,
giving a field of 69x69 arcsec centered on the
comet. The start time of the exposure was 12:06 UT.

2.1.2 IR observations. The 10.8-μm map was made
at the 2.3-meter telescope at Wyoming Infrared
Observatory with a 20-pixel two-dimensional bolom-
eter array. The full array covered 42x33 arcsec;
overlapping fields were combined to produce a
mosaic map with dimensions of approximately 80x160
arcsec. The IR map was obtained over a period of
5 hours centered on 10:00 UT. A contour map of
the data is presented in Figure 1.

2.1.3 Geometry. On 4 August 1985, the geocentric
distance of P/Giacobini-Zinner was 0.59 AU and its
heliocentric distance was 1.12 AU. The comet was
at a moderate phase angle (64°) at the time of
these observations, giving a favorable view of the
tail structure. This was particularly evident in
the IR thermal map, where there appears to be a
large-grain tail superposed on the underlying coma
and broader small-grain tail (Ref 1.). Because
the IR observations bracket the visual obser-
vation, time variability of the comet should not
be a problem.

2.2 Data Reduction

2.2.1 Calibration. The visual data were cali-
brated using measurements of Landolt star 144-755
in conjunction with the IHW flux calibration for
primary solar analogs. The star ↓ Cep was used as
a primary flux standard for the IR data. Details
of the calibration for both data sets can be found
in Ref. 1. Following absolute calibration of both
data sets, the visual data were rescaled and
binned to match both the beam size (7.5 arcsec
square) and sample spacing (8.5 arcsec center-to-
center) of the IR map. Care was taken to ensure
that the maps were properly aligned.

2.2.2 Albedo calculation. The average albedo was
calculated by using the simplifying assumption
(Refs. 2, 3) that the ratio of the total fluxes in
the scattered solar and thermal emission energy
distributions equals the ratio of the maximum

values of λF_λ for each distribution. The ratio of λF_λ(visible)/λF_λ(infrared) is defined to be S. The albedo, g, is then equal to S/(S + 1). For the dust temperatures inferred from the IR map for Giacobini-Zinner (Ref 1.), the peak thermal flux occurred near 10.8 µm. We correct for the fact that the peak visual flux does not occur at 6840 Å by multiplying our visual data by a factor of 1.35. Albedos of other comets calculated with this method typically have values between 0.1 and 0.3 (Ref. 3).

2.3 Albedo map

2.3.1 Albedo values and distribution.
The albedo map for P/Giacobini-Zinner is shown in Figure 2. The map was limited spatially by the size of the single CCD frame centered on the nucleus. The blanked-out region was contaminated by a field star. The albedos are low, ranging from 0.07 to 0.15. The lowest values are found offset slightly from the nucleus in the anti-sunward direction, i.e., along the tail. The values of g increase radially from the nucleus, except possibly in the direction of the tail, where the albedos are still slightly lower.

2.3.2 Possible sources of error.
A possible source of error in determination of the albedo map is misalignment of the two data sets used to calculate the final map. To estimate the magnitude and morphology of such an error, tests cases were run with the visual image deliberately offset from the IR map. The intensity distributions of both the visual and IR maps are strongly peaked; even a very small error in alignment (less than 3 arcsec) manifested itself as an obvious distortion of albedo contours. Misalignment of the data sets cannot cause the observed albedo distribution.

Another possible source of error is poor calibration of the visual image. There was thin cirrus several hours before the P/Giacobini-Zinner observations were made. Simulated variation of the standard star flux by ±20% (an overestimate) of the observed value had no effect at all on the spatial distribution of albedo. The albedo values change by only ±0.01. Therefore, even a conservative estimate of the calibration error leads to material that is dark.

2.4 Interpretation

The IR map indicates a tail composed of large (>100 µm) grains (Ref. 1). The region of lowest albedo corresponds spatially with this large-grain tail (see Figures 1, 2). Because multiple internal scattering may cause large grains to appear dark, we infer we were observing a low albedo area caused by the presence of large dark grains. This is implied by both the low albedo (multiple scattering in large fluffy grains) and the location of low albedo relative to the nucleus and the large-grain tail. Large grains are expected be closer to the nucleus because of slower ejection velocities.

3. P/HALLEY

3.1 Observations

Observations of P/Halley were made on 18 November 1985. Additional details of the observations are discussed in Ref. 4.

3.1.1 Visual observations.
Five CCD images were obtained with the same filter, camera, and telescope described in Section 2.1.1. Two-by-two binning of the data was done at the telescope, yielding an image scale of 0.276 arcsec/pixel. The field of each individual image is 69x69 arcsec. Four images were taken with the nucleus of P/Halley shifted into each of the four corners. The nucleus was centered in the fifth image. The position of the nucleus was determined to within a fraction of a pixel for each image. The images were then shifted appropriately and added to form a single composite image centered on the nucleus with a field of 125x125 arcsec. The nuclear region of the composite was carefully compared with the single direct CCD image to verify that no spurious structure was created during the mosaic processing. All five 2.5-minute exposures were taken between 9:50 and 10:14 UT.

3.1.2 IR observations.
The thermal IR map of P/Halley was made at the NASA Infrared Telescope Facility at Mauna Kea Observatory using the same bolometric array described in Section 2.1.2. The pixel size was 4.3x4.3 arcsec, with the separation between pixels equal to 4.5 arcsec. The field covered is about 80x100 arcsec. The map was created by combining overlapping fields obtained over a period of 6.7 hours centered on 11:00 UT. Figure 3 shows a contour map of the IR data.

3.1.3 Geometry.
The geocentric distance of P/Halley was 0.7 AU on this date; the heliocentric distance was 1.7 AU. At the time of these observations, the comet was near opposition: the phase angle was 2° and changed by only about half a degree over the course of the observations. This means any significant dust tail should be along the line of sight. Nevertheless, the IR map shows the dust tail curves toward the southeast; the visual map is also asymmetric, with the lowest brightness levels extended toward the southeastern corner. The IR and visual observations were not simultaneous--the visual images were obtained 4 hours before the last sections of the IR map. Although the phase angle was nearly constant over this period, the position angle of the tail was changing rapidly, causing rotation of the tail by 11° between two data sets.

3.2 Data reduction

The data reduction process is the same as described in Section 2.2 for Giacobini-Zinner.

3.3 Albedo map

3.3.1 Albedo values and distribution.
The P/Halley albedo map is shown in Figure 4. The albedos are systematically higher than those in the P/Giacobini-Zinner map. In fact, the values are high in general, ranging from 0.25 to 0.45. While there is less contrast (i.e., variation) in albedos in the P/Halley albedo map, the spatial distribution of albedo is similar to that of P/Giacobini-Zinner: the region of lowest albedo seems to be in the direction of the tail--the anti-sunward direction. The albedo increases radially from the nucleus, except along the tail, where the albedos are depressed.

3.3.2 Possible sources of error.
Misalignment of the P/Halley maps is unlikely for the same reason discussed above for P/Giacobini-Zinner: both maps show a very strong central condensation. Thus the
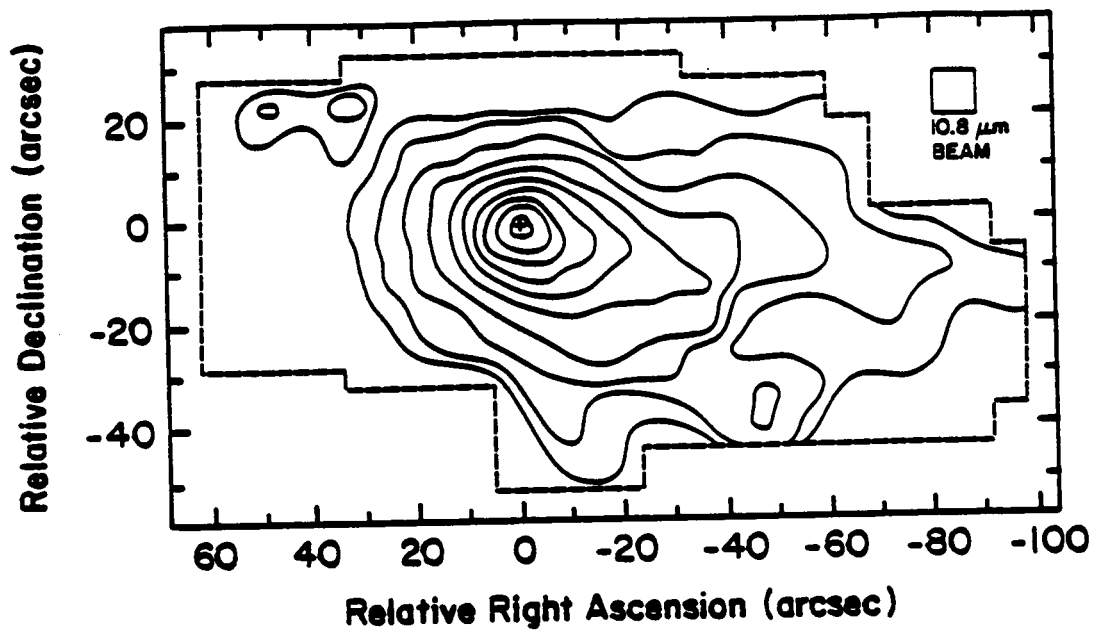
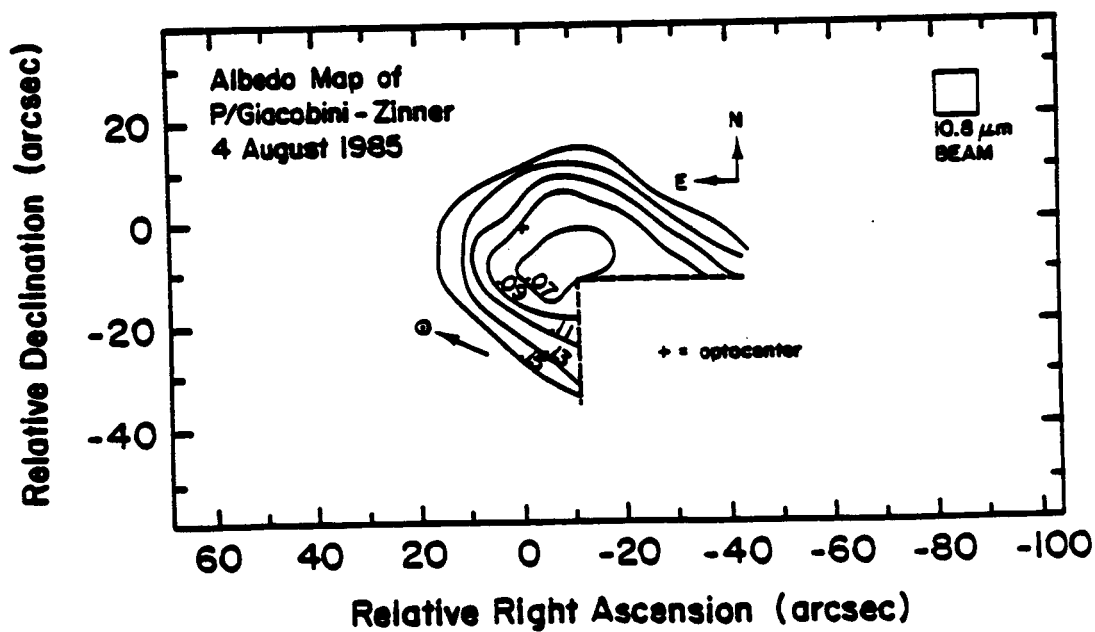Figure 1. Map of P/Giacobini-Zinner at 10.8 μm

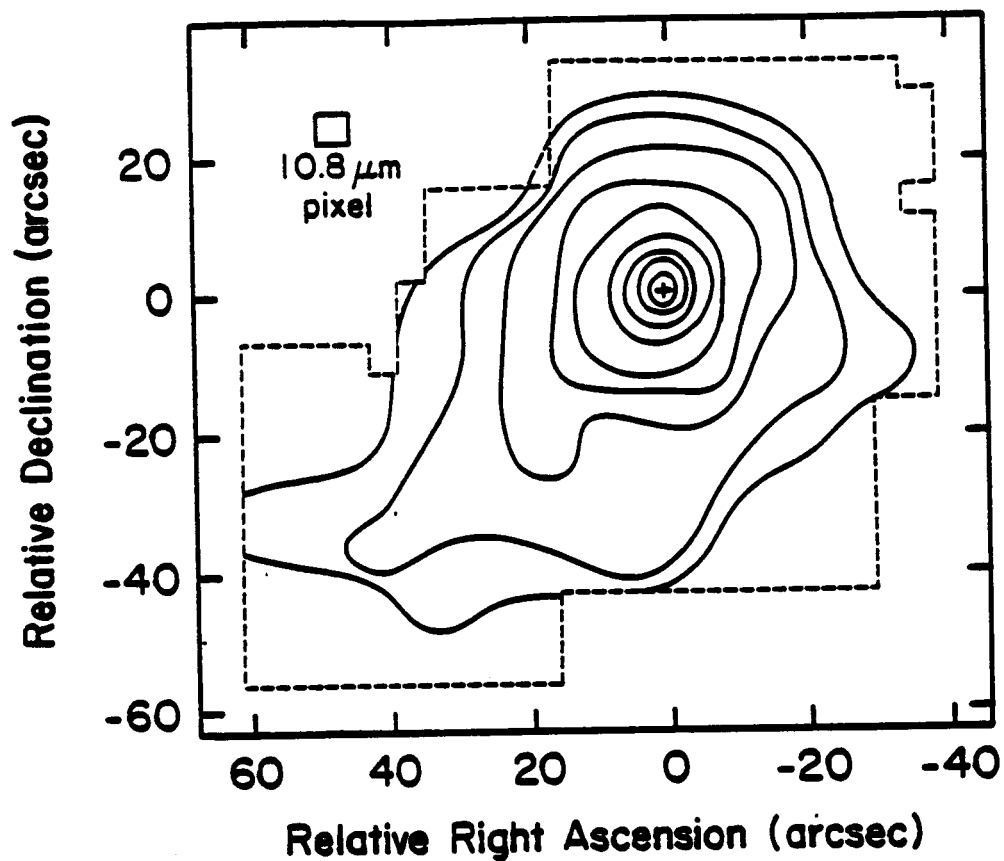Figure 2. Albedo Map of P/Giacobini-Zinner

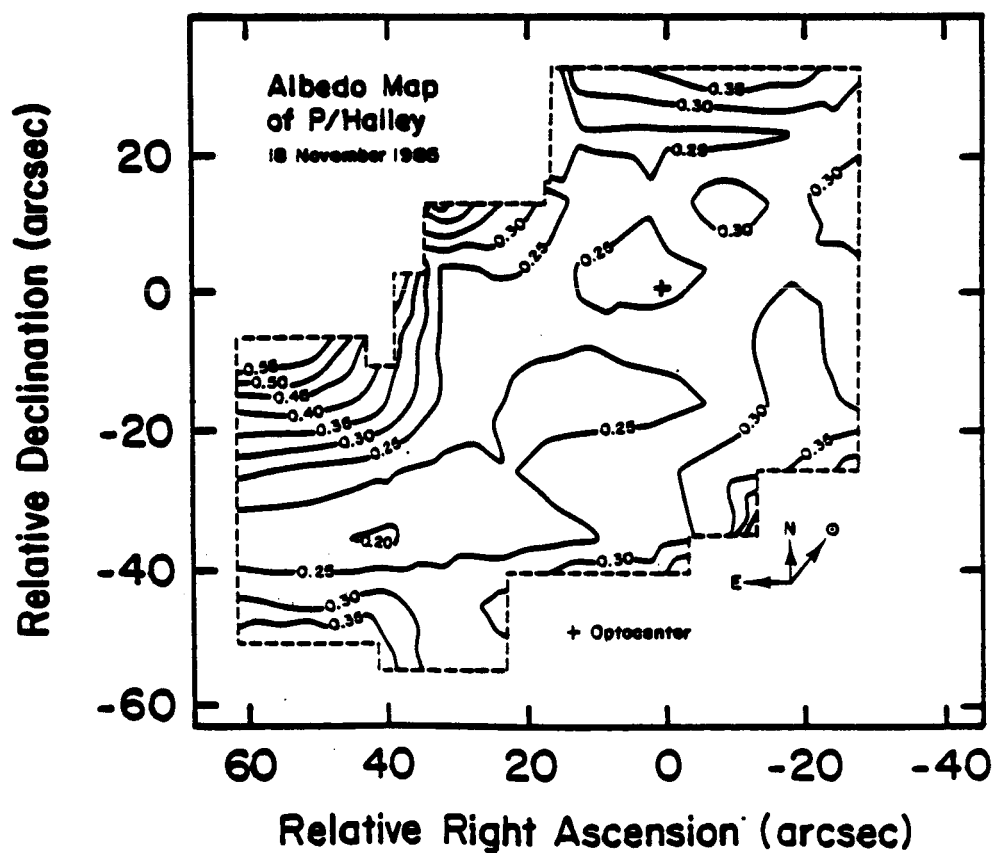Figure 3. Map of P/Halley at 10.8 μm

Figure 4. Albedo Map of P/Halley

albedo map is very sensitive to the alignment; small errors make large distortions.

The sky was clear and photometric during the observations. There should be no problem with the standard star calibration.

As discussed above, the position angle of the Halley's tail changed by 11° between the observation times of the visual and IR maps. However, the visual contours are very smooth over this range of angle, implying little or no change in the albedo map if the image were rotated.

3.4 Interpretation

The overall higher albedos in P/Halley are probably due to increased brightness in the visual map. Enhanced brightness at continuum wavelengths near opposition has been seen in other comets (e.g., see Refs. 5, 6). This has been interpreted as enhanced backscattering by dust, and it may produce a brightness increase as large as a factor of 3 at near opposition phase angles (Ref. 5). If P/Halley is a normal comet, we would expect a backscattering peak at the phase angle observed here. The albedo values in the Halley map would be comparable with typical cometary values if reduced by a factor of 2-3.

The difference in contrast between the P/Halley and P/Giacobini-Zinner maps may indicate a smaller concentration of large grains, which presumably cause the deep depression in the P/G-Z data. IR observations of Halley at moderate phase angle (60°-62°) made in March 1986 show a dearth of large particles relative to Giacobini-Zinner (Ref. 7). The March Halley observations and the IR observations of P/G-Z reported here were made when the comets were at nearly identical heliocentric and geocentric distance. Thus, there is a consistent picture of grain-size distribution and albedo.

4. SUMMARY

We have presented maps of the albedo distribution of comets P/Giacobini-Zinner and P/Halley. The maps are derived from near-simultaneous visual and infrared mapping of the comets. Both comets show a similar distribution in albedo, with the albedo increasing radially from the nucleus except along the anti-sunward direction, where the albedos

remain lower. The contrast in albedo is much more pronounced in the P/Giacobini-Zinner map. We interpret the albedo distribution as being produced by large grains concentrated near the nucleus. The smaller contrast in the P/Halley map is consistent with IR observations which show a dearth of large grains in P/Halley relative to P/Giacobini-Zinner.

The high albedos in P/Halley are probably a result of increased brightness in the visual data. The near-opposition geometry may produce enhanced backscattering from the dust in the coma. Such backscattering peaks have been observed at low phase angle in other comets, typically causing an increase of a factor of 2-3 over the continuum values at moderate phase angles.

6. REFERENCES

1. Telesco, C.M. et al. 1986, Thermal infrared and visual imaging of Comet Giacobini-Zinner, Ap. J. (Letters), in press.

2. O'Dell, C.R. 1971, Nature of particulate matter in comets as determined from infrared observations, Ap. J. 166, 675-681.

3. Ney, E.P. 1982, Optical and infrared observations of bright comets in the range 0.5 mm to 20 mm, in Comets, ed. L.L. Wilkening, Tucson, University of Arizona Press, 323-340.

4. Telesco, C.M. et al. 1986, in preparation.

5. A'Hearn, M.F. et al. 1984, Comet Bowell 1980b, Astron. J. 89, 579-591.

6. Millis, R.L. et al. 1982, Narrowband photometry of Comet P/Stephan-Oterma and the backscattering properties of cometary grains, Astron. J. 87, 1310-1317.

7. Campins, H. et al. 1986, Thermal IR imaging of Comet Halley, these proceedings.

5